

Alma Mater Studiorum - Università di Bologna

DOTTORATO DI RICERCA IN
MONITORAGGIO E GESTIONE DELLE STRUTTURE E
DELL'AMBIENTE - SEHM2

Ciclo 33

Settore Concorsuale: 08/B2 - SCIENZA DELLE COSTRUZIONI

Settore Scientifico Disciplinare: ICAR/08 - SCIENZA DELLE COSTRUZIONI

RESONANT METAMATERIALS FOR THE CONTROL OF RAYLEIGH WAVES

Presentata da: Farhad Zeighami

Coordinatore Dottorato

Alessandro Marzani

Supervisore

Alessandro Marzani

Co-supervisore

Antonio Palermo

Esame finale anno 2021

To my family and my wife.

ACKNOWLEDGMENTS

I would like to express my most sincere gratitude and appreciation to my respective advisor Prof. Alessandro Marzani for the continuous guidance throughout my Ph.D. journey, for his patience, motivation, and insightful discussions. He has been always super supportive and very kind to me and has given me so much freedom to pursue different research directions.

Besides my advisor, I would like to extend my deep appreciation to my co-advisor Prof. Antonio Palermo who supported me in every step of the way. He has been always available to listen to my ideas and share his immense knowledge. Antonio, I really enjoyed our collaboration, and I am grateful for sharing your office with me and giving me the opportunity to have regular daily discussions.

Special appreciations go to Prof. Wieslaw Ostachowicz and Prof. Pawel Kudela from the Institute of Fluid-Flow Machinery - Polish Academy of Sciences who welcomed me warmly during my six-month mobility period in Gdańsk.

My thanks also go out to Prof. Dimitris Pitilakis and his research group from the Aristotle University of Thessaloniki for their collaboration on the field testing of the resonant wave barrier. I also thank researchers Dr. Nicola Testoni and Ing. Denis Bogomolov who supported me with the experimental testing of the metamaterial plate. I would like to thank Ing. Francesco Vai from the Laboratory of Mechanics for the fabrication of the metamaterial plate.

I thank all my research colleagues: Xingbo, Zinon, and Milad. I appreciate our challenging discussions during our group meetings. I would like to also thank the advisory board of the SEHM2 Ph.D. programme and my colleagues in the XXXIII cycle. We had interesting meetings and I enjoyed exchanging ideas with you. I convey my gratitude to the head of the laboratory of computational mechanics - LAMC, Prof. Stefano de Miranda, and all my coworkers there: Luca, Antonio, Giulia, Mao, Weilin, and Jin Xing. Thanks for your supports.

In addition, I would like to thank the reviewers of this thesis, Prof. Zhibao Cheng from Beijing Jiaotong University, and Prof. Ioannis A Antoniadis from the National University of Athens.

Finally, I would like to express my deepest gratitude to my father Ali, my mother Akram, my sister Faranak, my brother Farzad, and my niece Elina for their unconditional love and care. My supportive parents have always pushed me toward my goals. My sister was my first mentor who introduced me to the interesting world of Physics. The friendship and supports of my brother have always made me feel strong and grounded. I am forever indebted to all of you.

Last but not least, I thank my wife Ramak for her endless love, patience, inspiration, and constant support. Thank you for staying by my side in each step of my life and helping me to reach my dreams. I am deeply thankful to you.

ABSTRACT

Since their emergence, locally resonant metamaterials have found several applications for the control of surface waves, from micrometer-sized electronic devices to meter-sized seismic barriers. The interaction between Rayleigh-type surface waves and resonant metamaterials has been investigated through the realization of locally resonant metasurfaces, thin elastic interfaces constituted by a cluster of resonant inclusions or oscillators embedded near the surface of an elastic waveguide. When such resonant metasurfaces are embedded in an elastic homogeneous half-space, they can filter out the propagation of Rayleigh waves, creating low-frequency bandgaps at selected frequencies. In the civil engineering context, heavy resonating masses are needed to extend the bandgap frequency width of locally resonant devices, a requirement that limits their practical implementations. In this dissertation, the wave attenuation capabilities of locally resonant metasurfaces have been enriched by proposing (i) tunable metasurfaces to open large frequency bandgaps with small effective inertia, and by developing (ii) an analytical framework aimed at studying the propagation of Rayleigh waves propagation in deep resonant waveguides.

In more detail, inertial amplified resonators are exploited to design advanced metasurfaces with a prescribed static and a tunable dynamic response. The modular design of the tunable metasurfaces allows to shift and enlarge low-frequency spectral bandgaps without modifying the total inertia of the metasurface. Besides, an original dispersion law is derived to study the dispersive properties of Rayleigh waves propagating in thick resonant layers made of sub-wavelength resonators. Accordingly, a deep resonant wave barrier of mechanical resonators embedded inside the soil is designed to impede the propagation of seismic surface waves. Numerical models are developed to confirm the analytical dispersion predictions of the tunable metasurface and resonant layer. Finally, a medium-size scale resonant wave barrier is designed according to the soil stratigraphy of a real geophysical scenario to attenuate ground-borne vibration.

Contents

1	Introduction	1
1.1	Literature Review	1
1.1.1	Phononic crystals	3
1.1.2	Elastic Metamaterials	5
1.1.3	Seismic Metamaterials	8
1.2	Applications and open issues	16
1.3	Thesis Objectives and outlines	18
1.3.1	Thesis objectives	18
1.3.2	Thesis Outlines	19
2	Design of a tunable metasurface with inertial amplified resonators	21
2.1	Introduction	21
2.2	Dynamics of the inertial amplified resonator	24
2.3	Dispersive properties of the IAR metasurface	29
2.3.1	Analytical model	29
2.3.2	Numerical verification	33
2.4	Transmission of a finite-length IAR metasurface	34
2.5	Conclusions	37
2.6	Acknowledgments	40
3	Rayleigh waves in resonant metamaterials	41
3.1	Introduction	42
3.2	Dispersion law of layered resonant medium	43
3.2.1	Resonant layer and effective medium description	44
3.2.2	Longitudinal and shear wave velocities in the anisotropic 2D continuum	46
3.2.3	Derivation of the dispersion relation	48
3.2.4	Limit case: Dispersion relation of a full resonant half-space	51
3.3	Case study: Dispersive properties of seismic barriers	52
3.3.1	Effective resonant layer model of the seismic barrier	54

3.3.2	Dispersive properties of a deep seismic barrier modeled as a resonant half-space	57
3.3.3	Dispersion of finite-depth seismic barriers	63
3.4	Transmission of a finite-length seismic barrier	69
3.5	Design of a resonant metamaterial plate	71
3.6	Conclusions	76
3.7	Acknowledgments	78
3.8	Funding	78
4	A medium-size scale resonant wave barrier	79
4.1	Introduction	80
4.2	A medium-scale resonant wave barrier	81
4.2.1	Experimental field site description	81
4.2.2	Description of the locally resonant wave barrier	82
4.3	Finite element analysis of the resonant barrier	84
4.3.1	Numerical dispersion analysis of the barrier	84
4.3.2	Time transient analysis	90
4.4	Frequency-variable resonant wave barrier	94
4.5	Preliminary Experimental Test Results	97
4.5.1	Instrumentation setup	98
4.5.2	Source characterization	99
4.5.3	Experimental Results	101
4.6	Conclusions	102
4.7	Acknowledgments	103
4.8	Funding	103
5	Conclusions	105
5.1	Conclusions of Chapter II	105
5.2	Conclusions of Chapter III	106
5.3	Conclusions of Chapter IV	107
5.4	Ongoing research	108
5.4.1	Experimental investigation of surface waves in a resonant metamaterial plate	109
5.4.2	Experimental assessment of an innovative proof-of-concept medium-size scale resonant wave barrier	110
5.5	Future outlook	113

List of Figures

1.1	Phononic Crystals vs. Metamaterials. Figures on the first row depict phononic crystals with (a) 1D [12], (b) 2D, and (c) 3D periodicity [13]. Figures on the second row depict metamaterials with (d) 1D [12], (e) 2D, and (f) 3D periodicity. Panel (b) is reproduced with permission [14], Copyright 2012, Elsevier. Panel (e) is reproduced with permission [15], Copyright 2012, AIP Publishing. Panel (f) is reproduced with permission [16], Copyright 2000, The American Association for the Advancement of Science.	3
1.2	(a) Schematics of a one-dimensional phononic rod modeled as a discretized spring-mass lattice. (b) Dispersion relation of a generic isotropic homogeneous medium, and (c) phononic crystal. The shaded area represents the spectral bandgap [27].	5
1.3	(a) A simple mass-spring model to describe the one-dimensional metamaterial with local resonance. (b) Dispersion relation of a generic isotropic homogeneous medium, and (c) locally resonant metamaterial. The shaded area represents the spectral bandgap [27].	7
1.4	(a) First experiment of seismic metamaterial [74]. (b) An example of phononic-based seismic metamaterial made of transparent cylindrical holes inside the soil. Panel (b) is reproduced with permission [10], Copyright 2020, Elsevier Ltd.	9
1.5	Resonant metafoundation (a) Isometric, and (b) plan view a storage tank isolated with resonant metafoundation. Reproduced with permission[87] Copyright 2019, John Wiley and Sons Ltd.	11
1.6	(a) Locally resonant seismic barrier. (b) The meter-sized surface resonator as the building block of the barrier. (c) Schematic of resonators interacting with Rayleigh waves. (d) Dispersion relation presents a low-frequency bandgap corresponding to the formation of local resonance mechanism [88].	12

1.7	Schematics of large-scale metamaterials (a) 3D and (b) cross-sectional (yz-plane) view. (c) Unit cells arranging the seismic metamaterial (top view). (d) The first Brillouin zone with the irreducible part. (e) Cross-like cavity unit cell. (f) Hollow cylinder unit cell. (g) Coated cylinder unit cell [72].	14
1.8	The resonant metawedge (a) The geometry and material properties. Displacement wavefield of the (b) classic, and (c) inverse metawedge. Panel (d) gives the theoretical versus numerical prediction, of the turning point position for various frequencies for the wedge in (a) [100].	15
1.9	Phononic-based seismic metamaterial (a) Side view, and (b) plan view of SMs around the protected building. Dispersion relations (c) clamped bedrock with no column, and (d) with rigid column [120].	17
1.10	Schematics of four lines of the metamaterial-based seismic defense system. (a) Metasurfaces to convert surface waves into bulk shear waves. (b) Metalenses to redirect seismic waves. (c) Perforated buried cylinders to convert seismic waves into sound. (d) Forest trees as locally resonant metasurfaces to attenuate surface waves. Reproduced with permission. [129], Copyright 2016, Elsevier Ltd.	17
2.1	(a) An example of a two-dimensional lattice structure with embedded inertial amplification mechanism. (b) Experimental test setup to measure the wide phononic bandgap. Reproduced with permission [158], Copyright 2013, Elsevier Ltd.	23
2.2	(a) Schematics of the advanced metasurface. (b) Schematic representation of an IAR resonator. (c) Effective medium description of the IAR metasurface modeled as a thin boundary condition (dark gray layer) on the top of a homogeneous half-space (light gray layer). (d) Representation of the vertical and tangential stresses at the interface and free surface above the metasurface.	24
2.3	(a) Equivalent mass of the IAR (m_I in Eq.(2.8)) normalized by the total resonator mass (m). (b) The resonant frequency of the IAR normalized by the resonant frequency of the equivalent SDOF oscillator for different internal angles ($10^\circ < \theta < 80^\circ$) and mass ratios ($\alpha = [0.25, 0.5, 0.75, 1]$). (c) The DAF of the IAR. (d) The anti-resonance frequency vs. internal angle for variation of the inertia ratio. Reproduced with permission [160], Copyright 2019, Springer Nature.	27

2.4	(a) Normalized base force of the IAR (f_b/f_s , where $f_s = KUg$). (b) Normalized zero-force frequency values with respect to the internal angle for the variation of mass ratio values. Reproduced with permission [160], Copyright 2019, Springer Nature.	29
2.5	(a) Dispersion curve of IAR metasurface in the high-frequency range. The dark gray region indicates the substrate sound cone, i.e., $c_p > c_T$. (b) Detail of the IAR low-frequency behavior. IAR metasurface dispersion curves for (c) variable mass ratios and $\theta = 30^\circ$ and for (d) variable internal angles with constant mass ratio $\alpha = 0.5$. (e) Frequency bandgap evolution for different mass ratios ($\alpha = 0.25$, $\alpha = 0.5$, and $\alpha = 1$). Reproduced with permission [160], Copyright 2019, Springer Nature.	32
2.6	(a) Schematic of the 2D IAR metasurface unit cell. (b) Dispersion curves as extracted from the Finite Element (FE) model (dots) and analytical dispersion law (continuous lines) for varying internal angles $\theta = [20^\circ, 30^\circ, 40^\circ]$. Panel (b) is reproduced with permission [160], Copyright 2019, Springer Nature.	34
2.7	(a) Schematics of a finite-length single-frequency resonant metasurface. (b) Schematics of the graded IAR metasurface of increasing internal angle $\theta = [10^\circ - 50^\circ]$ and constant mass distribution $\alpha = 0.5$.	35
2.8	(a) The vertical displacement field for a vertical harmonic excitation at the resonant frequency of the advanced metasurfaces. (b) The vertical displacement field of the z-axis is driven by a harmonic excitation at the zero-force frequency.	36
2.9	(a) Transmission coefficient of different IAR metasurfaces. (b) Transmission coefficient for the graded metasurface of IARs. Figures are reproduced with permission [160], Copyright 2019, Springer Nature.	38
2.10	Schematic of a possible design for a tunable IAR for seismic Rayleigh waves in (a) undeformed and (b) deformed configurations. Reproduced with permission [160], Copyright 2019, Springer Nature. . . .	39
3.1	Schematic of a resonant layer made of randomly distributed resonators overlying a non-resonant homogeneous semi-infinite medium. The inset shows a detail of the reference volume element (RVE). . .	44
3.2	Schematics of the reference volumes used for the calculation of the (a) effective longitudinal modulus M_{eff} and (b) effective shear modulus μ_{eff}	46
3.3	(a) Schematics of the resonant layer with a regular grid of embedded resonators overlying a homogeneous half-space. In the inset is shown a representative strip of the bilayered half-space. (b) Barrier unit cell.	53

- 3.4 (a) Schematics of the FE model used to calculate the longitudinal modulus M_{eff} , and (b) shear modulus μ_{eff} of the resonant barrier. Longitudinal strain (c) and stress (e) components are associated with the uniaxial constrained deformation state. Shear strain (d) and stress (f) components are associated with the pure shear deformation state. 55
- 3.5 (a) Developed FE unit cell in Comsol Multiphysics. (b) Numerical dispersion relation of the unit cell used to extract the equivalent shear and longitudinal velocities of the cell. 56
- 3.6 Effective properties of the resonant barrier. (a) Effective mass density. (b) Effective velocities of propagating bulk waves and (c) evanescent bulk waves. Shaded areas indicate the bandgap associated with negative EMD and purely imaginary values of the effective velocities. 58
- 3.7 (a) Real and (b) imaginary wavenumber for the dispersion of Rayleigh waves propagating across a full resonant half-space, respectively. (c) Real and (d) imaginary parts of the effective Rayleigh wave velocity in the resonant medium, respectively. 59
- 3.8 Rayleigh wave mode shapes in resonant half-space (continuous lines) and in the host medium (dashed lines) computed for a dimensionless circular frequency of (a) $\omega' = 0.8$ (in-phase), and (b) $\omega' = 1.5$ (out-of-phase). 60
- 3.9 (a) Schematic of a strip of the resonant half-space. (b) Dispersion relation of the resonant half-space. Solid lines present the analytical solutions, and circles mark the FE eigensolutions (blue dots denote the surface modes). (c) Zoom-in on the wavefield ($H = \lambda_0$) of a surface mode computed at $\omega' = 2.11$ and $k' = 0.3$ showing an out-of-phase displacement between the internal mass and the host medium; (d) rotating mode at $\omega' = 1.72$ and $k' = 0.3$; (e) surface mode computed at $\omega' = 0.91$ and $k' = 0.3$ with in-phase motion between the host medium and the internal resonant mass. 62
- 3.10 Dispersion relation of (a) propagating and (b) evanescent Rayleigh waves in a resonant layer with a depth of $H = \lambda_0$ overlaying a homogeneous half-space. The fundamental surface mode is marked by black lines. 64

3.11 Dispersion curves of real wavenumbers for a semi-infinite resonant medium consisting of a homogeneous half-space below a resonant layer with the depth of (a) $H = 0.2\lambda_0$, (b) $H = 0.5\lambda_0$, (c) $H = \lambda_0$, and (d) $H = 2\lambda_0$, respectively. (e) bandgap width in normalized angular frequency vs. normalized depth of the resonant layer. The dashed blue line indicates the BG upper edge of a resonant half-space, while the dashed red line indicates the upper edge for a metasurface. 66

3.12 (a) Schematic of the metasurface layer attached to the free surface of a homogeneous half-space. (b) Dispersion of the resonant layer composed of single unit cell embedded to host material(RL) vs. locally resonant metasurface(MS). 67

3.13 (a) FE surface modes (blue dots), discriminated according to the criterion reported in Eq. (3.42), and over-imposed to the analytical dispersion relation (solid lines) for $H = 0.2\lambda_0$ and (b) $H = \lambda_0$. (c) A representative unit cell of a resonant barrier on top of a homogeneous soil. (d) The vertical displacement wavefields of a leaky surface mode corresponding to $k' = 0.08$ and $\omega' = 1.33$. (e) The vertical displacement wavefield of the fundamental surface mode for $k' = 0.18$ and $\omega' = 1.54$. Note that the resonators move out-of-phase with respect to the host medium. 68

3.14 (a) Schematic of the FE model used for the calculation of the transmission coefficients. (b) Comparison of transmission coefficients $T(\omega')$ calculated for the seismic barrier and homogenized layer with an identical depth of $H = \lambda_0$ 70

3.15 Snapshots of the vertical displacement field (z-axis) for (a) the seismic barrier and (b) its equivalent resonant layer driven by a vertical harmonic excitation at $\omega' = 1$ and for (c) the seismic barrier (d) and (d) its equivalent resonant layer is driven by a vertical harmonic excitation at $\omega' = 1.3$ 71

3.16 Transmission coefficients of resonant layers with different thicknesses, $H = [0.2, 0.5, 1]\lambda_0$. The red box highlights the bandgap of $H = 0.2\lambda_0$, while the shaded gray region marks the bandgap of $H = 0.5\lambda_0$ and $H = \lambda_0$. (c) 72

3.17 (a) Schematics of the phononic cell. (b) Schematics of the resonant unit cell. Bulk waves dispersion curves for (c) the basic and (d) resonant cells, respectively. 73

3.18 (a) A zoom in the bulk dispersion of the resonant unit cell (see Fig.3.18b). (b) Bulk modes are obtained from eigenfrequency analysis of the unit cell. 74

3.19	(a) Bulk dispersion of the 3D resonant unit cell vs. equivalent 2D model. (b) Bulk modes of the equivalent 2D unit cell.	74
3.20	(a) Bulk dispersion of a resonant layer over a non-resonant PVC half-space over-imposed by the FE dispersion (red dots). (b) Schematics of the unit cell for FE Rayleigh mode extraction with the depth of $1 m$. The resonant part includes 5 resonators with a depth of one wavelength (λ). (c) Bulk dispersion with filtered surface modes. (d) Vertical displacement wavefield for in-phase and out-of-phase branches. Highlighted gray region denotes the low-frequency surface wave bandgap.	75
3.21	(a) 2D Schematic design of the resonant unit cell and (b) metamaterial plate. (c) 3D view of the designed metamaterial plate.	77
4.1	(a) Longitudinal and (b) shear waves speed profiles of the Euroseistest site. Reproduced with permission [177], Reproduced with permission, Copyright 2018, Elsevier Ltd.	82
4.2	(a) An array of 5 by 10 resonators forming the metabarrier design (top view). (b) Schematics of a single resonator. (c) Schematics of a dead mass placed over the soil layer without the presence of steel plates and springs. Reproduced with permission [162], Copyright 2020, Taylor and Francis.	83
4.3	(a) Reference soil model (RSM) unit cell. Dispersion curves in terms of (b) frequency vs. wavenumber, and (c) phase velocity vs. frequency. Analytical prediction of the fundamental mode according to Eq. (1) (red line) is over-imposed to the dispersion curves. Reproduced with permission [162], Copyright 2020, Taylor and Francis.	85
4.4	(a) Dead Mass (DM) unit cell. Dispersion curves in terms of (b) frequency vs. wavenumber, and (c) phase velocity vs. frequency. The over-imposed red curve in panel (b) has been obtained using Eq. (4.2). Reproduced with permission [162], Copyright 2020, Taylor and Francis.	86
4.5	(a) Resonant wave barrier (MB) unit cell. Dispersion curves in terms of (b) frequency vs. wavenumber, and (c) phase velocity vs. frequency. The curves reported as red lines in panel (b) have been obtained by Eq. (4.3). Reproduced with permission [162], Copyright 2020, Taylor and Francis.	88
4.6	(a) Buried Metabarrier inside a trench (MB) unit cell. Dispersion curves in terms of (b) frequency vs. wavenumber, and (c) phase velocity vs. frequency. The curves reported as red lines in panel (b) have been obtained by Eq. (4.3).	88

- 4.7 Normalized amplitude obtained from vertical nodal displacement for the dead mass (panel a) and metabarrier (panel b) cases vs. the RSM (dashed lines) at the resonant frequency of resonators ($f_r = 44 Hz$). In the presence of metabarrier, all the surface modes are characterized by a vanishing displacement at the soil surface (continuous lines in the panel (b)). 89
- 4.8 (a) Schematics of the full 2D FE model used in time history analyzes. (b) The layout of on-field experimental test setup (instrumentation, source offsets, and barrier arrangement). Reproduced with permission [162], Copyright 2020, Taylor and Francis. 91
- 4.9 Frequency spectra of the vertical displacement fields generated by a Ricker wavelet with a central frequency of $50Hz$ obtained from the measurement (a) along the barrier (e.g., output 1), and (b) after the barrier (e.g., output2) for the RSM, DM, and MB configurations. Reproduced with permission [162], Copyright 2020, Taylor and Francis. 92
- 4.10 Dispersion spectra obtained from 2D FFTs of the time-domain surface displacements for the DM and MB cases (output 1). The dispersion curves predicted by the WFEM models in the Sec.4.3.1 are over-imposed as continuous lines. The gray box denotes the Rayleigh-induced bandgap. Reproduced with permission [162], Copyright 2020, Taylor and Francis. 93
- 4.11 The vertical displacement field of (a) RSM, and (b) metabarrier (MB) configurations. Gray box denotes the bandgap region. Reproduced with permission [162], Copyright 2020, Taylor and Francis. 93
- 4.12 Mass distribution and the resonant frequency of the graded resonant barrier with increasing mass (a), and decreasing mass (b). Frequency spectra calculated along the graded barrier (output 1) with increasing mass (c), and decreasing mass (d) for a constant stiffness of the resonators. Frequency spectra after the graded barrier (output 2) with increasing mass (e), and decreasing mass (f) for a constant stiffness of the resonators ($K_{tot} = 9869.6 kN/m$). Reproduced with permission [162], Copyright 2020, Taylor and Francis. 95

4.13	Stiffness and the resonant frequency of the graded resonant barrier with increasing stiffness (a), and decreasing stiffness (b). Frequency spectra calculated along the graded barrier (output 1) with increasing vertical stiffness (c), and decreasing vertical stiffness (d) for a constant mass of the resonators. Frequency spectra are calculated after the graded barrier (output 2) with increasing vertical stiffness (e) and decreasing vertical stiffness (f) for a constant mass of the resonators ($M = 100$ kg). Reproduced with permission [162], Copyright 2020, Taylor and Francis.	96
4.14	Mass and resonant frequency of three random resonant barriers (a), (b), and (c), respectively. (d) Comparison between the frequency spectra (output 1) of the three random cases.	98
4.15	(a) On-field line measurement setup across DM length on soil pristine (T_0 setting) (b) Dead mass configuration (barrel with 100 kg of mass) atop of soil pristine (T_1 setting).	99
4.16	Sledgehammer impact. (a) The source excites the far-field from position 2, and sensor H (accelerometer) measures the response. (b) Signal time trace and mean of the FFTs of the recorded signal for the free field and (c) dead mass conditions.	100
4.17	Comparison between soil (RSM) and dead mass (DM) from (a) experimental tests, and (b) numerical simulations.	101
5.1	(a) A CNC machine is used to perforate the PVC plate. (b) Steel masses are press-fitted inside each basic cells of the plate. (c) The phononic unit cell is realized with four elastic connectors holding a resonating rigid mass. (d) Resonant metamaterial plate made by the regular repetition of the phononic cell. Metamaterial plate includes two barriers with different thicknesses (three and five rows of the resonant cells on the top and bottom edges of the plate, respectively).	110
5.2	(a) Experimental test setup. (b) Pristine PVC plate excited with a piezoelectric buzzer to generate surface waves. (c) The fundamental surface mode of the plate (e.g., $f=5$ kHz and $k=56$ rad/m) is obtained from FE analysis. (d) Surface wave dispersion obtained from FFT response in time and space for excitation at 5 kHz.	111
5.3	(a) Instrumented resonators without the presence of the static mass. (b) The realization of the prototype resonator as the building block of the medium-scale resonant wave barrier. (c) Instrumented resonators with 100 kg of the mass.	112

List of Tables

3.1	Mechanical parameters of the metamaterial plate.	72
-----	--	----

Chapter 1

Introduction

1.1 Literature Review

Controlling the propagation of mechanical waves through elastic media, sound and water waves in fluids, and electromagnetic waves in vacuum and material medium, have been studied for many years. Major scientific breakthroughs in the control of waves across different contexts and scales have been achieved in recent years thanks to the development of metamaterials. The term “Metamaterial” has emerged to describe rationally designed composite materials with extraordinary material properties not commonly observed in natural materials. Such an artificially structured composite is usually made of different elements fashioned in periodic or random arrangements. Peculiar characteristics of the metamaterials, which make them capable of manipulating the propagation of waves, are not inherited from single components but arise from the size, geometry, and arrangement of their artificially manufactured elements [1]. These elements are intentionally designed to have dimensions much smaller than the wavelength of incident waves. Such dimensions guarantee that the interaction between the metamaterials and phenomena they influence occurs at a sub-wavelength scale.

The concept of metamaterials has emerged in optics around a half-century ago where negative-index materials were theoretically introduced [2]. In 2000, left-handed metamaterials were practically developed to modulate electromagnetic waves through lenses [3]. The surge of various electromagnetic metamaterial designs was mainly due to the incorporation of the concept of photonic crystals. Photonic crystals are periodic optical crystals realized to control the propagation of light [4]. Functioning metamaterials have been evolved from the combination of periodic structures and photonic crystals to filter out the propagation of light waves with the wavelengths comparable to the metamaterial periodicity [5]. An example of such electromagnetic metamaterial is the periodic arrangement of split-ring resonators

notched on a dielectric substrate [6]. Electromagnetic metamaterials have later found their counterparts in different areas of science such as thermodynamics, classical mechanics (including acoustics, elastostatics, elastodynamics, and fluid dynamics) [7]. This paradigm shift has led to the born of acoustic and elastic metamaterials. In the context of acoustics, phononic crystals (PCs) were engineered to guide, hinder, and amplify the sound waves. The wave filtering property of phononic crystals relies on material periodicity. In the past few years, phononic crystals found broad applications in vibration control, noise reduction devices, acoustic cloaking, and waveguide structures [1].

In elastodynamics, sub-wavelength resonant units are incorporated in the design of metamaterials to inhibit the wave transmission in specific frequency ranges, namely bandgap (BG) frequencies [8]. Differently from phononic crystals, elastic metamaterials exploit resonance-induced bandgaps to impede mechanical wave propagation. Hence, more recently, elastic metamaterials have found numerous applications in mechanical and civil engineering fields such as ground-borne vibration mitigation devices and seismic isolation systems [9]. For the latter case, a new branch of elastic metamaterials, namely seismic metamaterials (SMs), has emerged. So far, the main target in earthquake engineering is to enhance the bearing capacity of the soil layer below the structures and to improve the strength of superstructures or infrastructure. Instead, seismic metamaterials propose a novel strategy completely different from the traditional methods to shield the vulnerable infrastructures/structures by attenuating, reflecting, and refracting the incoming seismic surface waves [10]. The seismic isolation performance of the seismic metamaterials has been experimentally validated at the geophysical scale in the past few years [11]. Within this context, the study and design of elastic metamaterials to mitigate the propagation of seismic surface waves are getting increasing attention.

Surface waves are mechanical waves that propagate along the surface of an elastic medium or along the interface between two different solid media. In seismology, surface waves are categorized into horizontally (e.g., Love waves) and vertically (e.g., Rayleigh waves) polarized waves. During an earthquake, the far-field elastic energy of seismic waves is mainly carried out by Rayleigh waves. Hence, the control of Rayleigh waves propagation is of paramount importance to safeguard existing structures. In this dissertation, we study and design locally resonant metamaterials to control the propagation of Rayleigh waves.

In what follows, a brief review of the basic concepts of the phononic crystals and elastic metamaterials is provided. Next, the state of the art and recent advancements of seismic metamaterials are extensively discussed. Finally, theoretical and practical limitations and open challenges on the application of resonant metamaterials for the control of elastic waves are discussed.

1.1.1 Phononic crystals

Phononic crystals (PCs) are usually defined as rationally designed materials made of the periodic distribution of scatterers or inclusions embedded in a host matrix that allow the manipulation of waves [1]. The emergence of phononic crystals was followed by the advancement of period structures. A periodic structure is made of a finite or infinite repetition of a unit cell, the smallest repeating portion of crystal structure possessing its full symmetry, in one, two, or three dimensions as shown in Fig. 1.1a, b, and c, respectively. The spatial periodicity of a periodic medium is either due to a repetition of different geometries or material phases.

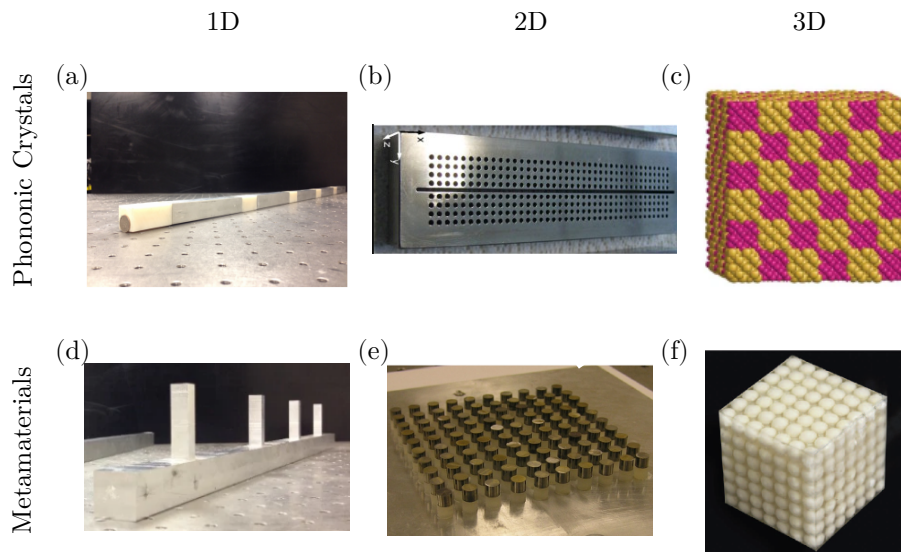


Figure 1.1: Phononic Crystals vs. Metamaterials. Figures on the first row depict phononic crystals with (a) 1D [12], (b) 2D, and (c) 3D periodicity [13]. Figures on the second row depict metamaterials with (d) 1D [12], (e) 2D, and (f) 3D periodicity. Panel (b) is reproduced with permission [14], Copyright 2012, Elsevier. Panel (e) is reproduced with permission [15], Copyright 2012, AIP Publishing. Panel (f) is reproduced with permission [16], Copyright 2000, The American Association for the Advancement of Science.

The idea of conceptualizing a composite material made of functional building blocks packed into a host material backs to 1873, when James Clerk Maxwell discussed the possibility of laminates [17]. Later on, the French physicist Léon Nicolas Brillouin studied wave propagation in the periodic media. In more detail, he studied the propagation of elastic waves in atomic vibrations (phonons), propagation of electromagnetic waves, and the interaction of periodic media with acoustic waves [18]. He discussed some fundamental concepts in periodic materials

including most notably Brillouin scattering, Brillouin function, Brillouin zone, and frequency bandgaps (BGs). The frequency bandgap is a frequency span in which the propagation of the waves is inhibited. Brillouin zone (or reciprocal space) is the representation wave properties of the corresponding infinite periodic system in the wave vector space (k-space). The first Brillouin zone which describes the dispersion relations of elastic waves can be calculated by using a unit cell. In physics, dispersion relations describe the effect of dispersion on the properties of waves propagating throughout a medium. Dispersion is the dependence of the wavenumber (or wavelength) to the wave frequency. In other words, dispersion relations also describe the phase and group velocity of waves. Wave scattering, Brillouin zones, and unit cell definitions are widely used to characterize the dynamic features of an ideal infinite periodic structures.

The development of periodic structures was remarkably contributed to the advancements of photonic and phononic crystals in the twentieth century. In 1979, a superlattice structure (a one-dimensional phononic crystal) was experimentally developed to control the propagation of high-frequency phonons [19]. During the early 1990s, two-dimensional and three-dimensional phononic crystals were conceived by Sigalas and Economou [20, 21]. They discussed the band structure of acoustic and elastic waves in three-dimensional structures composed of periodically distributed spheres in a host medium [20], and two-dimensional fluid and solid systems constituted of periodic arrays of cylindrical inclusions embedded in a matrix [21]. The full band structure of out-of-plane vibration of the two-dimensional periodic elastic composite was calculated by Kushwaha et al [22]. Later on, phononic crystals were used to hinder the propagation of longitudinal [23], transverse [24], Lamb [25], and Rayleigh waves [26] inside the stop-band frequencies observed in the band structure diagrams of different lattice structures.

Phononic crystals exploit the Bragg scattering mechanism to control the dispersion of waves. Bragg scattering is the scattering of waves by a periodic distribution of scatterers having dimensions comparable to the wavelength of the propagating waves. An example of a one-dimensional phononic crystal made by the repetition of two different materials is schematically shown in Fig.1.2a. A simple lumped-mass model, an infinite chain of discrete mass-spring system, is considered to simplify the physical description of the problem. The dispersion relation of the 1D phononic crystal (see Fig.1.2c) is obtained via the mass-spring model and compared to the dispersion of a one-dimensional elastic homogeneous material, as shown in Fig.1.2b. The formation of the Bragg scattering mechanism leads to the generation of a low-frequency bandgap (see the gray box in Fig.1.1c) in the first irreducible Brillouin zone. The formation of the bandgap mechanism highlights the wave filtering property of phononic crystals which opens the possibility of designing innovative and smart materials. During the past two decades, many researchers

have tried to employ periodic structures and phononic crystals to regulate elastic wave propagation in different wavelength scales.

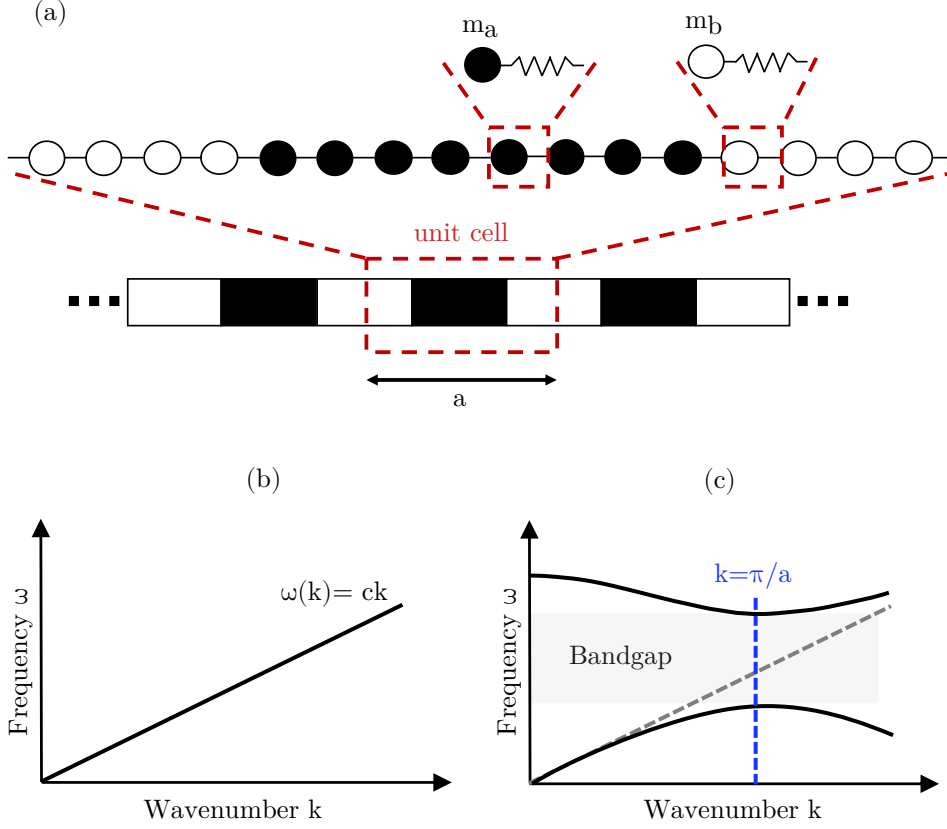


Figure 1.2: (a) Schematics of a one-dimensional phononic rod modeled as a discretized spring-mass lattice. (b) Dispersion relation of a generic isotropic homogeneous medium, and (c) phononic crystal. The shaded area represents the spectral bandgap [27].

1.1.2 Elastic Metamaterials

We discussed how periodic structures can substantially impact the propagation of waves. In this section, we present the concept of metamaterials as an alternative solution to achieve such a similar behavior without having limitations on the size of the structure. Periodic structures, photonic, and phononic crystals are sometimes defined as subclasses of metamaterials in the literature [7]. However, metamaterials have a broad definition and they are commonly referred to as artificial composite materials characterized by resonant units or inclusions embedded in the host medium of the composite. According to this definition, metamaterials can also be

non-periodic, although most of the designed metamaterials are realized as periodic composites.

Examples of one, two, and three-dimensional metamaterials are shown in Fig.1.1d, e, and f, respectively. The principal dynamic characteristic of the metamaterials is the generation of the local resonance mechanism. Under certain conditions, effective mass density and bulk-material properties of metamaterials can become negative at a narrow frequency band precisely located at the frequency ranges around the bandgaps associated with the collective resonances of resonant inclusion/resonators. A discrete mass-spring chain model with localized resonators each having an angular resonant frequency of ω_r , (see Fig.1.3a), is exploited to describe the dynamic features of a one-dimensional metamaterial rod. The dispersion relation of an elastic rod (e.g., Fig.1.3b) is compared to a metamaterial rod (e.g., Fig.1.3c). The introduction of the resonant units hybridizes the fundamental mode into two repelling branches and generates a sub-wavelength bandgap. Local resonance bandgaps, although narrow in their frequency band, allow the possibility to filter waves at specifically selected frequencies, control the low-frequency vibrations, and obtain a negative refraction index.

Acoustic Metamaterials The first conceptual realization of acoustic metamaterials is discussed in the work of Liu et al. [16] published in 2000. In this seminal work, a cubic sonic crystal consisting of a heavy solid core material (e.g., lead) coaxially coated with an elastic soft material (e.g., silicone rubber) embedded in a hard matrix material (e.g., epoxy) is studied (see Fig.1.1f). Two low-frequency bandgaps were generated corresponding to that of the local resonance of the lead and elastomer resonator, respectively. Since the wavelength of acoustic waves is orders of magnitude larger than the centimeter-sized cubic crystal, the interaction of waves and metamaterial occurs at the sub-wavelength scale. Within the sub-wavelength regime, the dynamics of the three-phase metamaterial can be appropriately described by using an “effective” description via multiple scattering theory [28]. This description yields a homogeneous material with effective mass density and effective elastic moduli characterized by a dynamic response equivalent to one of the composite media in the long-wavelength regime.

The notion of acoustic metamaterials together with the possibility of tuning the bandgap frequency generated by the local resonance mechanism has been a source of inspiration for designing metamaterials viable for wave propagation control in different scales. Following the advent of hard-soft-hard composite materials [29, 30, 31], different configurations have been proposed such as split-rings [32], hollow cylinders or spheres [33], trusses and beams equipped with internal resonators [34, 35], two-dimensional metamaterials [36, 37, 38], structures with inertial amplifiers [39, 40], membranes [37], chiral lattices [41, 42], metamaterials

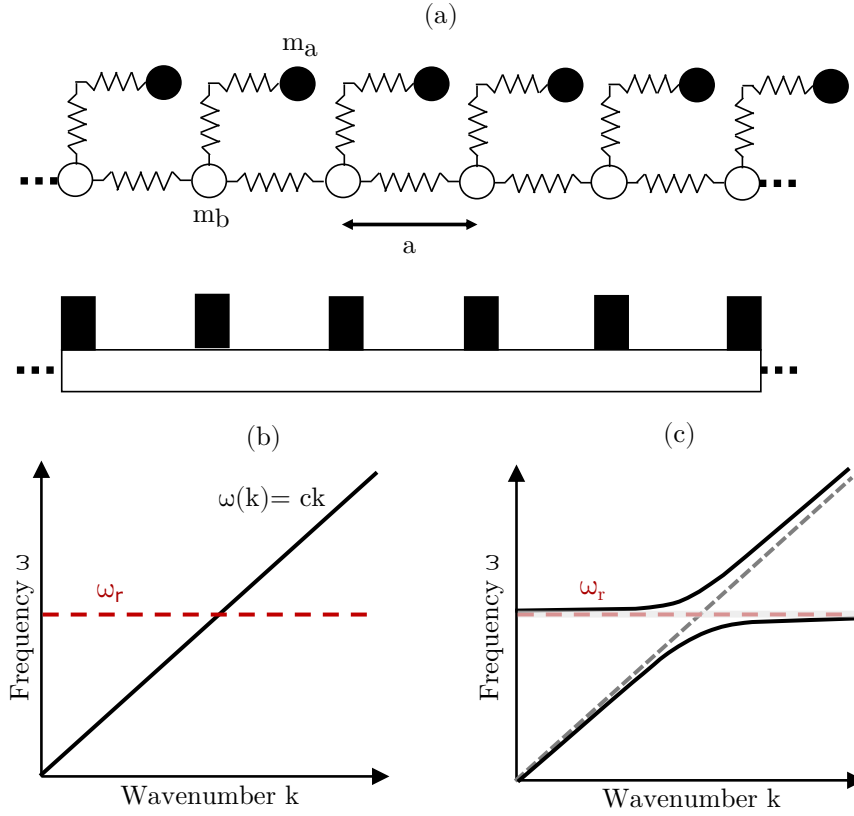


Figure 1.3: (a) A simple mass-spring model to describe the one-dimensional metamaterial with local resonance. (b) Dispersion relation of a generic isotropic homogeneous medium, and (c) locally resonant metamaterial. The shaded area represents the spectral bandgap [27].

with negative effective stiffness [43, 44], discrete mass-in-mass systems [45, 46], and three-dimensional architected media [47, 48]. More recently, the description of the resonant units has been enriched to account for viscoelastic material behavior [49, 50, 51, 52], nonlinearity [53, 54, 55], hierarchical geometry [56, 57], and time-dependent mechanical properties of metamaterials [58, 59, 60].

Furthermore, it is worth noting that several homogenization techniques have been used in the literature to retrieve the effective properties of the heterogeneous metamaterials, including static and dynamic homogenization, averaging techniques like retrieval methods, micromechanical techniques, Multiple Scattering, and Coherent Potential Approximation methods (see the review article [61] for a broader overview).

Inertial amplified metamaterials Several approaches have been proposed in the literature to enrich the dynamic properties and the operational frequency range of metamaterials. One strategy to enhance the dynamic response of metamaterials is to employ inertial amplification mechanisms, as originally proposed in Ref. [39]. An inertial amplification mechanism exploits inerters, rigid mechanisms designed to provide a force proportional to the relative acceleration between two points. This additional force can be used to generate resonant and anti-resonant responses, and to alter the frequency spectrum of discrete lattice materials [39, 40, 62] or continuous waveguides [63, 64] where these mechanisms are incorporated. More interestingly, Zhou et al. designed a nonlinear inertial amplification-based resonator to design a switch to control the propagation of flexural waves [65].

Inerters can be equivalently used to change the dynamic of mass-spring oscillators, as demonstrated in the design of dynamic vibration absorbers [66] and tuned mass dampers (TMDs) [67]. De Domenico et al. combined seismic isolation with a tuned-inerter damper, where they were able to simultaneously control the response of the base-isolated structures and superstructure [68]. Overall, inertial amplification can be classified as a different mechanism rather than Bragg scattering or local resonance mechanism and can be used to generate wide bandgaps in the low-frequency regime.

1.1.3 Seismic Metamaterials

Metamaterials have been introduced into the domain of mechanics after their successful implementations in acoustics and electromagnetism. For instance, elastic metamaterials have found numerous applications in civil engineering. In particular, metamaterial-based devices are proposed as an innovative solution to the existing seismic isolation techniques to mitigate the effects of seismic waves and thus shield historical sites, urban areas, as well as unprotected structures and infrastructures [69, 70, 71, 72, 73]. This class of devices, frequently indicated as “seismic metamaterials (SMs)” from the seminal work by Brule et al. [74] (see Fig. 1.4a), includes periodic and resonant foundations as well as periodic and resonant wave barriers able to interact with the propagation of seismic waves. Since then, different types of SMs have been developed. SMs can be classified into different categories. According to Kim and Mukunda [75], seismic cloaking and artificial shadow zone are two main methods to deflect and attenuate seismic waves. Brule et al. [10] classified SMs into five categories, namely seismic soil-metamaterials, buried mass-resonators, above-surface resonators, auxetic metamaterials, and other dissipative structures. A systematic and comprehensive review of the development of SMs has been done in 2020 by Mu et al. [9], where they classified SMs based on their arrangement, regulation mechanism, application, and performed experimental studies. In what

follows, we adopt a classification from the physical perspective of the SMs and based on their regulation mechanisms. As a result, SMs are divided into three main categories, namely phononic-based SMs, locally resonant SMs, and transformed urbanism.

I. Phononic-based SMs Inspired by phononic crystals concept, phononic-based SMs are developed exploiting the Bragg scattering mechanism to damp the propagation of seismic waves. In 1999, Meseguer et al. [26] experimentally studied the scattering of surface elastic waves through a periodic array of cylindrical holes in a marble quarry. Fifteen years later, seismic metamaterials were born when phononic crystals constituted by meter-size holes drilled in a periodic arrangement along the sedimentary soil surface (see Fig.1.4a) were experimentally tested to attenuate the propagation of soil vibration at frequencies around 50 Hz [74]. Additionally, Chen et al. conducted lab-scale experiments on SMs made of concrete piles and observed broadband frequency bandgaps (< 7.2 Hz) in the multilayered SMs together with the surface confinement of elastic waves [76]. Later on, different design approaches of the periodic pile barriers were used to attenuate surface waves in layered soil [77] and poroelastic half-space [78].

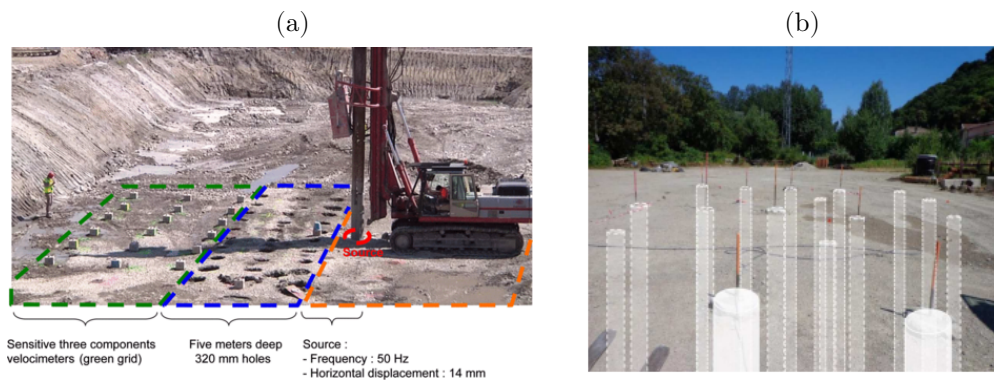


Figure 1.4: (a) First experiment of seismic metamaterial [74]. (b) An example of phononic-based seismic metamaterial made of transparent cylindrical holes inside the soil. Panel (b) is reproduced with permission [10], Copyright 2020, Elsevier Ltd.

Periodic foundations The concept of periodic (layered) foundations backs to the early 2010s. In 2012 Bao et al. proved that the seismic response of the structure equipped with a periodic foundation can be highly reduced in both vertical and horizontal directions for an arbitrary incident seismic wave [69]. Xiang et al. experimentally tested the periodic foundations by conducting the shaking table tests, where they were able to prove the existence of the attenuation zones

that seismic wave amplitudes were remarkably decreased [79]. Cheng and Shi developed two-dimensional composite periodic structures made of concrete, steel, and rubber materials characterized by a low-frequency attenuation zone (< 20 Hz) [80]. Shi et al. designed a three-dimensional periodic foundation able to damp the incoming seismic waves in any direction inside the effective attenuation zone [70]. Since then, efforts have been done to improve the efficiency of the periodic foundations by exploiting the concepts of the pentamode metamaterials [81], negative stiffness mechanism [82], damped-layer periodic foundation [83], directional attenuation zones [84], and combining the local resonance mechanism and dual-stiffness structures [85].

Although revolutionary in their conception, practical implementation of phononic-based SMs at the low-frequency range (< 30 Hz) characteristic of seismic events requires very large structures, since the wavelengths of typical seismic waves can be of several meters or decameters.

II. Locally resonant SMs Complementary to the phononic-based SMs, locally resonant SMs exploit an array of embedded locally resonant units to interact with propagating surface waves at a sub-wavelength scale. Therefore, for seismic waves characterized by long wavelengths, locally resonant metamaterials allow for the design and construction of more viable devices, i.e. of smaller and feasible spatial dimensions. On the basis of this paradigm, two classes of resonant metamaterials, namely resonant metafoundations, and metasurfaces have been proposed in recent years. Resonant metafoundations consist of a cascade of mass-spring systems embedded in the foundations to isolate the related substructure [86, 87, 82]. Resonant metasurfaces, instead, consists of an array of locally resonant units embedded close to the soil surface, capable of shielding buildings and infrastructures from surface Rayleigh [88, 89] or Love waves [90, 91, 92].

Resonant Metafoundations Inspired by the development of the metamaterials concept, resonant metafoundations were proposed as a novel solution for seismic protection of the foundations and superstructure. Finite locally resonant metafoundations are realized as foundations with embedded resonators. They are characterized by attenuation zones in which seismic waves can be dissipated and non-attenuation zones where the response of the superstructure is amplified [93]. Resonant metafoundations can be either implemented to the unprotected structure alone or simultaneously with another seismic protection system. Colombi et al. combined two metamaterial-based isolation strategies, namely metasurface and metafoundation, to shield a typical structure and pointed out that the incorporated design approach remarkably enlarges the mitigation bandwidth of seismic surface waves [94].

Apart from the seismic isolation application of resonant metafoundations for the buildings and structures, they have been used to shield critical industrial structures against seismic action [82]. La Salandra et al. conceptualized the design of three-dimensional resonant metamaterial consist of periodically arranged locally resonant units for the seismic protection of storage tanks [86]. Later on, Basone et al. experimentally tested a finite locally resonant metafoundation designed to support storage fuel tanks [87], which is shown in Fig.1.5. Franchini et al. proposed a metafoundation realized by steel columns placed between concrete slabs with concrete resonators to protect slender tanks against seismic actions with a significant vertical acceleration [95].

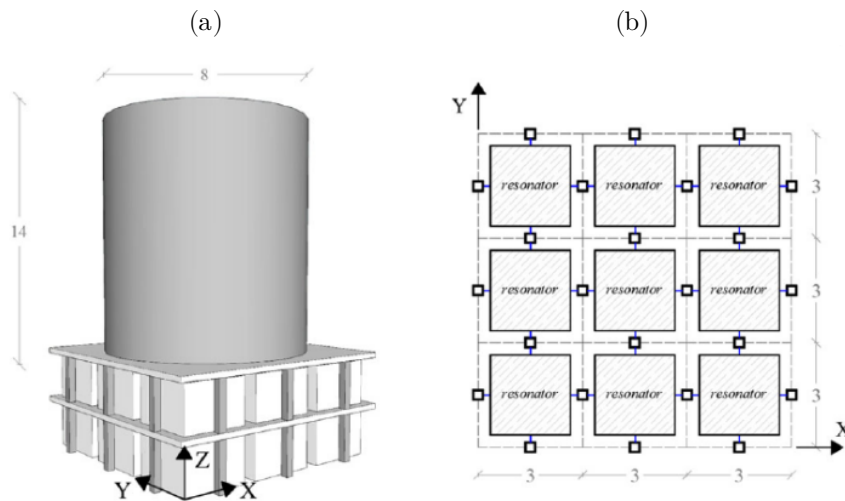


Figure 1.5: Resonant metafoundation (a) Isometric, and (b) plan view a storage tank isolated with resonant metafoundation. Reproduced with permission[87] Copyright 2019, John Wiley and Sons Ltd.

Despite the great advances in the design of metafoundations, their practical applications in civil engineering are still limited due to the lack of study on the bearing capacity of the foundations, stability of superstructure, and their cost of realization.

Resonant Metasurfaces The idea of a resonant metasurface, in particular, is motivated by the fact that far from the epicenter surface waves can carry a significant portion of the earthquake energy [96] and that existing structures may be hard to be retrofitted with conventional foundation systems. The resonant metasurfaces found their principle basis on the interaction between purposely engineered resonant units with surface waves in the low-frequency regime (<10 Hz). The resonant units are generally mass-stiffness resonators, embedded near-surface

or placed directly atop of the soil and excited by the vertical component of the Rayleigh wave motion (see Fig.1.6a). When the resonant units are arranged at the free surface of an elastic waveguide, to form a so-called *metasurface*, the propagation of waves confined at the soil surface can be controlled. Once activated, the dynamic interaction of metasurfaces with the soil steers part of the elastic Rayleigh wave energy into the interior stratum of the soil deposit as bulk shear waves [88, 97].

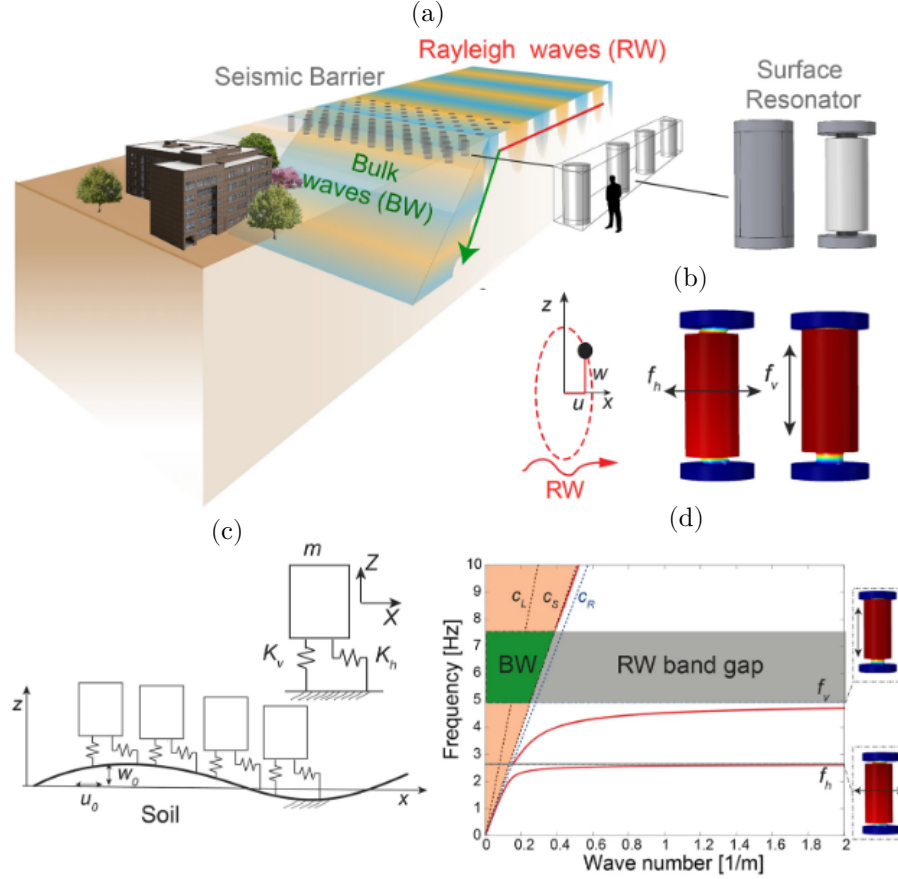


Figure 1.6: (a) Locally resonant seismic barrier. (b) The meter-sized surface resonator as the building block of the barrier. (c) Schematic of resonators interacting with Rayleigh waves. (d) Dispersion relation presents a low-frequency bandgap corresponding to the formation of local resonance mechanism [88].

In 2016, Colombi et al. found out that periodically arranged pine trees of a forest in Grenoble, France can be treated as a natural resonant metasurface [98]. In their experiments, longitudinal resonances of the trees were coupled to Rayleigh waves, resulted in the generation of multiple bandgap frequencies. The thought-provoking results of this research inspired many researchers to design engineered metasurfaces

able to attenuate surface seismic waves in the low-frequency regime. Palermo et al. [88] designed tailored metasurfaces made of a periodic arrangement of steel masses suspended by elastic bearings encased in concrete shells, embedded close to the surface of an idealized soil (see Fig.1.6a and b). The strong impedance mismatch between the resonators and Rayleigh wave opened up a narrow frequency bandgap in the spectrum of Rayleigh wave, as shown in the shaded area of Fig.1.6d. More interestingly, surface Rayleigh to bulk shear wave conversion is observed in the sound cone (e.g., frequency region near bandgap where only purely shear modes propagate). The filtering and wave conversion effects were predicted by deriving ad-hoc dispersion laws formulated by considering the metasurfaces as a dynamic boundary condition for the elastic waveguides [99]. Besides, Colquitt et al. theoretically studied the flexural and compressional resonances of seismic metasurfaces (modeled as periodic rods placed over an elastic homogeneous semi-infinite medium) coupled to Rayleigh wave [97].

Some strategies have been proposed to enlarge the narrow Rayleigh-induced bandgap frequencies. Among those, Miniaci et al. combined the Bragg scattering (cross-like cavity and hollow cylinder) and local resonant cylinders made of steel/concrete mass suspended by rubber material embedded in the soil, to design large-scale SMs (see Fig.1.7) [72]. The designed metamaterials were able to successfully attenuate both the surface waves (e.g., Rayleigh waves) and bulk waves in the low-frequency regime. Colombi et al. proposed a seismic metawedge made of spatially graded sub-wavelength resonant rods (with increasing or decreasing resonant frequency) placed over an elastic half-space (see Fig.1.8a). Hence, the classic resonant metawedge reflects the Rayleigh waves and exhibits a seismic “rainbow trapping effect” (see Fig.1.8b). Conversely, inverse resonant metawedge (see Fig.1.8c) converts surface Rayleigh waves into bulk shear waves [100]. Palermo et al. tackled the problem and proposed multi-mass seismic metasurfaces using an analytical approach followed by numerical verification. The multi-mass metasurfaces were able to create multiple bandgaps in the dispersion relation of Rayleigh waves and increase the bandwidth of the ground motion attenuation zone [101].

The soil characteristics highly influence the propagation velocity and amplitude decay of the seismic surface waves. In the above-mentioned studies, soil material is considered as an idealized homogeneous and elastic material for simple mathematical treatment purposes. Palermo et al. studied the heterogeneity effect of soil in the interaction of Rayleigh waves and elastic metasurfaces by experimentally testing the surface wave propagation in a multi-layer granular material. Although a surface wave attenuation is observed around the resonant frequency of the resonators, the generation of Rayleigh-induced bandgap typical of the homogeneous medium is hindered by higher-order surface modes [102]. Pu et al. investigated the interaction of Rayleigh waves with elastic metasurfaces attached to a porous layered media,

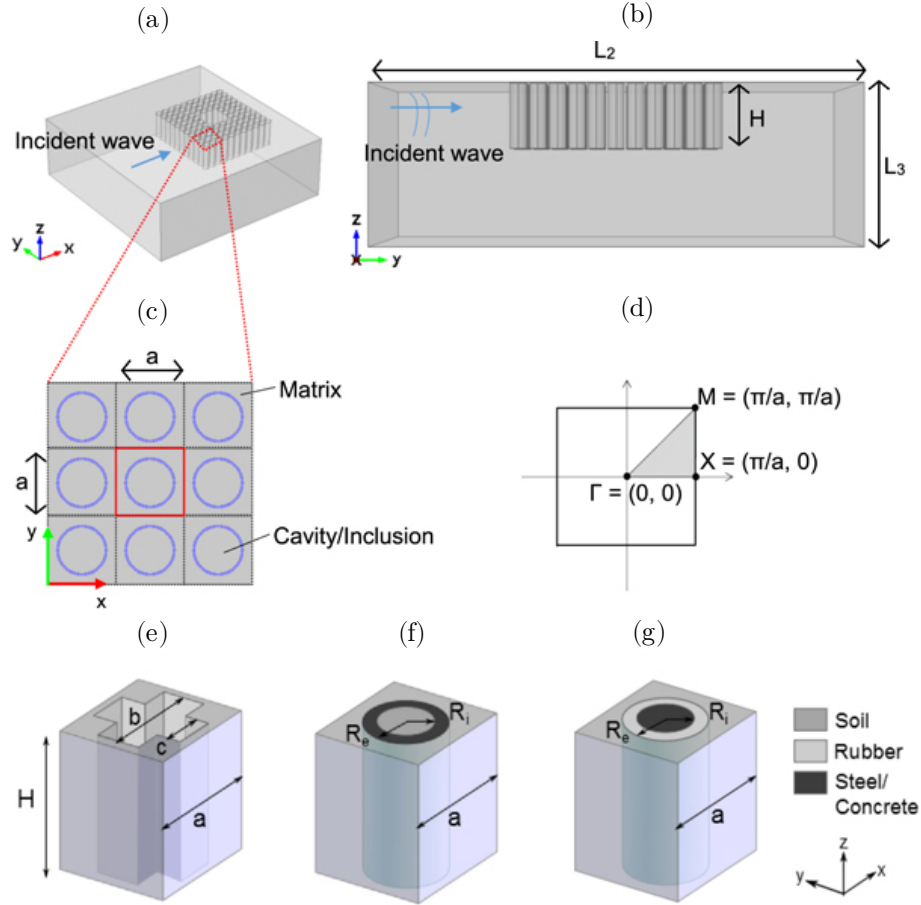


Figure 1.7: Schematics of large-scale metamaterials (a) 3D and (b) cross-sectional (yz -plane) view. (c) Unit cells arranging the seismic metamaterial (top view). (d) The first Brillouin zone with the irreducible part. (e) Cross-like cavity unit cell. (f) Hollow cylinder unit cell. (g) Coated cylinder unit cell [72].

where due to the fluid-solid interaction surface waves propagate in the form of slow pressure waves [103].

Complementary to Rayleigh waves, locally resonant metasurface were conceived to control also the propagation of horizontally polarized surface waves (i.e. Love waves). Palermo and Marzani designed gradient-index metalenses (Maxwell and Luneburg lenses) to redirect the propagation of Love waves [104]. In a complementary study, Palermo et al. discussed the effect of the metasurface inertia on the dispersion of love waves [92] where large inertial masses increase surface confinement of fundamental surface mode. Maurel et al. studied the possibility of wave trapping

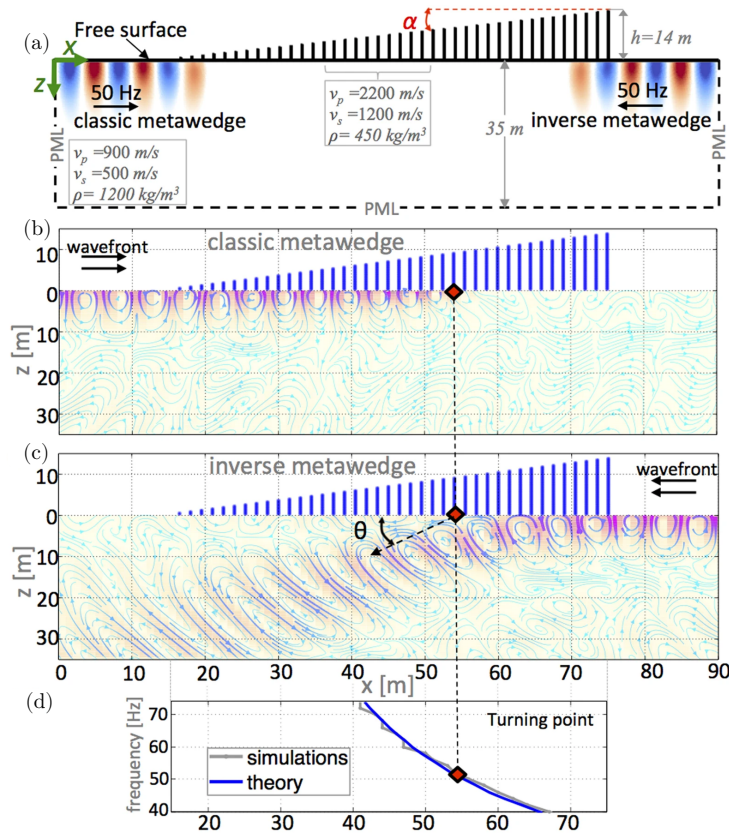


Figure 1.8: The resonant metawedge (a) The geometry and material properties. Displacement wavefield of the (b) classic, and (c) inverse metawedge. Panel (d) gives the theoretical versus numerical prediction, of the turning point position for various frequencies for the wedge in (a) [100].

and surface Love wave conversion in a forest tree [91]. Zaccherini et al. conducted a table-top to experimentally study the interaction of horizontally polarized surface waves and locally resonant metasurface in a granular medium [105], where a frequency attenuation zone is observed while the surface to bulk conversion is prevented by the depth-dependent profile of the unconsolidated granular medium.

More recently, several approaches have been proposed to enrich the dynamic response of the locally resonant metasurfaces. Active metasurfaces are designed through piezoelectric materials to tune the frequency response of the resonators [106, 107, 108, 109]. Time-modulated resonators are incorporated as nonlinear metasurface for unidirectional waveguiding of Rayleigh waves [110, 111]. The rainbow trapping in elastic metasurfaces is exploited for elastic energy harvesting [112, 113]. Furthermore, Chaplain et al. coupled surface Rayleigh waves to reversed bulk shear and compressional waves to achieve tunable redirection and wave focusing

inside the bulk material [114]. Although some important physical aspects of the resonant metasurface were carefully analyzed through recent years, the seismic isolation performance of the metasurfaces is still unexplored and did not tackle by the above-mentioned studies.

III. Transformed urbanism Introduced in optics, the concept of negative refraction has been exploited to design transformed crystals for elastic waves manipulation exploiting Snell's law. In recent years and after the manifestation of SMs, the transformed mechanism has been used to propose seismic cloaks to manipulate the seismic wavefront and shield a target structure behind the cloak [115, 116]. In transformation elastodynamics, seismic cloaking is the ability to render a district of buildings invisible to the incident seismic wave, which can be achieved by exploiting restricted and unrestricted micropolar medium [117] and Willis equations [115]. As an example, a periodic arrangement of concrete columns with variable dimensions has been proposed to modify the velocity of seismic waves and reroute them around a protected area [118], exploiting concepts of ray theory and lens designing. Brule et al. considered buildings of a neighborhood as subsurface elastic resonators, capable to interact with seismic waves, to design a seismic cloak [119].

Henceforth, a periodic arrangement of rigid columns embedded in a soft and thin sedimentary basin overlaying the bedrock (see Fig.1.9a and b) constituted a surface waves reflector [120]. Interestingly, the designed SMs proved the possibility of opening a broadband zero-frequency stopband in the frequency spectrum of seismic surface wave, as shown in the dispersion curve of Fig.1.9d. Another class of seismic cloaks is proposed using auxetic metamaterials combining effects of impedance mismatch, local resonances, and Bragg scattering mechanisms [121].

For more detailed reviews on the previous studies and advancements of phononic crystals, acoustic/elastic, and seismic metamaterials, the readers may refer to Ref [122, 123], [124, 125, 126], and [9, 10], respectively.

1.2 Applications and open issues

Periodic and locally resonant metamaterials are rapidly expanding research fields with promising future applications in the context of wave propagation manipulation. Local resonance and Bragg scattering allow the possibility to control waves in different wavelength scales, from micrometer [127] to meter-size scale [88, 128]. In the low-frequency regime, seismic metamaterials were proposed to impede the propagation of seismic surface waves [98, 72, 88], as described in Sec.1.1.3. Fig.1.10 summarizes some examples of metamaterial-based defense systems designed to shield critical structures or infrastructures prone to seismic hazards [129].

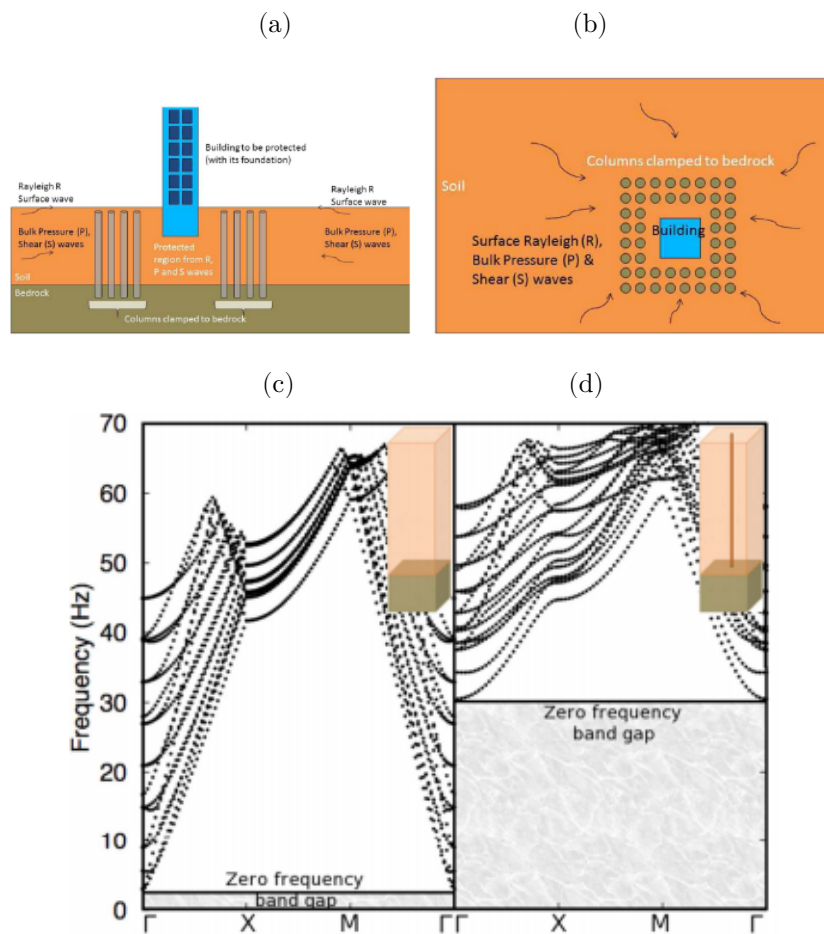


Figure 1.9: Phononic-based seismic metamaterial (a) Side view, and (b) plan view of SMs around the protected building. Dispersion relations (c) clamped bedrock with no column, and (d) with rigid column [120].

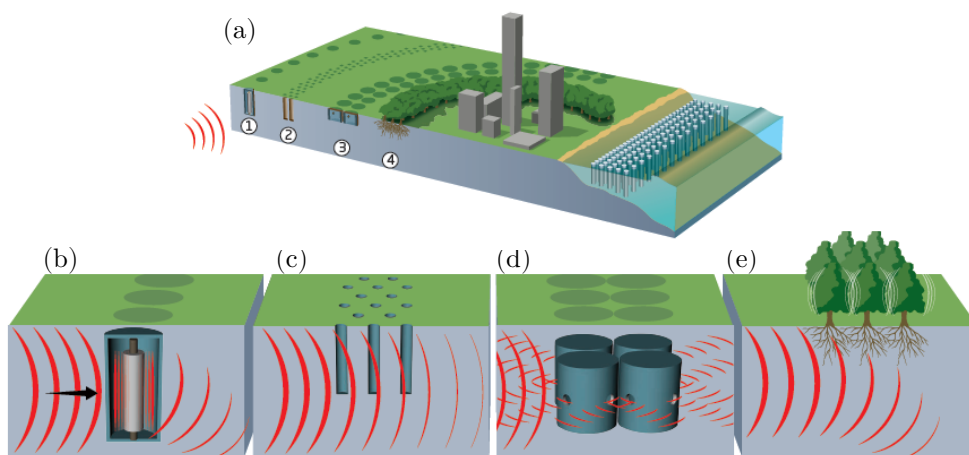


Figure 1.10: Schematics of four lines of the metamaterial-based seismic defense system. (a) Metasurfaces to convert surface waves into bulk shear waves. (b) Metalenses to redirect seismic waves. (c) Perforated buried cylinders to convert seismic waves into sound. (d) Forest trees as locally resonant metasurfaces to attenuate surface waves. Reproduced with permission. [129], Copyright 2016, Elsevier Ltd.

Although the dynamics of the resonant wave barriers are well-described by analytical models [88, 97, 128] and numerical simulations [88, 101, 130], experimental validations of these devices are still limited to a few small-scale experiments for surface Rayleigh [88, 102, 131], and shear waves [105]. At the geophysical scale, the coupling between surface waves and distributed resonators has been evinced only by analyzing the propagation of ground vibrations through forest trees [98]. Indeed, to be able to open considerable spectral bandgaps, large structures with very heavy resonating mass are required. This limitation restricts the engineering application of metasurfaces for seismic isolation. The trade-off between the amount of resonant mass and the attenuation efficiency of these devices, together with concerns about the structural integrity of these systems, are open issues that require in-depth investigations supported by experimental evidence suggesting first the design of medium-scale experiments, able to test the dynamics of real resonators on the field.

So far, the investigations on the metasurfaces are limited to resonant units embedded very close to the surface or placed at the surface layer of the elastic waveguides. Hence, the scenarios where resonators are distributed through the whole medium depth or within a thick surface layer overlying a homogeneous half-space are still unexplored. Understanding the dynamics of these systems is fundamental to ease the development of novel devices, like barriers and foundations, to control and mitigate the propagation of Rayleigh waves.

1.3 Thesis Objectives and outlines

1.3.1 Thesis objectives

This dissertation aims to investigate the dynamics of the Rayleigh-type surface waves propagating in locally resonant metasurfaces, and to address some of the open questions and existing challenges discussed in the previous section. To this end, three main objectives are set as follows:

1. Design advanced metasurfaces with a tunable dynamic response;
2. Investigate the dynamics of surface waves propagating in a finite-thickness resonant layer made of bulk resonant metamaterials;
3. Design of a medium-scale resonant wave barrier considering the effects of soil heterogeneity properties (stratification, topography, etc).

1.3.2 Thesis Outlines

The dissertation is organized as follows. In Chapter 2, an advanced metasurface is proposed exploiting the kinematics of the inertial amplified mechanism. The chapter comprises the derivation of an analytical closed-form dispersion law for Rayleigh waves propagating in a homogeneous half-space equipped with a resonant boundary layer made of Inertial Amplified Resonators (IARs). Next, 2D finite element models are developed according to the wave finite element method to validate analytical dispersion curves. Further numerical simulations are carried out to show and discuss the transmission coefficients of different IAR metasurface configurations and to design graded metasurfaces for wideband Rayleigh waves attenuation.

In Chapter 3, the dynamics of resonant layers with variable thicknesses composed of randomly distributed resonators over the whole depth of the layer are studied. In particular, the dispersion relations of a finite-depth resonant layer laid over a homogeneous half-space, and an infinite-depth resonant half-space are derived analytically. Dispersion laws are then validated by numerical simulations. A resonant seismic wave barrier is designed according to the analytical/numerical findings of the resonant layer concept, and harmonic analyses are performed via finite element simulations to evaluate the seismic attenuation performance of the proposed resonant barrier.

In Chapter 4, the numerical design procedure of an experimental campaign aimed at assessing the surface ground motion attenuation performance of a medium-size scale resonant wave barrier within the frequency range of 50 – 100 Hz is presented. Hence, the soil stratification and its in-situ properties (obtained from Euroseistest site) as well as the components, and arrangement of the proposed wave barrier are described. Then, the seismic isolation performance of the barrier through a numerical dispersion analysis is tested, and numerical predictions are made via time transient simulations. Eventually, graded resonant barriers are designed, to achieve broadband seismic wave attenuation.

Finally, Chapter 5 provides a summary of the main findings discussed in previous chapters, briefly reviews the ongoing research activities, and gives an insight into the possible future research directions.

Chapter 2

Design of a tunable metasurface with inertial amplified resonators

Abstract

The chapter studies the design principles of an advanced locally resonant metasurface able to manipulate the propagation of surface waves. The metasurface consists of a cascade of Inertial Amplified Resonators (IARs), e.g., mechanical resonators coupled with two inerters suspended by two inclined rigid links which are connected to an additional mass encased in a rhomboid geometry. The IAR has a static behavior equivalent to that of a single-degree-of-freedom (SDOF) oscillator whereas its dynamic response can be controlled by means of the effective inertia of the resonators and their geometrical configuration. A closed-form dispersion law is derived analytically to study the interaction between Rayleigh waves and the advanced metasurface coupled to an elastic half-space. The proposed metasurface presents some unique dynamic features including a tunable dynamic response to shifting its bandgap frequency without altering the mass or stiffness of the resonators. Moreover, the tunability feature of the metasurface allows the design of graded metasurfaces for broadband filtering purposes, and to obtain a high-frequency behavior typical of dead masses which contributes to having additional filtering properties. The analytical findings of the chapter are verified via finite element numerical simulations.

2.1 Introduction

Elastic metasurfaces have been developed as a novel class of locally resonant metamaterials capable to interact with the incoming waves. Locally resonant metasurfaces are realized as a dynamic boundary layer attached to the surface of an

elastic waveguide [132]. The resonant boundary layer usually consists of the periodic arrangement of sub-wavelength scale resonant units (e.g., resonant inclusions or oscillators). Locally resonant metasurfaces provide several applications among different fields in recent years. In electromagnetism, smart metasurfaces allow the realization of superlens [133, 134, 135], and electrically small resonators are used to design metasurface antennas [136, 137]. In acoustics, acoustic metasurfaces were designed for controllable transmission [138, 139], controllable reflection [140], and near-perfect absorption purposes [141, 142]. The main applications of the acoustic metasurfaces noted in the literature are self-bending beams [139], beam focusing [143], sound-absorbing of acoustic metamaterial beams [144], and asymmetrical transmission [145]. The readers may refer to Ref. [146] for an extensive literature review of the acoustic metasurface.

Later on, elastic metasurfaces are proposed to manipulate the elastic wave propagation [88, 97], or to design transmission metasurface for elastic solids [147, 148]. In elastodynamics, resonant metasurfaces made of pillars and surface or embedded resonant structures are used to design elastic waveguides [149, 99, 110], metalenses [118, 90], and surface wave filtering metastructures [98, 150].

Garova et al. conceptualized one of the simplest realizations of elastic metasurfaces by considering a sub-wavelength arrangement of discrete mass-spring resonators attached to the free waveguide of an elastic semi-infinite media [151]. Elastic metasurfaces exploit the locally resonant mechanism of the resonators to open up frequency bandgaps and to change the surface wave trajectory direction into bulk media across different length scales [152, 153, 118]. The bandgaps are generated around the collective resonant modes of the resonators $\omega_{r,S} = (K/m)^{1/2}$, where (K) is the stiffness and (m) is the mass of the resonators. One of the main limitations of the classical elastic metasurfaces is that for a given static response (prescribed mass and stiffness), the dynamic response of the metasurface is determined. To overcome this limitation, we propose the design of an advanced locally resonant metasurface with a tunable dynamic response in this chapter.

Complementary to the Bragg scattering and local resonance, the Inertial Amplification Mechanism (IAM) is proposed by Yilmaz et al. in 2007 as an alternative mechanism to enlarge phononic bandgaps of elastic metamaterials [39]. In this mechanism, the effective inertia of the dynamic system is amplified via inerters or embedded amplification mechanisms [39].

Inerters are proposed for low-frequency vibration control, where they can achieve large dynamic inertia while retaining the static mass of the dynamic system to the minimum value [154, 155]. Inerters have found various applications in the usage of tuned-mass-dampers (TMDs) [67, 156], lattice structures [157], and dynamic vibration absorbers (DVAs) [66].

An embedded inertial amplification mechanism has been used in different lattice

structures to enhance their dynamic responses. In 2D lattice structures, IAM generates large effective inertial forces by amplifying the small static mass of the system [39]. This additional force generates resonant and anti-resonant responses and modifies the frequency spectrum of discrete 2D (see Fig.2.1) [39, 40, 158] as well as 3D lattice structures [62, 159].

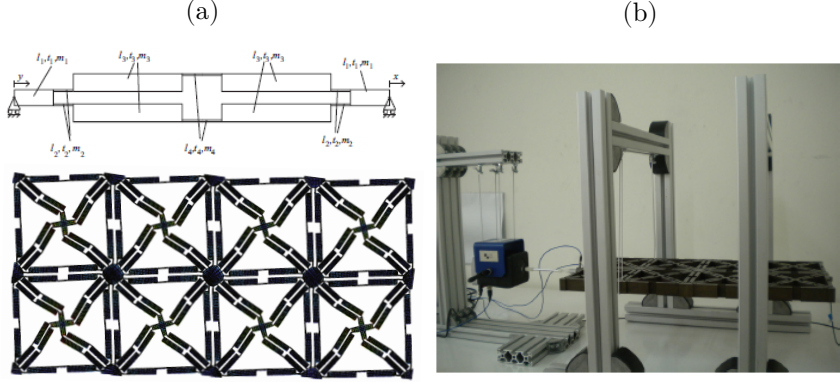


Figure 2.1: (a) An example of a two-dimensional lattice structure with embedded inertial amplification mechanism. (b) Experimental test setup to measure the wide phononic bandgap. Reproduced with permission [158], Copyright 2013, Elsevier Ltd.

Inspired by the tunable dynamic nature of the IAM, we design an advanced metasurface in this chapter. To this end, an array of near-surface Inertial Amplified Resonators (IARs), i.e., mass-spring oscillators with embedded amplification mechanism, manifests the metasurface design. The IAR consists of the SDOF resonator coupled with two rigid lateral mechanisms, carrying each an additional mass, able to amplify or attenuate the inertia of the oscillator [39].

The IAR, characterized by the same overall static mass (m) and stiffness (K) of the mass-stiffness oscillator, presents an enriched dynamic response, i.e., resonance, anti-resonance, and high-frequency behavior, which can be controlled by the geometrical configurations and the mass distribution of the amplification mechanism. The dynamic response of the IAR is obtained through the Dynamic Amplification Factor (DAF), which is the ratio between the static and maximum dynamic displacement of the resonator, as well as the vertical force which is translated to the base of the resonator. We exploit the tuning properties of IAR to realize a metasurface of whose frequency bandgap and high-frequency response can be changed by varying the geometrical configuration of the IAR. We discuss these dynamic properties through the derivation of a closed-form dispersion relation specialized for the IAR metasurface and investigating its transmission properties through numerical simulations.

2.2 Dynamics of the inertial amplified resonator

In this section, we analyze the main dynamic properties of the Inertial Amplified Resonator (IAR) as a building block of the advanced metasurface. The IAR configuration comprises a mass-stiffness block (m_T, K) attached to two lateral inertia (m_L) linked via four rigid connectors oriented at an angle $0^\circ < \theta < 90^\circ$ with respect to the vertical z -axis, as schematically shown in Fig. 2.2b. The far-ends of the rigid connectors and the spring are realized by moment-free hinges to prevent the generation of bending moments. The vertical spring of the IAR enables translational motion of the top mass in the vertical direction while the horizontal motion of the IAR is neglected. An identical mechanism has been studied in Ref.[40] to generate low-frequency and wide stopbands in periodic lattice structures.

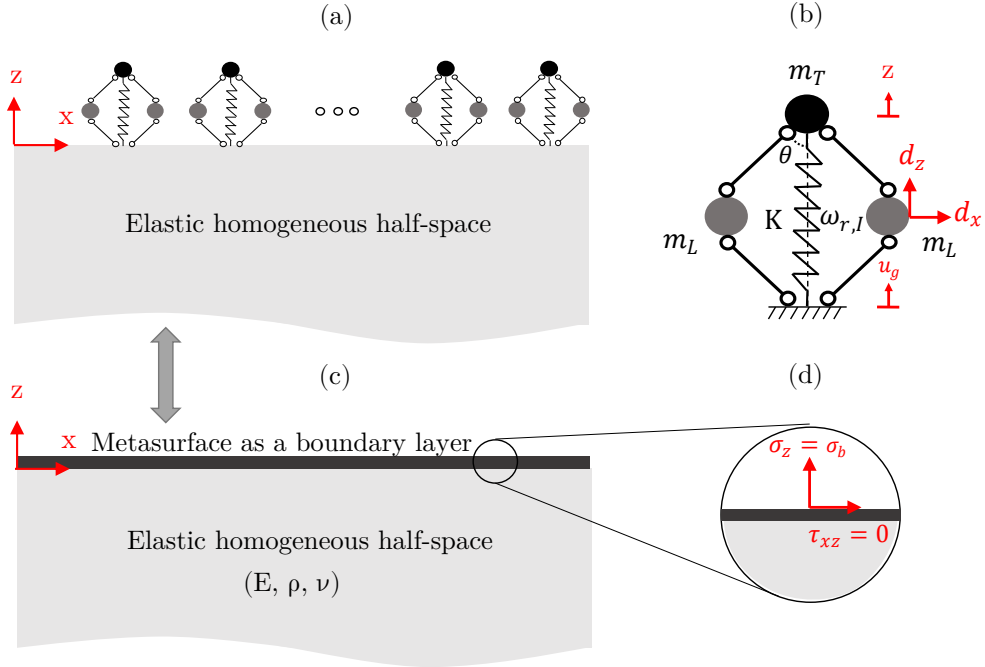


Figure 2.2: (a) Schematics of the advanced metasurface. (b) Schematic representation of an IAR resonator. (c) Effective medium description of the IAR metasurface modeled as a thin boundary condition (dark gray layer) on the top of a homogeneous half-space (light gray layer). (d) Representation of the vertical and tangential stresses at the interface and free surface above the metasurface.

We begin our investigation by formulating the IAR dynamic response for the case of harmonic base excitation. To do so, the dynamic amplification factor (DAF) and the vertical force at the base of the proposed resonators is formulated.

The force exerted by the resonator to the base is a fundamental element that is used lately to couple dynamics of the IAR to an elastic semi-infinite medium (see Fig.2.2a and Sec.2.3).

The equation of motion (EOM) of the top mass m_T in terms of absolute vertical displacement, evaluated under the small displacement assumptions, namely around the IAR undeformed configuration defined by a constant internal angle θ , reads:

$$m_T \ddot{z} + \frac{1}{2} m_L \left(\ddot{z} + \ddot{u}_g \right) + \frac{1}{2} m_L \left(\frac{\ddot{z} - \ddot{u}_g}{\tan^2 \theta} \right) + K(z - u_g) = 0 \quad (2.1)$$

where u_g is the ground displacement.

Eq. (2.1) exploits additional linearized inertia forces due to the embedded lateral masses with respect to the inertia of a single-degree-of-freedom (SDOF) oscillator. These additional inertia contributions have emerged from the horizontal and vertical displacements of the extra embedded mass terms, respectively

$$d_x = \frac{u_g - z}{2 \tan \theta}, \quad d_z = \frac{z + u_g}{2} \quad (2.2)$$

In particular, the term:

$$f_{ine} = \frac{1}{2} m_L \left(\frac{\ddot{z} - \ddot{u}_g}{\tan^2 \theta} \right) \quad (2.3)$$

stems from the relative acceleration between the top mass and the resonator base highlighting the contribution of an additional inerter. The benefit of the proposed advanced metasurface is to have the ability to alter the properties of the inerter by means of modifying the geometrical properties (i.e., internal angle of the rhomboid geometry θ) of the locally resonant metasurface.

By introducing the dimensionless mass ratio $\alpha = m_T/m$, where $m = m_T + 2m_L$ is the total inertia of the advanced IAR, the resonator equilibrium equation, Eq. (2.1), can be rearranged as:

$$\alpha m \ddot{z} + \frac{1}{4} m (1 - \alpha) \left(\ddot{z} (1 + \cot^2 \theta) + \ddot{u}_g (1 - \cot^2 \theta) \right) + K(z - u_g) = 0 \quad (2.4)$$

The following investigations on the dynamics of the IAR metasurface are limited to the internal angles ranging in the interval of $10^\circ < \theta < 80^\circ$ in order to have a meaningful physical explanation.

We derive the dynamic amplification (DAF) of the IAR by imposing a harmonic base motion, i.e., $u_g = U_g e^{i\omega t}$, and considering a time-harmonic response $z = Z e^{i\omega t}$ as:

$$D(\omega, \alpha, \theta) = \frac{Z}{U_g} = \frac{K + \frac{m\omega^2}{4}(1 - \alpha)(1 - \cot^2 \theta)}{K - \frac{m}{4}(3\alpha + 1 + \frac{1 - \alpha}{\tan^2 \theta})\omega^2} \quad (2.5)$$

The resonance $\omega_{r,I}(\alpha, \theta)$ and anti-resonance frequencies $\omega_{ar,I}(\alpha, \theta)$ of the IAR are obtained respectively for $D(\omega_{r,I}, \alpha, \theta) \rightarrow \infty$ and $D(\omega_{ar,I}, \alpha, \theta) \rightarrow 0$:

$$\omega_{r,I}(\alpha, \theta) = \sqrt{\frac{K}{\frac{m}{4}(3\alpha + 1 + \frac{1-\alpha}{\tan^2\theta})}} = \sqrt{\frac{K}{m_I}} \quad (2.6)$$

$$\omega_{ar,I}(\alpha, \theta) = \sqrt{\frac{K}{\frac{m}{4}(1-\alpha)(\cot^2\theta - 1)}} \quad (2.7)$$

where m_I in Eq. (2.6) represents an equivalent mass of the resonating system:

$$m_I = \frac{m}{4} \left(3\alpha + 1 + \frac{1-\alpha}{\tan^2\theta} \right) \quad (2.8)$$

From Eq.(2.8), one can conclude that for $\theta = 30^\circ$, the equivalent mass m_I becomes identical to the total inertia of the advanced metasurface m , independently from the mass distribution factor α (cf. Eq. (2.9)).

$$m_I = m \iff 3(\alpha - 1) = \frac{1-\alpha}{\tan^2\theta} \iff \theta = 30^\circ \quad (2.9)$$

Fig. 2.3a presents the equivalent inertia of the IAR resonator, normalized by its total inertia, with respect to the internal angle θ .

The DAF of an SDOF resonator can be recovered for $\alpha = 1$ as:

$$D(\omega, 1, \theta) = \frac{\omega_{r,S}^2}{\omega_{r,S}^2 - \omega^2} \quad (2.10)$$

and similarly, the natural angular frequency of the standard SDOF resonator can be recovered as $\omega_{r,I}(1, \theta) = \omega_{r,S} = (K/m)^{1/2}$. We leverage the natural frequency of the SDOF resonator to introduce the non-dimensional frequencies:

$$\omega' = \frac{\omega}{\omega_{r,I}(1, \theta)}, \quad \omega'_{r,I}(\alpha, \theta) = \frac{\omega_{r,I}(\alpha, \theta)}{\omega_{r,I}(1, \theta)}, \quad \omega'_{ar,I}(\alpha, \theta) = \frac{\omega_{ar,I}(\alpha, \theta)}{\omega_{r,I}(1, \theta)}$$

Fig. 2.3b shows that the non-dimensional angular resonant frequency of the IAR $\omega'_{r,I}(\alpha, \theta)$ can be controlled by modification of the introduced design parameters α and θ . With a prescribed total inertia m and stiffness K , the natural frequency of the IAR can be significantly modified even with a minimal modification of the mass distribution, for instance, $\alpha = 0.75$. For $\theta = 30^\circ$ regardless of the variation of the α values, the IAR natural resonant frequency becomes identical to one of the SDOF resonators, as it can be inferred from Eq. (2.6).

The absolute dynamic amplifications of two different advanced resonator configurations, namely, $D(\omega', 1, \theta)$, i.e. the one for the equivalent SDOF resonator, and

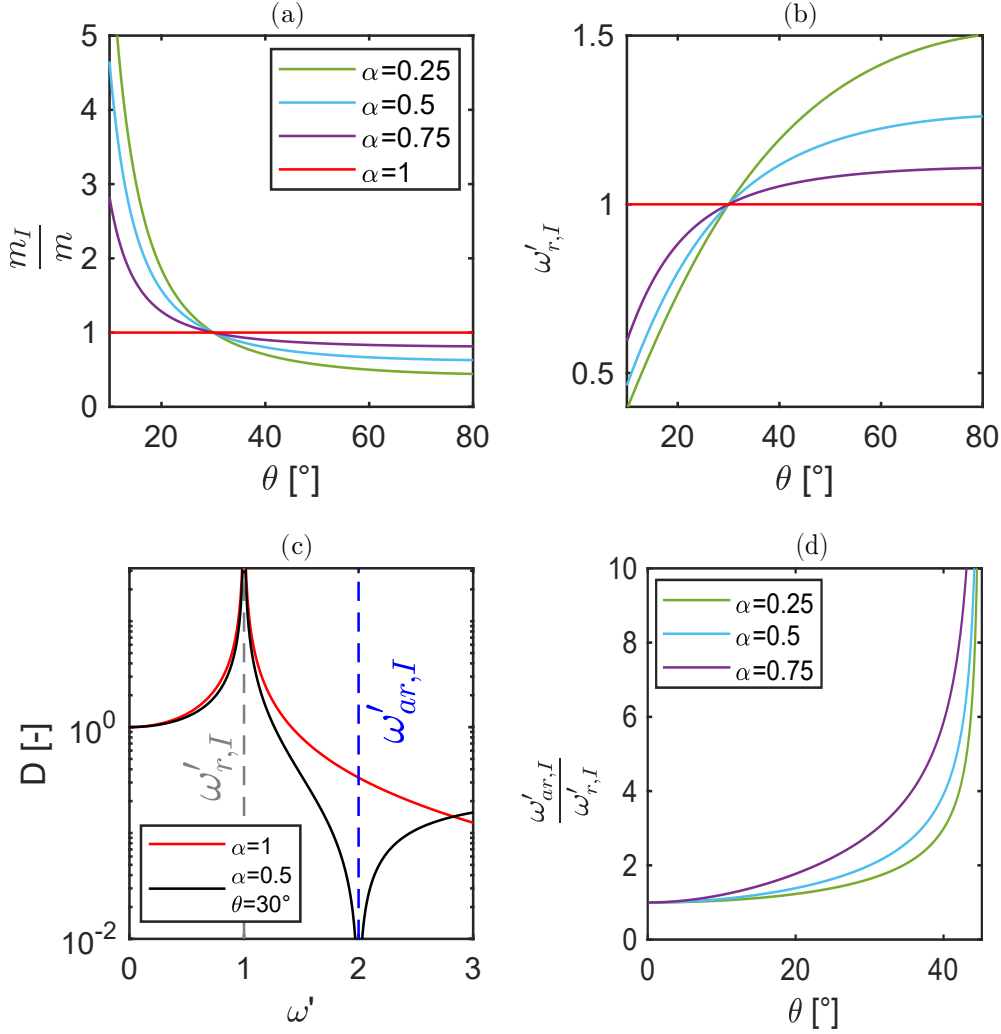


Figure 2.3: (a) Equivalent mass of the IAR (m_I in Eq.(2.8)) normalized by the total resonator mass (m). (b) The resonant frequency of the IAR normalized by the resonant frequency of the equivalent SDOF oscillator for different internal angles ($10^\circ < \theta < 80^\circ$) and mass ratios ($\alpha = [0.25, 0.5, 0.75, 1]$). (c) The DAF of the IAR. (d) The anti-resonance frequency vs. internal angle for variation of the inertia ratio. Reproduced with permission [160], Copyright 2019, Springer Nature.

$D(\omega', 0.5, 30^\circ)$, are shown in Fig. 2.3c. Indeed, the high-frequency limit ($\omega' \rightarrow \infty$) of the IAR dynamic amplification converges to a non-null value:

$$\lim_{\omega' \rightarrow \infty} D(\omega', \alpha, \theta) = \frac{(1 - \alpha)(\cot^2 \theta - 1)}{3\alpha + 1 + \frac{1 - \alpha}{\tan^2 \theta}} \quad (2.11)$$

on the contrary with a standard SDOF resonator, for which $D(\omega' \rightarrow \infty, 1, \theta) = 0$. This unique feature of the IAR has a remarkable effect on the high-frequency response of the IAR metasurface, as will be discussed later in Sec. 2.3. Furthermore, similar to the resonance, the anti-resonant response of the IAR can also be tuned by the modification of the introduced design parameters θ and α , cf. Eq (2.7). Particularly, Fig. 2.3d reveals the dependence of the IAR anti-resonance $\omega_{ar,I}$, normalized by the IAR angular resonance $\omega_{r,I}$, with the variation of the geometrical design parameter. The anti-resonance frequency is bounded by the IAR resonance ($\omega'_{ar,I} > \omega'_{r,I}$ for any θ), and gives rises for an increasing internal angle, diverging at $\theta = 45^\circ$.

Next, we investigate the amount of vertical force exerted by the IAR to the base, to be able to investigate the dynamic interaction of the IAR resonator with an elastic substrate. The vertical force transferred at the base of IAR is derived by exploiting the equilibrium of forces as:

$$f_{b,I}(\omega', \alpha, \theta) = mU_g \left(\frac{1}{4} \omega'^2 (1 - \alpha) (1 + D + \frac{1 - D}{\tan^2 \theta}) + \frac{m_I}{m} \omega'^2_{r,I} (D - 1) \right) \quad (2.12)$$

and can be compared to the vertical force transferred to the base of standard SDOF oscillator:

$$f_{b,I}(\omega', 1, \theta) = f_{b,S} = mU_g (D(\omega', 1, \theta) - 1) \quad (2.13)$$

The comparison between the base force exerted by the IAR and standard SDOF resonators is shown in Fig. 2.4a. In the low-frequency range, IAR transfers less vertical stress to its base in comparison with the SDOF resonator since part of the elastic force is used to counter-balance the horizontal displacement of the embedded lateral inertia system. On the contrary, the IAR behaves similarly to an extra dead mass, with a base force proportional to the vertical acceleration, in the high-frequency regime. This phenomenon is completely different from the dynamic behavior of the standard mass-spring oscillator, which instead transfers a negligible force in the high-frequency regime ($f_{b,I}(\omega', 1, \theta) \rightarrow 0$ for $\omega' \rightarrow \infty$). Eventually, we report the observation of the third frequency value of interest, where the base force of the IAR becomes zero:

$$\omega'_{f_0}(\alpha, \theta) = \omega'_{r,I} \sqrt{1 + \frac{(1 + \alpha)^2 \tan^2 \theta}{(1 - \alpha)(1 + \alpha \tan^2 \theta)}} \quad (2.14)$$

which we label as zero-force (or equivalently zero-stress) frequency. We remark that the zero-force frequency is always larger than the resonant frequency of IAR (See Eq. (2.14)), and it gives rise to an increase in the introduced design parameters α, θ , as shown in Fig. 2.4b.

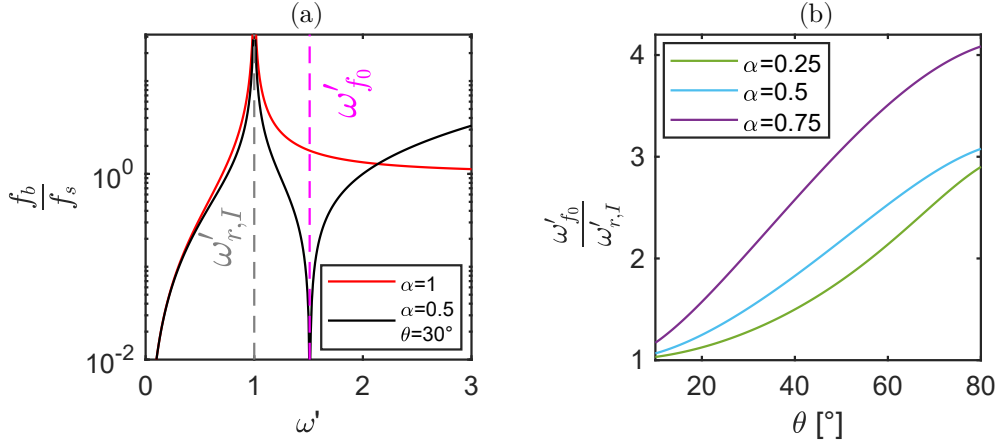


Figure 2.4: (a) Normalized base force of the IAR (f_b/f_s , where $f_s = KUg$). (b) Normalized zero-force frequency values with respect to the internal angle for the variation of mass ratio values. Reproduced with permission [160], Copyright 2019, Springer Nature.

2.3 Dispersive properties of the IAR metasurface

2.3.1 Analytical model

This section studies the dynamics of Rayleigh wave propagation in a homogeneous half-space equipped with an IAR metasurface layer attached to its free surface. We exploit the effective medium approach [153] as a simple analytical approach to discuss the dynamics of the IAR metasurface couple to an elastic semi-infinite half-space. Such an approach has been used in the study of the classical metasurface [88, 90, 92].

According to the effective medium approach, IAR metasurface comprises regularly distributed sub-wavelength oscillators that transfer uniform vertical stress over the surface of the elastic homogeneous semi-infinite medium. This uniform stress distribution is calculated from the base force (f_b) of each oscillator over an average influence area (S), defined from the regular spatial arrangement of the IAR oscillators over the waveguide surface. Accordingly, the IAR metasurface is modeled as an effective boundary condition for the elastic medium, as depicted in Fig. 2.2c. Indeed, the IAR metasurface exerts only the vertical stress ($\sigma_b = f_{b,I}/S$) to the elastic half-space.

Following the analytical approach for the derivation of the dispersion law of the Rayleigh waves from Ref. [96], we can derive an original dispersion law to

describe the coupling between the IAR metasurface and the vertically polarized surface waves. As such, we replace the standard zero-stress boundary conditions at the surfaces of half-space with the stresses exerted by the IAR metasurface to the elastic substrate. The closed-form dispersion of Rayleigh waves propagating along the x -axis of an elastic medium of longitudinal velocity c_L , shear velocity c_T , density ρ , and interacting with generic vertical resonators exerting a base force f_b reads [150]:

$$\left(2 - \left(\frac{\omega'}{k'}\right)^2\right)^2 - 4\sqrt{1 - \left(\frac{\omega'\gamma}{k'}\right)^2} \sqrt{1 - \left(\frac{\omega'}{k'}\right)^2} = \frac{-f_b\omega'^2}{S\rho c_T k'^3 \omega_{r,I}(1, \theta)} \sqrt{1 - \left(\frac{\omega'\gamma}{k'}\right)^2} \quad (2.15)$$

where $\gamma = c_T/c_L$ and $k' = k \cdot c_T/\omega_{r,I}(1, \theta)$ is the dimensionless wavenumber. This relationship can be specialized for the IAR metasurfaces by replacing the force at the base f_b with the one of the IAR as Eq. (2.12):

$$\begin{aligned} & \left(2 - \left(\frac{\omega'}{k'}\right)^2\right)^2 - 4\sqrt{1 - \left(\frac{\omega'\gamma}{k'}\right)^2} \sqrt{1 - \left(\frac{\omega'}{k'}\right)^2} \\ &= \Upsilon \frac{\omega'^4 \sqrt{1 - \left(\frac{\omega'\gamma}{k'}\right)^2}}{k'^3 \left(\left(\frac{\omega'}{\omega_{r,I}}\right)^2 - 1\right)} \left(1 - \left(\frac{\omega'}{\omega_{r,I}}\right)^2 \left(\frac{(1-\alpha)(1+\alpha \tan^2 \theta)}{1-\alpha + \tan^2 \theta(1+3\alpha)}\right)\right) \end{aligned} \quad (2.16)$$

where the parameter Υ :

$$\Upsilon = \frac{m\omega_{r,I}(1, \theta)}{S\rho c_T} \approx \frac{m}{S\rho\lambda_{\omega_{r,I}(1, \theta)}} \quad (2.17)$$

represents an approximate ratio between the inertia of the IAR and the inertia of a Rayleigh wave at a reference resonant frequency $\omega_{r,I}(1, \theta)$.

The roots of the Eq. (2.16) return the dispersion relation of Rayleigh waves and IAR metasurface as shown in Fig. 2.5a and b, for an IAR metasurface with $\Upsilon = 0.59$, $\gamma = 0.53$, $\theta = 30^\circ$ and $\alpha = 0.5$. Moreover, we demonstrate that the dispersion curve for $\alpha = 1$ is identical to the standard SDOF resonators metasurface in Fig. 2.5b. According to the dispersion relations, the IAR metasurface presents a classical avoided-crossing behavior in the low-frequency regime, where the fundamental Rayleigh wave is hybridized around the resonant frequency of the IARs, resulting in the generation of a surface waves bandgap. Surface to shear wave conversion is also achieved for the case of the IAR metasurface in the frequency range close to the collective resonant frequencies of the resonators analogous to what has been observed for Rayleigh waves interacting with classical SDOF resonators [153, 88].

On the contrary, surface waves are characterized by lower velocities $c_p < c_R$ in the high-frequency regime, with a dispersive behavior similar to the one, observed for an elastic half-space with additional dead mass atop, following the behavior observed for the IAR force response. This hypothesis is confirmed by the high-frequency approximation $\omega' \gg \omega'_{r,I}$ of the IAR dispersion relation in Eq. (2.16), which reads:

$$\left(2 - \left(\frac{\omega'}{k'}\right)^2\right)^2 - 4\sqrt{1 - \left(\frac{\omega'\gamma}{k'}\right)^2} \sqrt{1 - \left(\frac{\omega'}{k'}\right)^2} = -\Upsilon \frac{\psi(\alpha, \theta)\omega'^4}{k'^3} \sqrt{1 - \left(\frac{\omega'\gamma}{k'}\right)^2} \quad (2.18)$$

The factor $\psi(\alpha, \theta)$:

$$\psi(\alpha, \theta) = \frac{(1 - \alpha)(1 + \alpha \tan^2 \theta)}{1 - \alpha + \tan^2 \theta(1 + 3\alpha)} \quad (2.19)$$

allows mapping the approximate IAR dispersion law in Eq. (2.18) to the one of a semi-infinite homogeneous substrate with an additional mass attached to its free surface $m_{add} = m\psi(\alpha, \theta)$. Indeed, a mass-loading m_{add} applied over the free surface of an elastic medium exerts uniform vertical stresses, σ_{am} , proportional to the vertical acceleration of the substrate:

$$\sigma_{am} = -\frac{m_{add}\omega^2}{S} U_g e^{i\omega t} \quad (2.20)$$

where U_g is the vertical displacement at $z = 0$. Hence, following Eq.(2.15) we can derive the dispersion law for a layer of added masses distributed on the free surface of a homogeneous half-space:

$$\left(2 - \left(\frac{\omega'}{k'}\right)^2\right)^2 - 4\sqrt{1 - \left(\frac{\omega'\gamma}{k'}\right)^2} \sqrt{1 - \left(\frac{\omega'}{k'}\right)^2} = \frac{-m_{add}\omega'^4 \omega_{r,I}(1, \theta)}{S\rho c_T k'^3} \sqrt{1 - \left(\frac{\omega'\gamma}{k'}\right)^2} \quad (2.21)$$

The reader can appreciate the similarity between Eq. (2.21) and Eq. (2.18).

In the frequency region between the upper edge of the bandgap and the zero-force frequency, the upper dispersive branch has a phase velocity $c_R < c_p < c_T$, where c_R is the Rayleigh wave velocity. The zero-force frequency marks the condition when $c_p = c_R$, where the IAR metasurface becomes transparent to the Rayleigh waves propagation.

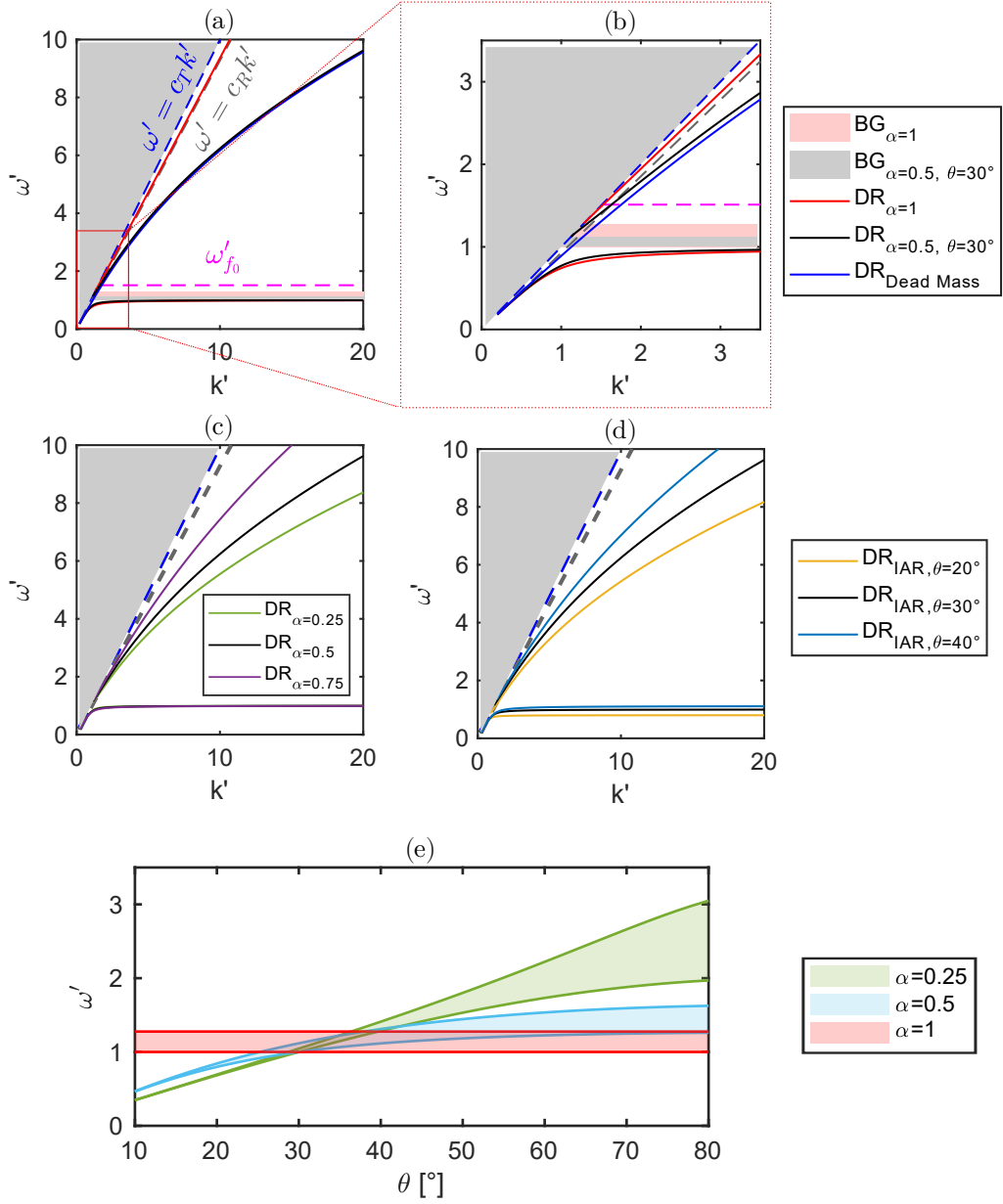


Figure 2.5: (a) Dispersion curve of IAR metasurface in the high-frequency range. The dark gray region indicates the substrate sound cone, i.e., $c_p > c_T$. (b) Detail of the IAR low-frequency behavior. IAR metasurface dispersion curves for (c) variable mass ratios and $\theta = 30^\circ$ and for (d) variable internal angles with constant mass ratio $\alpha = 0.5$. (e) Frequency bandgap evolution for different mass ratios ($\alpha = 0.25$, $\alpha = 0.5$, and $\alpha = 1$). Reproduced with permission [160], Copyright 2019, Springer Nature.

We take advantage of the tunable dynamic response of the IAR with respect to its design parameters to tune the dispersive characteristics of the advanced metasurface. Fig. 2.5c and 2.5d emphasize how the variation of the design parameters α and θ can modify the dispersion curves of the IAR metasurface. As an example, for a constant internal angle $\theta = 30^\circ$, an increase in the mass distribution ratio results in a surge in the phase velocity of the upper dispersive branch. Similarly, for a constant $\alpha = 0.5$, larger values of the internal angle θ result in higher phase velocities of the upper-frequency branch, as displayed in Fig. 2.5d.

The bandgap frequency ranges are also influenced by the modifications of the design parameters, as shown in Fig. 2.5e. The bandgap width widens for larger inertia distribution and also larger internal angle θ . Lower frequency bandgaps occur at the expense of their frequency width, as observed in other resonant metamaterials. Conversely, higher frequency resonances allow for broader attenuation bands.

2.3.2 Numerical verification

We develop a 2D finite element model in Comsol Multiphysics [161] following Bloch's theorem [18] to validate the analytically derived dispersion laws of the IAR metasurface. In this regards, we build the IAR metasurface unit cell considering a portion of the elastic domain with the depth $H = 3\lambda_{\omega_r, I(1, \theta)}$ and width $a \ll \lambda_{\omega_r, I(1, \theta)}$, as shown in Fig.2.6a. The elastic half-space is modeled under plane-strain assumptions. Periodic boundary conditions are imposed on the lateral edges of the unit cell to obtain the numerical dispersion relation of Rayleigh waves propagating in the principle wavenumber direction k_x (e.g., along the x -axis) of the half-space. The bottom edge of the model is restrained to prevent any undesired rigid motions.

The inertial amplified resonator comprises four rigid truss elements of length L connecting the three masses and a vertical spring element linking the top mass to the unit cell's base. The top $m_{T, 2D}$ and lateral $m_{L, 2D}$ embedded masses are modeled as added point masses at the truss elements' tips. The total inertia of the IAR in the 2D model is set as $m_{2D} = m_{T, 2D} + 2m_{L, 2D} = m \cdot a/S$, to achieve a linear distribution of resonator mass equivalent to the one assumed in our analytical model. The lateral displacement of the top mass is restrained, again in accordance with the developed analytical model in Sec.2.2.

The unit cell domain is discretized with quadratic triangular elements with a minimum dimension of $d_{min} = a/2$ to provide an adequate approximation of the shortest wavelength at the highest frequency of interest. Henceforth, an extra thin homogeneous layer of thickness $t_l < a \ll \lambda_{\omega_r, I(1, \theta)}$, with a larger stiffness with respect to the elastic half-space, i.e., $c_{L, lay} = 2c_L$, $c_{T, lay} = 2c_T$, is placed between the IAR and half-space. The existence of the thin stiff layer avoids stress concentrations at the IAR-substrate connection ensuring the uniform stress distribution assumption of the analytical effective medium approach.

Dispersion curves, as extracted from the numerical model with $a = \lambda_{\omega_r, I(1, \theta)}/124$ and $t_l = a/6$ are shown in Fig. 2.6b for three different internal angles $\theta = [20^\circ, 30^\circ, 40^\circ]$ and a constant mass distribution ratio $\alpha = 0.5$. The FE eigensolutions, marked by solid circles well-matched the analytical predictions reported with continuous lines.

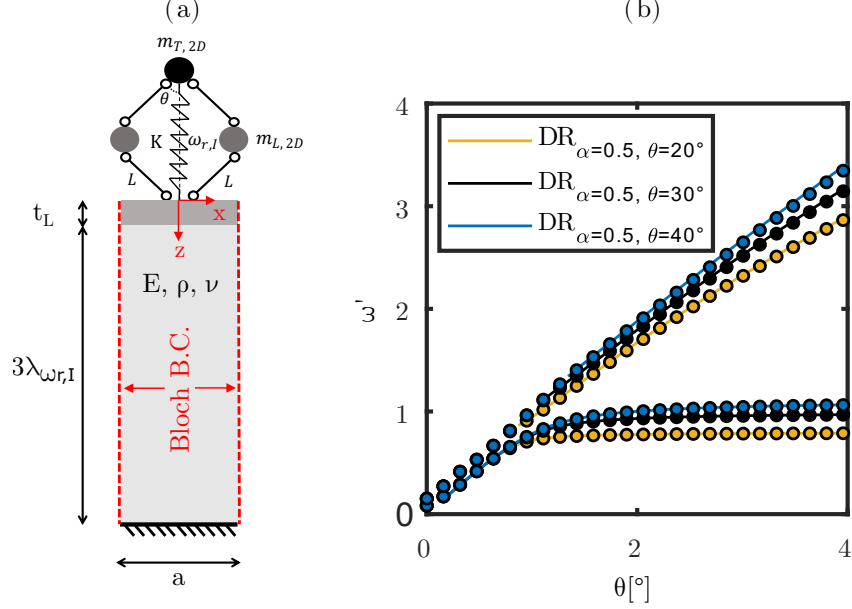


Figure 2.6: (a) Schematic of the 2D IAR metasurface unit cell. (b) Dispersion curves as extracted from the Finite Element (FE) model (dots) and analytical dispersion law (continuous lines) for varying internal angles $\theta = [20^\circ, 30^\circ, 40^\circ]$. Panel (b) is reproduced with permission [160], Copyright 2019, Springer Nature.

2.4 Transmission of a finite-length IAR metasurface

In this section, we employ the metasurface unit cell model (Fig.2.6a) as the building block of an extended numerical model to investigate the transmission coefficient of a finite-length IAR metasurface, i.e., $L_M = 3\lambda_{\omega_r, I(1, \theta)}$ (see Fig. 2.7a). The metasurface layer is inserted within two half-space domains: (I) an input domain of length $L_{inp} = 10\lambda_{\omega_r, I(1, \theta)}$, where a harmonic surface point source is placed at a distance $d_s = 2\lambda_{\omega_r, I(1, \theta)}$ from the model edge; (II) an output domain of length $L_{out} = 4\lambda_{\omega_r, I(1, \theta)}$. The harmonic point source excites the input domain with vertical unitary displacement. Horizontal and vertical rigid motions of the numerical model are restrained by the two fixed hinges placed at the model bottom corners. Then,

Low-reflective boundary conditions (LRBs) are applied at the lateral edges of the model to minimize the wave reflections effect from the boundaries. LRBC uses the material properties of the adjacent media to create an impedance-matched interface for the propagating longitudinal and shear waves [162]. The whole domain is discretized using triangular elements with a minimum dimension of $d_{min} = a/2$ and a maximum dimension equals $1/20$ of the reference Rayleigh wavelength ($\lambda_{\omega_r, I(1, \theta)}$).

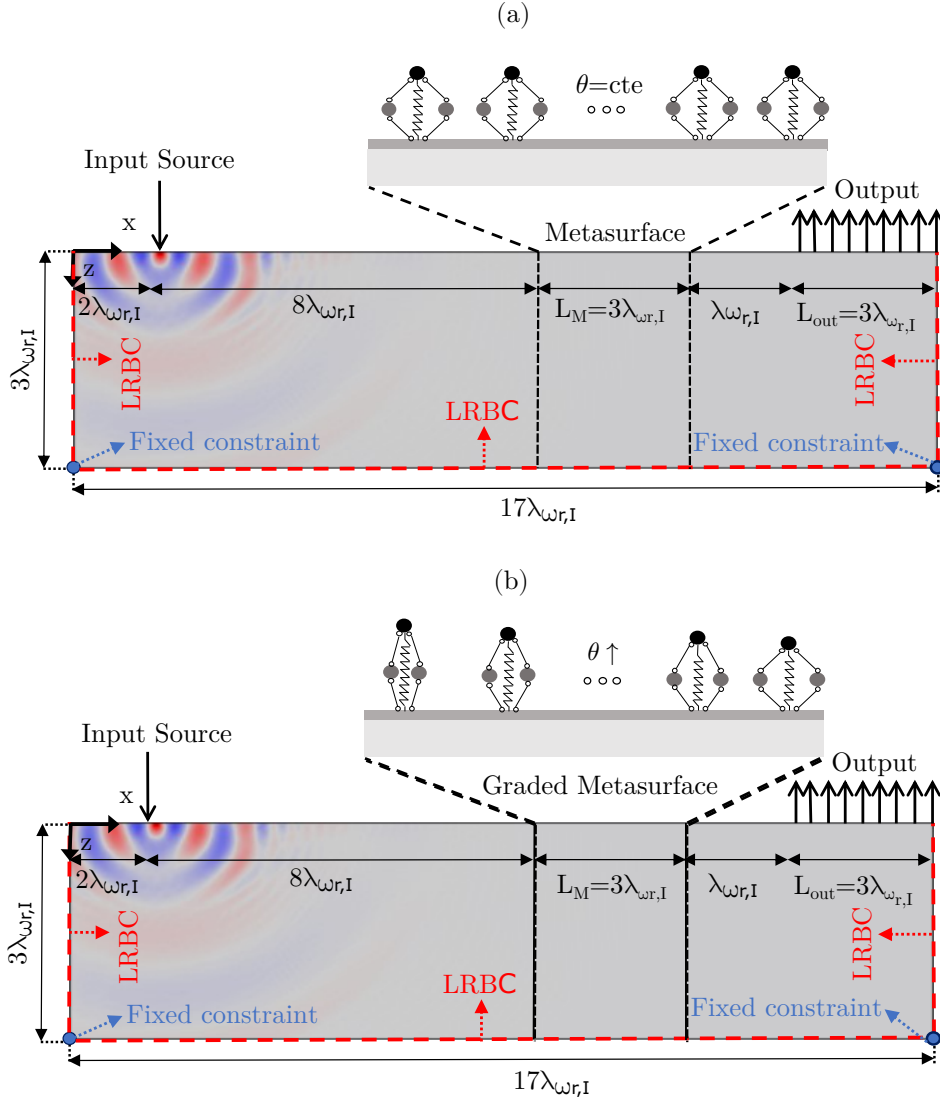


Figure 2.7: (a) Schematics of a finite-length single-frequency resonant metasurface. (b) Schematics of the graded IAR metasurface of increasing internal angle $\theta = [10^\circ - 50^\circ]$ and constant mass distribution $\alpha = 0.5$.

Harmonic analyses within the normalized angular frequency range $\omega' = [0 - 4]$ are performed for an IAR metasurface with design parameters set as $\alpha = 0.5$ and $\theta = 30^\circ$. The vertical displacement fields for Rayleigh waves propagating at the FE model are shown in Fig. 2.8a and b, for excitation frequencies $\omega' = \omega'_{r,I}$ and $\omega' = \omega'_{f0}$, respectively. The contour plot confirms the conversion of the incident Rayleigh wave into bulk shear waves at the resonant frequency of IAR metasurface (see Fig. 2.8a). Conversely, Fig. 2.8b highlights the zero-force frequency $\omega' = \omega'_{f0}$ behavior in which the metasurface becomes transparent to the propagation of incoming Rayleigh waves.

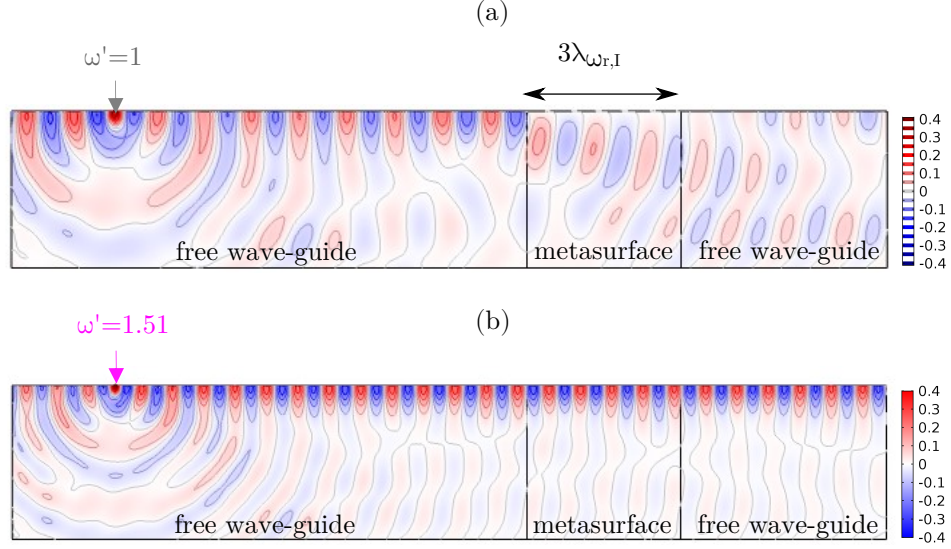


Figure 2.8: (a) The vertical displacement field for a vertical harmonic excitation at the resonant frequency of the advanced metasurfaces. (b) The vertical displacement field of the z-axis is driven by a harmonic excitation at the zero-force frequency.

We perform extended frequency domain analyses in the same normalized frequency range ($\omega' = [0 - 4]$) for different IAR configurations by keeping the mass ratio constant ($\alpha = 0.5$) and altering the internal angle within the range $\theta = [20^\circ, 30^\circ, 40^\circ]$ to compare the transmission efficiency of the different IAR metasurface configurations. The transmission coefficient is calculated as:

$$T(\omega') = \frac{\int_0^{3\lambda_{\omega_{r,I}(1,\theta)}} |\bar{v}_{z,m}| dx}{\int_0^{3\lambda_{\omega_{r,I}(1,\theta)}} |\bar{v}_{z,f}| dx} \quad (2.22)$$

where $\bar{v}_{z,m}$ is the averaged nodal vertical displacement as calculated from the numerical simulations along the output domain for a length $3\lambda_{\omega_{r,I}(1,\theta)}$. Likewise, $\bar{v}_{z,f}$ is the averaged nodal vertical displacement of the “free” wave field extracted

from a reference numerical model in the absence of the metasurface layer. As expected, in the relevant bandgap frequency zone, the amplitude of the input signal is significantly decreased, for all different configurations of IAR metasurface, which achieve comparable values of peak attenuation. We note that the possibility of tuning the bandgap frequency range comes at the expense of its frequency width, as already observed from the metasurface dispersion curves (see Fig.2.5e) [160]. Moreover, in the high-frequency range, the transmission coefficient presents a marked decreasing trend, almost linear in frequency, which depends on the internal angle of the IAR. This behavior stems from the dead mass dynamics of the IAR metasurface which presents an increasing impedance mismatch with the Rayleigh waves in the homogeneous medium.

Eventually, we leverage the tunable dispersive feature of the advanced metasurface to design a graded metasurface exploiting the concept of rainbow trapping [100] (see Chapter.1 Fig.1.8), i.e., a frequency-varying metasurface of resonators with increasing natural frequencies along its length. Consequently, by keeping constant the IAR inertia ratio (i.e. $\alpha = 0.5$) and increasing the internal angle of the resonator along the metasurface length from $\theta = 10^\circ$ to $\theta = 50^\circ$, we can realize a metasurface with a constant static response and variable dynamic response. The schematic of the graded metasurface is presented in Fig. 2.7b, where the normalized IAR resonance frequency is increased linearly within the normalized angular frequency range $\omega'_{r,I}(\alpha, \theta) = [0.5 - 1.2]$ along the metasurface array. The variation of the internal angle over the metasurface length is obtained by rearranging Eq. (2.6) as below:

$$\theta(\omega', \alpha) = \arctan \sqrt{\frac{1 - \alpha}{(\frac{2}{\omega'})^2 - 3\alpha - 1}} \quad (2.23)$$

The transmission curve of the graded metasurface is shown in Fig. 2.9b. The multiple-frequency metasurface recovers the bandgap frequencies of the different IAR configurations. Additionally, its high-frequency behavior is governed by the response of the IAR metasurface with a low internal angle, which indeed presents the highest impedance mismatch.

2.5 Conclusions

We designed an advanced tunable metasurface exploiting the concept of inertial amplification mechanism (IAM) capable to interact and impede the propagation of vertically polarized surface waves. Inertial Amplified Resonator (IAR) as the building block of the advanced tunable metasurface is realized by two lateral inerters, i.e., kinematical devices made by two inclined rigid links connected to an

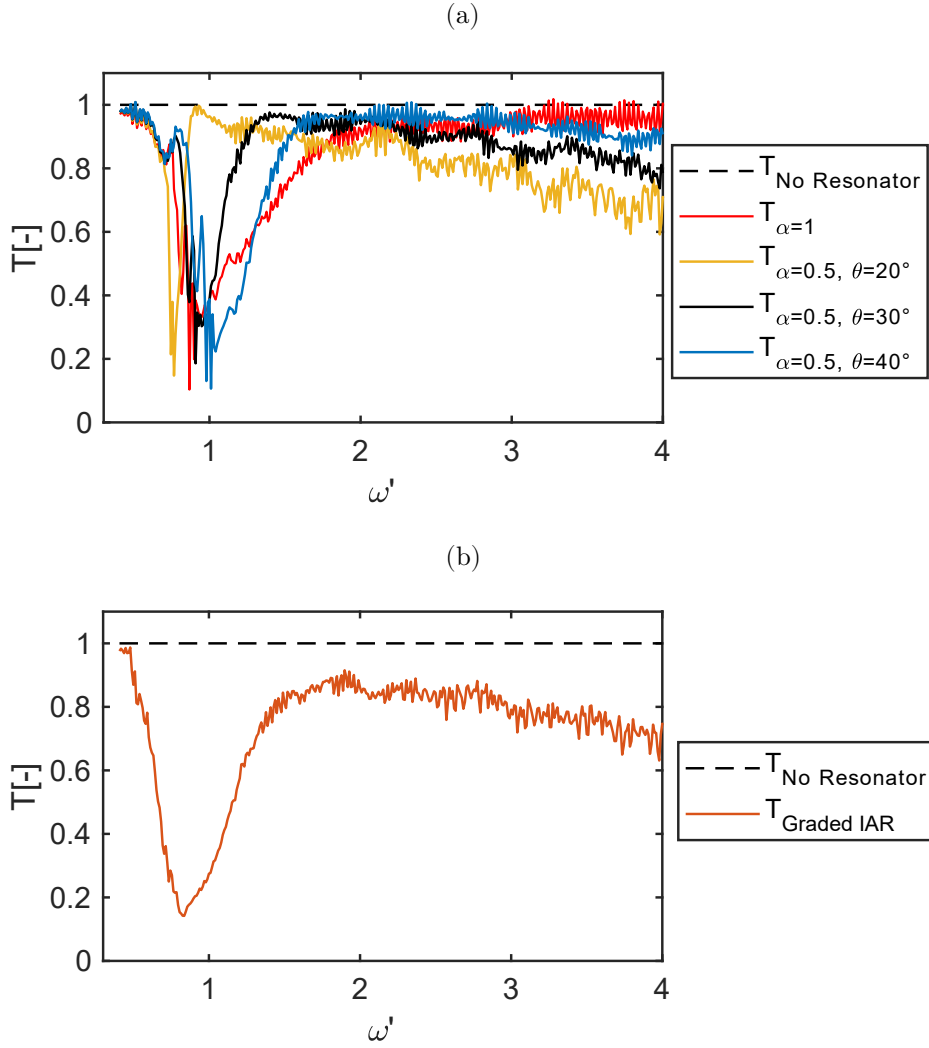


Figure 2.9: (a) Transmission coefficient of different IAR metasurfaces. (b) Transmission coefficient for the graded metasurface of IARs. Figures are reproduced with permission [160], Copyright 2019, Springer Nature.

additional mass to modify the total inertia of the resonator. The natural frequency of the IAR is controlled by two design parameters, namely the internal angle (θ) and the mass distribution ratio (α).

We followed the effective medium approach [99] to derive an original dispersion relation for a locally resonant metasurface made of a periodic arrangement of IARs at the free waveguide surface of an elastic half-space. We have shown that the interaction between Rayleigh waves and locally resonant IAR metasurfaces generates a low-frequency bandgap analogous to that of a classical mass-spring

metasurface. On the contrary, IAR metasurface presents a tunable dynamic response with a prescribed static response and allows the possibility of opening large spectral bandgaps with a small amount of effective mass. Besides, IAR metasurface demonstrated a high-frequency filtering behavior analogous to an array of "dead masses" placed directly over an elastic substrate. We took advantage of the modular and tunable design of the IAR metasurface to design graded metasurface (or varying-frequency metasurface) of increasing resonant frequency for broadband Rayleigh waves attenuation.

A resonant seismic wave barrier can be realized according to the proposed advance metasurface by assuming a shear velocity $c_T = 120 \text{ m/s}$, a longitudinal wave velocity $c_L = 230 \text{ m/s}$, a density of $\rho = 1300 \text{ kg/m}^3$ for the soil; a resonant frequency $f_r = 4.9 \text{ Hz}$ and an overall mass of $m = 3000 \text{ kg}$ for the resonator [88]. In this case, a tunable resonator could be practically conceived utilizing rigid telescopic links with a variable length such that for a given elongating elastic bearing of length L_s different IAR configurations (i.e., different IAR angles) can be achieved by simply altering the length of the rigid telescopic links (see the schematic in Fig. 2.10).

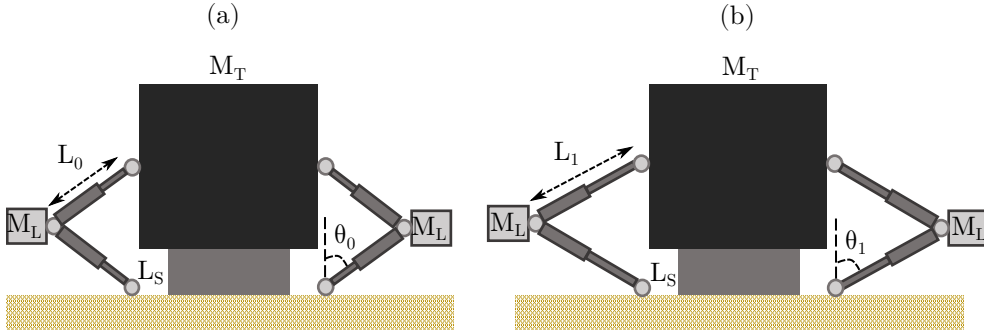


Figure 2.10: Schematic of a possible design for a tunable IAR for seismic Rayleigh waves in (a) undeformed and (b) deformed configurations. Reproduced with permission [160], Copyright 2019, Springer Nature.

For wide-band low-frequency random seismic excitation, an IAR metasurface with the maximum inclination angle $\theta = 80^\circ$ and $0.5 < \alpha < 1$ (see Fig. 2.5e) should be considered to open a considerable large low-frequency bandgap.

In summary, the proposed IAR metasurface is able to tune the dynamic response of the locally resonant metasurfaces. The IAR metasurface can have multiple applications in the context of surface waves manipulation, from SAW devices to seismic isolation systems.

2.6 Acknowledgments

The author would like to remark that the contents and figures of this chapter are partially adopted and reproduced from Ref. [160] with permission obtained on date Nov 30, 2020, under license number 4958690164313, Copyright 2019, Springer Nature.

Chapter 3

Rayleigh waves in resonant bulk metamaterials

Abstract

In this chapter, we go beyond the assumption of considering the locally resonant metasurfaces as a thin resonant interface placed at the free surface of an elastic waveguide by investigating the dynamics of Rayleigh waves propagation in thick resonant layers made of regularly distributed resonant materials along with the depth of the waveguide. In particular, we derive an analytical dispersion law for the case of a resonant layer with a variable thickness coupled to a non-resonant elastic half-space. The interaction of sub-wavelength embedded resonators and Rayleigh waves generates a low-frequency bandgap in the frequency span where the effective mass density of the resonant metamaterial assumes negative values. Around the bandgap frequency, we observe the existence of a leaky surface mode which disperses part of elastic wave energy into the half-space and contributes to the Rayleigh wave attenuation mechanism. Then, we perform parametric studies to unveil the dependence of bandgap width on the thickness of the resonant layer. Furthermore, we demonstrate that our analytical framework can capture the fundamental dynamics of a resonant metasurface, conceived as a thin resonant layer, as well as a full resonant half-space.

We take advantage of the dispersive features of the resonant layer to propose a seismic wave barrier realized by meter-size mechanical oscillators embedded inside the soil. Numerical models are developed according to the WFEM approach and Bloch's theorem to validate the dispersion laws. Eventually, to verify the theoretical findings of the work, the design procedure of a table-top experimental campaign is described. This procedure includes the design of a resonant metamaterial plate with the thin and thick resonant layers analogous to the presented analytical framework.

3.1 Introduction

Resonant metamaterials are artificial composites with local resonant particles or structures of sub-wavelength dimensions hosted in an elastic medium [163]. In a medium containing sub-wavelength resonators, surface waves hybridize with the local resonances and generate bulk waves bandgaps stems from the avoided crossing behavior of fundamental surface mode [153]. The bandgaps arise in the narrow frequency range between the resonance and anti-resonance of the resonators, where the density of the effective homogeneous medium assumes negative values.

Resonant metamaterials were initially realized to impede the propagation of bulk waves inside the local resonance-induced bandgaps [16]. For example, a bulk metamaterial realized by an arrangement of solid inclusions coated with a layer of soft material and embedded in an elastic matrix (hard-soft-hard metamaterial) has shown the generation of low-frequency bandgaps around the inclusions resonant frequencies [29, 28, 31]. These bandgaps were found to be related to the “effective” negative mass density of the material. The same physical phenomenon has been observed later in discrete mass-in-mass spring systems [45, 46], in trusses and beams equipped with internal resonators [34, 35], and 2D resonant metamaterials [36, 37, 38].

Complementary to the resonant inclusions embedded in a hosting material, resonant structures arranged at the top of an elastic medium, also known as locally resonant metasurfaces, have been proposed to control the propagation of surface Rayleigh waves. Surface-to-shear wave conversion [88, 97], filtering [164, 98, 100], and waveguiding [99, 8, 104] are among the notable applications of locally resonant metasurfaces. These peculiar dynamic effects were predicted by exploiting ad-hoc dispersion laws formulated by considering the metasurfaces as a dynamic resonant boundary condition for the elastic waveguides [99]. Despite the numerous applications of the resonant metasurfaces, the scenarios where resonators are distributed through the bulk medium or within a thick surface layer overlying a homogeneous half-space are still unexplored. Understanding the dynamics of these systems is essential to ease the development of novel devices and strategies to control and mitigate the propagation of surface waves, like metabarriers [88, 101] and metafoundations [87, 82] recently conceived for ground vibrations and seismic waves.

Henceforth, in this chapter, we study and investigate the dynamics of Rayleigh-type surface waves propagating through a medium composed of a finite-thickness resonant layer overlaid a homogeneous non-resonant half-space. The resonant layer is considered to have isotropic homogeneous material property made of the randomly distributed resonators, discrete mass-in-mass composite [46], attached to the host media via elastic connectors. Such an appropriate physical model is able to predict the effective medium dynamic properties, namely effective mass density

in the long-wavelength range. Then, we employ a static homogenization approach to derive the effective bulk velocities. We use this description to derive an original dispersion law to predict the dispersive features of the resonant bulk metamaterial, particularly the existence and extension of bandgaps for Rayleigh waves.

We continue our investigation by considering a case study of seismic waves propagation through a deep barrier made of buried resonators inside the soil, to validate our proposed analytical framework. Hence, we first consider the limit case of a very thick resonant layer with a depth much larger than the wavelength of interest, namely a resonant half-space. Next, we investigate the resonant layer with variable thicknesses placed over the non-resonant half-space and discuss the variation in dispersion properties and bandgaps width with respect to the resonant layer thickness. We develop numerical models according to WFEM [165] and Bloch wave [18], to verify our analytical findings including the validity of the applied homogenization approach and derived dispersion laws. The attenuation performance of the proposed seismic barrier is investigated through full 2D FE simulations.

The chapter is organized as follows. First, we derive the dispersion relation of a finite-thickness resonant layer overlaying a homogeneous half-space in Sec. 3.2. Next, we investigate the dispersive properties of the proposed resonant seismic barrier as the case study in Sec. 3.3. The analytical results are confronted and validated against finite element simulations where the exact geometry of the resonant barrier is employed. In Sec. 3.4, harmonic analyses are performed to calculate the transmission coefficients of different resonant layer configurations and to compare their attenuation performances. Besides, it is shown how the proposed analytical model recovers the dynamic behavior of a resonant metasurface. In Sec. 3.5, we describe the design guidelines of a resonant metamaterial plate composed of resonant layers with different thicknesses. The resonant metamaterial plate mimics the partially resonant waveguide whose dynamic properties have been studied analytically and numerically in this chapter. The rationally designed plate is set to test and verify the main findings of this study experimentally. Finally, some conclusions are drawn in Sec. 3.6.

3.2 Dispersion law for Rayleigh waves propagating in a resonant layer coupled with a homogeneous non-resonant half-space

In what follows, we derive the dispersive properties of Rayleigh-type surface waves in a resonant layer of finite thickness H coupled to a homogeneous, isotropic, and elastic non-resonant half-space. Without loss of generality, we restrict our interest

to the waves propagating in the $x - z$ domain assuming plane-strain conditions.

3.2.1 Resonant layer and effective medium description

The resonant layer is composed of local resonators randomly distributed in the host medium (see Fig. 3.1). Each resonator consists of a rigid mass (m_r) suspended by horizontal and vertical springs with identical axial stiffness K . This yields to the existence of degenerate resonant modes with an angular frequency $\omega_{r,x} = \omega_{r,z} = \omega_r$ along the axis $x - z$. The local resonators have dimensions significantly smaller than the wavelength of the propagating surface waves (λ) in the low-frequency range of interest. Additionally, we assume the host material to be isotropic and homogeneous with Lamé parameters λ_h and μ_h and density ρ_h .

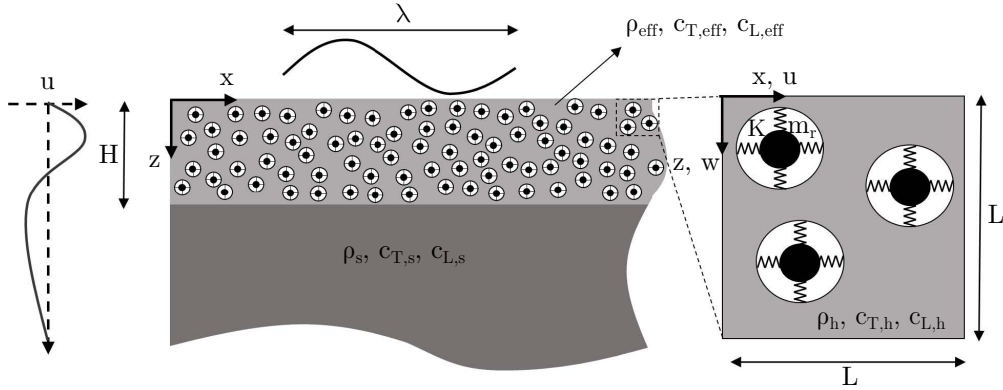


Figure 3.1: Schematic of a resonant layer made of randomly distributed resonators overlying a non-resonant homogeneous semi-infinite medium. The inset shows a detail of the reference volume element (RVE).

Under these assumptions, the dynamics of such resonant metamaterial can be appropriately described utilizing an “effective” medium approach. The effective description aims at defining the properties of an equivalent homogeneous material with frequency-dependent mass density and bulk waves velocities able to approximate the dynamic response of the composite medium in the long-wavelength regime. Our purpose is to derive effective density and bulk waves speeds expressions for the resonant material and use them to obtain an analytical formulation of the dispersion laws for surface waves existing in the layered resonant medium. The analytical formulation should provide an accurate description of the low-frequency dynamics of the layered resonant medium.

We consider an ensemble of n discrete resonators embedded in the host material within a reference volume $V = St$, where $S = L^2$ is the surface area of the 2D plane-strain model (see inset in Fig. 3.1), and t is the unitary out-of-plane thickness,

to properly define the effective density. For this configuration, the effective density can be adequately represented by a scalar frequency-dependent function [166]:

$$\rho_{eff}(\omega) = \frac{m_h + nm_r}{V} + \frac{nm_r}{V} \frac{\omega^2}{\omega_r^2 - \omega^2} = \rho_0 \left(1 + \alpha \frac{\omega^2}{\omega_r^2 - \omega^2} \right) \quad (3.1)$$

where ω is the angular frequency, m_h is the mass of host material enclosed in the reference volume, $\rho_0 = (m_h + nm_r)/V$ is the static ($\omega = 0$) density, and $\alpha = nm_r/(V\rho_0)$ is the ratio between the resonator mass per unit volume and the static density.

Given our interest in the low-frequency response of the resonant metamaterial, we resort to a static homogenization of its elastic parameters. Hence, for the definition of the effective elastic response of the composite material, here assumed to be isotropic at the length scale of interest, we need to compute two effective elastic parameters. For example, the reference volume material (or reference area in a 2D plane-strain model) can be subjected to a constrained uniaxial strain state (Fig. 3.2a) and to a shear strain state (Fig. 3.2b) to estimate the effective longitudinal modulus $M_{eff} = \lambda_{eff} + 2\mu_{eff}$ and the effective shear modulus μ_{eff} , respectively. If so, the two elastic parameters are calculated as:

$$M_{eff} = \frac{\bar{\sigma}_{xx}}{\bar{\varepsilon}_{xx}}, \quad \mu_{eff} = \frac{\bar{\sigma}_{xz}}{\bar{\gamma}_{xz}}, \quad (3.2)$$

where:

$$\bar{\sigma}_{xx} = \frac{\int_S \sigma_{xx} dS}{S}, \quad \bar{\varepsilon}_{xx} = \frac{\int_S \varepsilon_{xx} dS}{S}, \quad \bar{\sigma}_{xz} = \frac{\int_L \sigma_{xz} dL t}{L t}, \quad \bar{\gamma}_{xz} = \frac{\Delta u}{L} \quad (3.3)$$

In Eq. (3.3), $\bar{\sigma}_{xx}$ and $\bar{\varepsilon}_{xx}$ are respectively the average stress and average strain components associated with the uniaxial constrained deformation state calculated within the host medium enclosed in the reference area S . Similarly, $\bar{\sigma}_{xz}$ and $\bar{\gamma}_{xz}$ are respectively the average shear stress calculated along the top surface of the reference volume element and the related average shear strain.

At this stage, the effective bulk velocities of the homogenized composite can be obtained as:

$$c_{L,eff}(\omega) = \sqrt{\frac{\lambda_{eff} + 2\mu_{eff}}{\rho_{eff}(\omega)}} \quad (3.4)$$

$$c_{T,eff}(\omega) = \sqrt{\frac{\mu_{eff}}{\rho_{eff}(\omega)}} \quad (3.5)$$

These velocities are utilized in the analytical framework developed in the next section to describe the dispersive properties of surface waves in resonant materials.

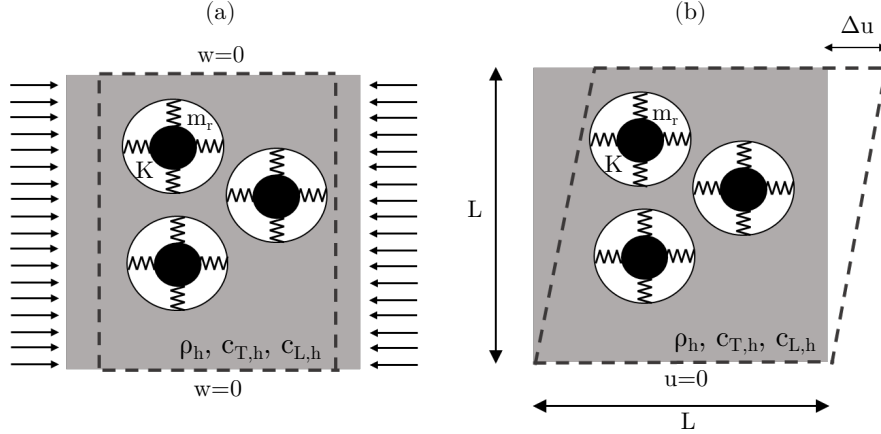


Figure 3.2: Schematics of the reference volumes used for the calculation of the (a) effective longitudinal modulus M_{eff} and (b) effective shear modulus μ_{eff} .

3.2.2 Longitudinal and shear wave velocities in the anisotropic 2D continuum

In long-wavelength approximation, the dynamics of the resonant layer can be discussed as an anisotropic 2D crystal, which is equivalent to those of cubic crystals. We discuss such a consideration together with the effect of wave polarization on the extraction of longitudinal and shear waves in this section. According to the classical theory of elastodynamics, the equations of motion for the cubic crystal read:

$$\nabla \cdot \mathbf{C} : \nabla_s \mathbf{u} = \rho_{eff} \ddot{\mathbf{u}} \quad (3.6)$$

where \mathbf{C} is the tensor of elastic coefficients and \mathbf{u} is the displacement vector. For an arbitrary plane harmonic wave with the propagation direction defined by wavenumber components k_x and k_z in $x - z$ plane of the resonant layer, the wave motions assume the solutions in the form of:

$$u_j = A p_j \exp[i(k_x x + k_z z - \omega t)] \quad (j = x, z) \quad (3.7)$$

where A is the wave amplitude, p_j is the wave polarization, and (k_x, k_z) is the direction of the propagating wave. By substituting the wave solution in Eq. (3.7) into Eq. (3.6), Christoffel's equation for a 2D crystal is obtained as:

$$\begin{bmatrix} \lambda_{xx} - \rho_{eff} c^2 & \lambda_{xz} \\ \lambda_{xz} & \lambda_{zz} - \rho_{eff} c^2 \end{bmatrix} \begin{bmatrix} p_x \\ p_z \end{bmatrix} = \begin{bmatrix} 0 \\ 0 \end{bmatrix} \quad (3.8)$$

where $c = \omega/k$ is the velocity of the propagating wave.

$$\begin{aligned}
\lambda_{xx} &= l^2 C_{11} + m^2 C_{44} \\
\lambda_{zz} &= m^2 C_{11} + l^2 C_{44} \\
\lambda_{xz} &= ml(C_{12} + C_{44})
\end{aligned} \tag{3.9}$$

where $m = \sin \theta$ and $l = \cos \theta$. For the wave propagation along x -axis, Eq. (3.8) becomes:

$$\begin{bmatrix} C_{11} - \rho_{eff} c^2 & 0 \\ 0 & C_{44} - \rho_{eff} c^2 \end{bmatrix} \begin{bmatrix} p_x \\ p_z \end{bmatrix} = \begin{bmatrix} 0 \\ 0 \end{bmatrix} \tag{3.10}$$

From Eq. (3.10), the longitudinal and shear wave speeds are obtained as:

$$c_{L,eff}(\omega) = \sqrt{\frac{C_{11}}{\rho_{eff}(\omega)}} \tag{3.11}$$

$$c_{T,eff}(\omega) = \sqrt{\frac{C_{44}}{\rho_{eff}(\omega)}} \tag{3.12}$$

where C_{11} and C_{44} are the elastic parameters of the resonant layer. For an isotropic material $C_{11} = \lambda + 2\mu$ and $C_{44} = \mu$.

For the plane harmonic wave propagating at an angle of $\theta = 45$ with respect to the principal directions, $m = l = \sqrt{2}/2$, Eq. (3.8) can be updated as:

$$\begin{bmatrix} \frac{(C_{11}+C_{44})}{2} - \rho_{eff} c^2 & \frac{(C_{12}+C_{44})}{2} \\ \frac{(C_{12}+C_{44})}{2} & \frac{(C_{11}+C_{44})}{2} - \rho_{eff} c^2 \end{bmatrix} \begin{bmatrix} p_x \\ p_z \end{bmatrix} = \begin{bmatrix} 0 \\ 0 \end{bmatrix} \tag{3.13}$$

The eigenvalues of the Eq. (3.13) return the wave speeds:

$$\begin{aligned}
c_1(\omega) &= \sqrt{\frac{C_{11} + C_{12} + C_{44}}{2\rho_{eff}(\omega)}} \\
c_2(\omega) &= \sqrt{\frac{C_{11} - C_{12}}{2\rho_{eff}(\omega)}}
\end{aligned} \tag{3.14}$$

The pure longitudinal wave ($p_1 = p_2 = \sqrt{2}/2$) exists for $c = c_1(\omega)$. Pure shear wave exists in $(x - \bar{z})$ plane when $p_1 = -p_2$.

3.2.3 Derivation of the dispersion relation

We now analyze the propagation of vertically polarized (Rayleigh-like) surface waves in a semi-infinite domain ($x - z$ plane, for $z > 0$), composed of a resonant layer of depth H overlying an elastic isotropic non-resonant half-space (see Fig. 3.1). The dynamics of the resonant layer is described by exploiting its frequency-dependent effective properties, namely ρ_{eff} , $c_{L,eff}$ and $c_{T,eff}$, as derived in Sec. 3.2.1, whereas the isotropic, homogeneous half-space is characterized by mass density ρ_s and longitudinal and shear waves speed $c_{L,s}$, and $c_{T,s}$, respectively. In what follows, parameters with subscript 1 denote the resonant layer and 2 elastic half-space, respectively.

We consider a plane harmonic wave propagating along the x -axis with a wavenumber k and angular frequency ω . For a wave polarized in the $x - z$ plane, the displacement vectors in the resonant layer \mathbf{u}_1 and the half-space \mathbf{u}_2 read:

$$\mathbf{u}_j = [u_j, v_j, w_j] \quad j = 1, 2 \quad (3.15)$$

where $v_1 = v_2 = 0$ are null displacement components. The displacement fields can be expressed in terms of the potential functions Φ_j , and $\Psi_{y,j}$:

$$u_j = \frac{\partial \Phi_j}{\partial x} - \frac{\partial \Psi_{y,j}}{\partial z}, \quad w_j = \frac{\partial \Phi_j}{\partial z} + \frac{\partial \Psi_{y,j}}{\partial x} \quad j = 1, 2 \quad (3.16)$$

where Φ_j is the scalar dilatation potential while $\Psi_{y,j}$ is the y -component of the distortional vector potential Ψ . These potentials should satisfy the wave equations in both the resonant layer and the half-space:

$$\begin{aligned} \nabla^2 \Phi_1 &= \frac{1}{(c_{L,eff})^2} \frac{\partial^2 \Phi_1}{\partial t^2}, & \nabla^2 \Psi_{y,1} &= \frac{1}{(c_{T,eff})^2} \frac{\partial^2 \Psi_{y,1}}{\partial t^2}, \\ \nabla^2 \Phi_2 &= \frac{1}{(c_{L,s})^2} \frac{\partial^2 \Phi_2}{\partial t^2}, & \nabla^2 \Psi_{y,2} &= \frac{1}{(c_{T,s})^2} \frac{\partial^2 \Psi_{y,2}}{\partial t^2}. \end{aligned} \quad (3.17)$$

Solutions of Eqs. (3.17) can be provided in the form:

$$\begin{aligned} \Phi_1(x, z, t) &= (a_1^d e^{ikr_1 z} + a_1^u e^{-ikr_1 z}) e^{i(\omega t - kx)}, \\ \Psi_{y,1}(x, z, t) &= (b_1^d e^{iks_1 z} + b_1^u e^{-iks_1 z}) e^{i(\omega t - kx)}, \\ \Phi_2(x, z, t) &= (a_2^d e^{ikr_2(z-H)} + a_2^u e^{-ikr_2(z-H)}) e^{i(\omega t - kx)}, \\ \Psi_{y,2}(x, z, t) &= (b_2^d e^{iks_2(z-H)} + b_2^u e^{-iks_2(z-H)}) e^{i(\omega t - kx)}. \end{aligned} \quad (3.18)$$

where r_j and s_j , for $j = 1, 2$, are given by:

$$\begin{aligned} r_1 &= \sqrt{\left(\frac{\omega}{kc_{L,eff}}\right)^2 - 1}, & s_1 &= \sqrt{\left(\frac{\omega}{kc_{T,eff}}\right)^2 - 1}, \\ r_2 &= \sqrt{\left(\frac{\omega}{kc_{L,s}}\right)^2 - 1}, & s_2 &= \sqrt{\left(\frac{\omega}{kc_{T,s}}\right)^2 - 1}. \end{aligned} \quad (3.19)$$

and where a_j^d , b_j^d , a_j^u , and b_j^u , for $j = 1, 2$, denote the amplitudes of the downgoing (superscript d) and upgoing (superscript u) body waves, respectively. We restrict our interest to the derivation of surface wave solutions by assuming inhomogeneous potentials within the elastic half-space as:

$$\begin{aligned} \Phi_2(x, z, t) &= a_2^d e^{-kr_2^*(z-H)+i(\omega t-kx)} \\ \Psi_{y,2}(x, z, t) &= b_2^d e^{-ks_2^*(z-H)+i(\omega t-kx)} \end{aligned} \quad (3.20)$$

where:

$$r_2 = ir_2^*, \quad r_2^* = \sqrt{1 - \left(\frac{\omega}{kc_{L,s}}\right)^2}, \quad s_2 = is_2^*, \quad s_2^* = \sqrt{1 - \left(\frac{\omega}{kc_{T,s}}\right)^2}, \quad (3.21)$$

and considering waves with phase velocity $c = \frac{\omega}{k} < c_{T,s} < c_{L,s}$. We highlight that the exponentially increasing waves do not propagate in the half-space and they have been eliminated by imposing $a_2^u = 0$, and $b_2^u = 0$. After some simple algebraic manipulations, the potential functions in both the resonant and homogeneous half-space are reformulated as:

$$\begin{aligned} \Phi_1(x, z, t) &= \left(A_1 \cos(kr_1 z) + A_2 \sin(kr_1 z) \right) e^{i(\omega t-kx)} \\ \Phi_2(x, z, t) &= A_3 e^{-kr_2^*(z-H)+i(\omega t-kx)} \\ \Psi_{y,1}(x, z, t) &= \left(A_4 \cos(ks_1 z) + A_5 \sin(ks_1 z) \right) e^{i(\omega t-kx)} \\ \Psi_{y,2}(x, z, t) &= A_6 e^{-ks_2^*(z-H)+i(\omega t-kx)} \end{aligned} \quad (3.22)$$

where A_j , for $j = 1, \dots, 6$, are constants that can be derived from a_j^u , a_j^d , b_j^u , b_j^d (e.g., $A_1 = a_1^d + a_1^u$). Substituting Eq. (3.22) into Eq. (3.16), and dropping the common propagating term $e^{i(\omega t-kx)}$, the horizontal and vertical displacement functions in

the resonant layer can be derived as:

$$\begin{aligned} u_1 &= -k \left[i \left(A_1 \cos(kr_1 z) + A_2 \sin(kr_1 z) \right) + s_1 \left(-A_4 \sin(ks_1 z) + A_5 \cos(ks_1 z) \right) \right] \\ w_1 &= -k \left[r_1 \left(A_1 \sin(kr_1 z) - A_2 \cos(kr_1 z) \right) + i \left(A_4 \cos(ks_1 z) + A_5 \sin(ks_1 z) \right) \right] \end{aligned} \quad (3.23)$$

Similarly, the displacements in the half-space are obtained as:

$$\begin{aligned} u_2 &= -k \left(iA_3 e^{-kr_2^*(z-H)} - s_2^* A_6 e^{-ks_2^*(z-H)} \right) \\ w_2 &= -k \left(r_2^* A_3 e^{-kr_2^*(z-H)} + iA_6 e^{-ks_2^*(z-H)} \right) \end{aligned} \quad (3.24)$$

By exploiting linear elastic isotropic constitutive relations, the stress components within the layers are expressed as:

$$\sigma_{zx,j} = \mu_j \left(\frac{\partial w_j}{\partial x} + \frac{\partial u_j}{\partial z} \right), \quad \sigma_{zz,j} = \lambda_j \operatorname{div} \mathbf{u}_j + 2\mu_j \frac{\partial w_j}{\partial z}. \quad j = 1, 2. \quad (3.25)$$

We substitute the displacements of the layered systems, Eq. (3.23) and Eq. (3.24), into Eq. (3.25), to obtain the tangential and normal stresses in the resonant layer:

$$\begin{aligned} \sigma_{zx,1} &= \rho_{eff} \omega^2 \left[i r_1 \gamma_1 (A_1 \sin(kr_1 z) - A_2 \cos(kr_1 z)) - \delta_1 (A_4 \cos(ks_1 z) + A_5 \sin(ks_1 z)) \right] \\ \sigma_{zz,1} &= \rho_{eff} \omega^2 \left[\delta_1 (A_1 \cos(kr_1 z) + A_2 \sin(kr_1 z)) + i \gamma_1 s_1 (A_4 \sin(ks_1 z) - A_5 \cos(ks_1 z)) \right] \end{aligned} \quad (3.26)$$

where, $\gamma_1 = 2(kc_{T,eff}/\omega)^2$ and $\delta_1 = \gamma_1 - 1$. Similarly, the stress components in the half-space are derived as:

$$\begin{aligned} \sigma_{zx,2} &= \rho_s \omega^2 \left[i r_2^* \gamma_2 A_3 e^{-kr_2^*(z-H)} - \delta_2 A_6 e^{-ks_2^*(z-H)} \right] \\ \sigma_{zz,2} &= \rho_s \omega^2 \left[\delta_2 A_3 e^{-kr_2^*(z-H)} + \gamma_2 i s_2^* A_6 e^{-ks_2^*(z-H)} \right] \end{aligned} \quad (3.27)$$

with, $\gamma_2 = 2(kc_{T,s}/\omega)^2$ and $\delta_2 = \gamma_2 - 1$. At this stage, the governing boundary problem for the layered medium is obtained by imposing the following boundary conditions:

$$\sigma_{zx,1} = 0, \quad \sigma_{zz,1} = 0 \quad \text{for } z = 0, \quad (3.28)$$

$$u_1 = u_2, \quad w_1 = w_2 \quad \text{for } z = H, \quad (3.29)$$

$$\sigma_{zx,1} = \sigma_{zx,2}, \quad \sigma_{zz,1} = \sigma_{zz,2} \quad \text{for } z = H. \quad (3.30)$$

namely, zero stresses at the medium free surface, Eq. (3.28), and continuity of displacements and stresses at the interface between the resonant layer and the half-space, Eq. (3.29), and Eq. (3.30), respectively. By exploiting the identities $A_2 = -A_4\delta_1/(ir_1\gamma_1)$ and $A_5 = A_1\delta_1/(is_1\gamma_1)$, we can reduce the boundary problem to a set of four independent equations. In particular, the continuity of displacements at the interface can be rewritten as:

$$\begin{aligned} i(\cos P - \frac{\delta_1}{\gamma_1}\cos Q)A_1 - (\frac{\delta_1}{r_1\gamma_1}\sin P + s_1\sin Q)A_4 - iA_3 + s_2^*A_6 &= 0 \\ (r_1\sin P + \frac{\delta_1}{s_1\gamma_1}\sin Q)A_1 + i(-\frac{\delta_1}{r_1\gamma_1}\cos P + \cos Q)A_4 - r_2^*A_3 - iA_6 &= 0 \end{aligned} \quad (3.31)$$

where $P = kr_1H$ and $Q = ks_1H$. Similarly, the equilibrium condition on the tangential and normal stresses at the interface can be reformulated as:

$$\begin{aligned} i(r_1\gamma_1\sin P + \frac{\delta_1^2}{s_1\gamma_1}\sin Q)A_1 + \delta_1(\cos P - \cos Q)A_4 - \frac{\rho_s}{\rho_{eff}}(ir_2^*\gamma_2A_3 - \delta_2A_6) &= 0 \\ \delta_1(\cos P - \cos Q)A_1 + i(\frac{\delta_1^2}{r_1\gamma_1}\sin P + s_1\gamma_1\sin Q)A_4 - \frac{\rho_s}{\rho_{eff}}(\delta_2A_3 + is_2^*\gamma_2A_6) &= 0 \end{aligned} \quad (3.32)$$

The system of equations (3.31) and (3.32), can be rearranged in matrix form:

$$\begin{bmatrix} i(\cos P - \frac{\delta_1}{\gamma_1}\cos Q) & -\frac{\delta_1}{r_1\gamma_1}\sin P - s_1\sin Q & -i & s_2^* \\ r_1\sin P + \frac{\delta_1}{s_1\gamma_1}\sin Q & i(-\frac{\delta_1}{r_1\gamma_1}\cos P + \cos Q) & -r_2^* & -i \\ i\rho_{eff}(r_1\gamma_1\sin P + \frac{\delta_1^2}{s_1\gamma_1}\sin Q) & \rho_{eff}\delta_1(\cos P - \cos Q) & -i\rho_s\gamma_2r_2^* & \rho_s\delta_2 \\ \rho_{eff}\delta_1(\cos P - \cos Q) & i\rho_{eff}(\frac{\delta_1^2}{r_1\gamma_1}\sin P + s_1\gamma_1\sin Q) & -\rho_s\delta_2 & -\rho_s i\gamma_2s_2^* \end{bmatrix} \begin{bmatrix} A_1 \\ A_4 \\ A_3 \\ A_6 \end{bmatrix} = \begin{bmatrix} 0 \\ 0 \\ 0 \\ 0 \end{bmatrix} \quad (3.33)$$

which can be written in a compact form as $\mathbf{D}(k, \omega)\mathbf{A} = \mathbf{0}$.

Non-trivial solutions of Eq. (3.33) are found by imposing the $\det(\mathbf{D}(k, \omega)) = 0$. Solutions of such nonlinear equation in the variables ω and k provide the dispersive properties of surface waves propagating in the layered resonant medium.

3.2.4 Limit case: Dispersion relation of a full resonant half-space

We first consider a limit case in which the whole half-space is resonant $z = H$. In this configuration, it is necessary to specify only the potential functions in the resonant layer. As in the previous derivation, we restrict our search to wave solutions confined to the surface by assuming potentials with the form:

$$\begin{aligned}\Phi_1(x, z, t) &= a_1 e^{ikr_1^* z} e^{i(\omega t - kx)}, \\ \Psi_{y,1}(x, z, t) &= b_1 e^{iks_1^* z} e^{i(\omega t - kx)}\end{aligned}\quad (3.34)$$

where:

$$r_1^* = \sqrt{\left(1 - \frac{\omega}{kc_{L,eff}}\right)^2}, \quad s_1^* = \sqrt{\left(1 - \frac{\omega}{kc_{T,eff}}\right)^2} \quad (3.35)$$

The dispersion relation of a resonant half-space can be obtained by expressing the stress components in the resonant medium, Eq. (3.25), as functions of the potentials in Eq. (3.34) and imposing the free-stress boundary conditions at the surface of the half-space, Eq. (3.28). The procedure yields a system of two homogeneous equations:

$$\begin{bmatrix} -2i\sqrt{1 - \left(\frac{\omega}{kc_{L,eff}}\right)^2} & 2 - \left(\frac{\omega}{kc_{T,eff}}\right)^2 \\ \left(\frac{\omega}{kc_{T,eff}}\right)^2 - 2 & -2i\sqrt{1 - \left(\frac{\omega}{kc_{T,eff}}\right)^2} \end{bmatrix} \begin{bmatrix} a_1 \\ b_1 \end{bmatrix} = \begin{bmatrix} 0 \\ 0 \end{bmatrix}. \quad (3.36)$$

Non-trivial solutions of Eq. (3.36) provide the dispersion law for Rayleigh waves in a resonant half-space:

$$\left(2 - \left(\frac{\omega}{kc_{T,eff}}\right)^2\right)^2 - 4\sqrt{1 - \left(\frac{\omega}{kc_{T,eff}}\right)^2} \sqrt{1 - \left(\frac{\omega}{kc_{L,eff}}\right)^2} = 0. \quad (3.37)$$

Note that Eq. (3.37) has the same form of the classical expression of Rayleigh waves in a homogeneous medium [96], here adapted with the “effective” velocities of the elastic half-space, namely $c_{L,eff}$ and $c_{T,eff}$.

In the following section, we utilize the obtained analytical formulation in Eqs. (3.33) and (3.37) to evaluate and discuss the dispersive properties of surface waves propagating through resonant layers with different thicknesses.

3.3 Case study: Dispersive properties of seismic barriers

To validate our analytical framework and discuss the fundamental dispersive features of surface waves in resonant materials, we consider the scenario of an array of meter-size resonators, known as metabarrier [88], embedded in the soil to attenuate the propagation of seismic surface waves and ground vibrations. The validation of our approach, which comprises the effective medium description and

the related dispersion relations is performed by comparing the predictions of the analytical models with the numerical outcomes of finite element models, where the resonant unit cells are modeled accounting for their exact geometries and mechanical parameters.

The configuration of interest is displayed in Fig. 3.3a. It comprises a layer of resonators embedded in the soil and arranged periodically in a square lattice of spacing a , for an overall depth H . Each unit cell consists of a resonator attached to the host medium via elastic connectors, modeled as discrete springs, with identical horizontal and vertical stiffness K , as schematically shown in Fig. 3.3b. In our numerical investigations, we resort to a unit cell (see Fig. 3.3b) with length $a = 1$ [m], with a square hole of length $a_v = 0.6a$ enclosing a resonator of dimensions $a_r \times a_r = 0.25a^2$. The host medium is a soft soil with mass density $\rho_h = 1500$ [kg/m^3], and bulk longitudinal and shear velocities of $c_{L,h} = 335$ [m/s], and $c_{T,h} = 120$ [m/s] [88], respectively. The 2D plane-strain model has an out-of-plane thickness $t = 1$ [m]. The mass of the resonator is $m_r = \rho_r a_r^2 t$, where $\rho_r = 2400$ [kg/m^3] is the mass density, and $\omega_r = 2\pi f_r$ is the angular resonant frequency of the resonator, with $f_r = 5$ Hz.

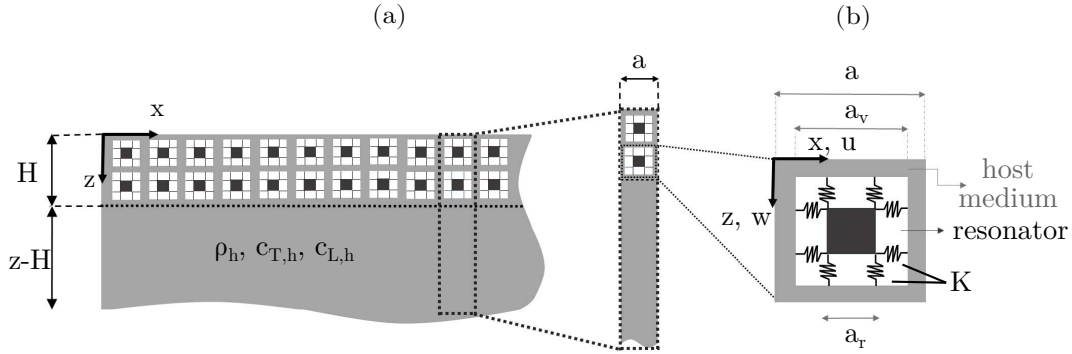


Figure 3.3: (a) Schematics of the resonant layer with a regular grid of embedded resonators overlying a homogeneous half-space. In the inset is shown a representative strip of the bilayered half-space. (b) Barrier unit cell.

Under the assumptions of the analytical model (Sec. 3.2), we restrict our analysis to the low-frequency range where the dimensions of the resonators are much smaller than both the wavelength and the penetration depth of the fundamental surface mode. In this scenario, the density of the resonant unit can be adequately described using the approach discussed in Sec. 3.2. Similarly, we approximate the elastic response of the composite material as an effective isotropic medium. In doing so, we neglect the orthotropic behavior induced by the square lattice arrangement of the resonators. Still, we demonstrate that this approach can capture the fundamental physics of the considered problem.

3.3.1 Effective resonant layer model of the seismic barrier

Static Homogenization for the derivation of elastic moduli

To characterize the elastic properties (M_{eff} and μ_{eff}) of the unit cell, we utilize the procedure discussed in Sec. 3.2. The calculation of the average stresses is performed via FE simulations using the software Comsol Multiphysics [161]. In more detail, we model a unit cell of the barrier under plane-strain conditions using Lagrange quadrilateral elements to discretize the host material and truss elements for the springs connecting the host material to the resonator. For the calculation of the longitudinal modulus, we impose a unitary lateral pressure load to the unit cell restraining its top and bottom boundaries along the vertical direction (see Fig. 3.4a). Fig. 3.4c and Fig. 3.4e depict the obtained longitudinal stress and strain distributions, respectively. We calculate the average stress $\bar{\sigma}_{xx}$ and strain $\bar{\epsilon}_{xx}$ components within the host medium, and estimate an effective longitudinal modulus $M_{eff} = \bar{\sigma}_{xx}/\bar{\epsilon}_{xx} = 36.37$ [MPa].

For the calculation of the shear modulus μ_{eff} we impose a unitary horizontal displacement at the top surface of the unit cell, restraining the bottom boundary along the horizontal direction (Fig. 3.4b). Additionally, we impose continuity conditions along the unit cell lateral boundaries to simulate the effect of neighboring unit cells. Fig. 3.4d and Fig. 3.4f show the obtained shear stress and strain distributions, respectively. From the average stress $\bar{\sigma}_{xz}$ we estimate an effective shear modulus $\mu_{eff} = \bar{\sigma}_{xz}/\bar{\gamma}_{xz} = 3.66$ [MPa].

For the calculation of the unit cell effective mass density (EMD), we utilize Eq. (3.1). Given the regular arrangement of the resonators, we consider as reference volume the one of a unit cell which encloses a single resonator, i.e., $V = a^2t = 1$ [m³] and $n = 1$ in Eq. (3.1). As a result, the static density of the homogenized medium is $\rho_0 = (m_h + m_r)/V = 1560$ [kg] with $m_h = \rho_h(a^2 - a_v^2)t = 960$ [kg] being the mass of the external host medium enclosed in a unit cell; whereas the mass ratio $\alpha = m_r/(V\rho_0) = 0.384$.

FE verification of the adopted static homogenization

We develop FE numerical model to extract the effective velocities of the resonant metamaterial and verify the efficiency of the adopted static homogenization approach. To this end, we estimate the bulk velocities of the resonant composite first and then calculate the effective bulk velocities of the homogenized composite in the long-wavelength range. The finite element model of the unit cell presented in Fig. 3.5a is again developed in Comsol Multiphysics. The material properties of the host media, resonator, and elastic spring are given in Sec. 3.2.1 are assigned to the model. Bloch periodic condition is applied to the lateral edges of the model to extract the dispersion of the bulk waves propagating in one of the principle directions (e.g.,

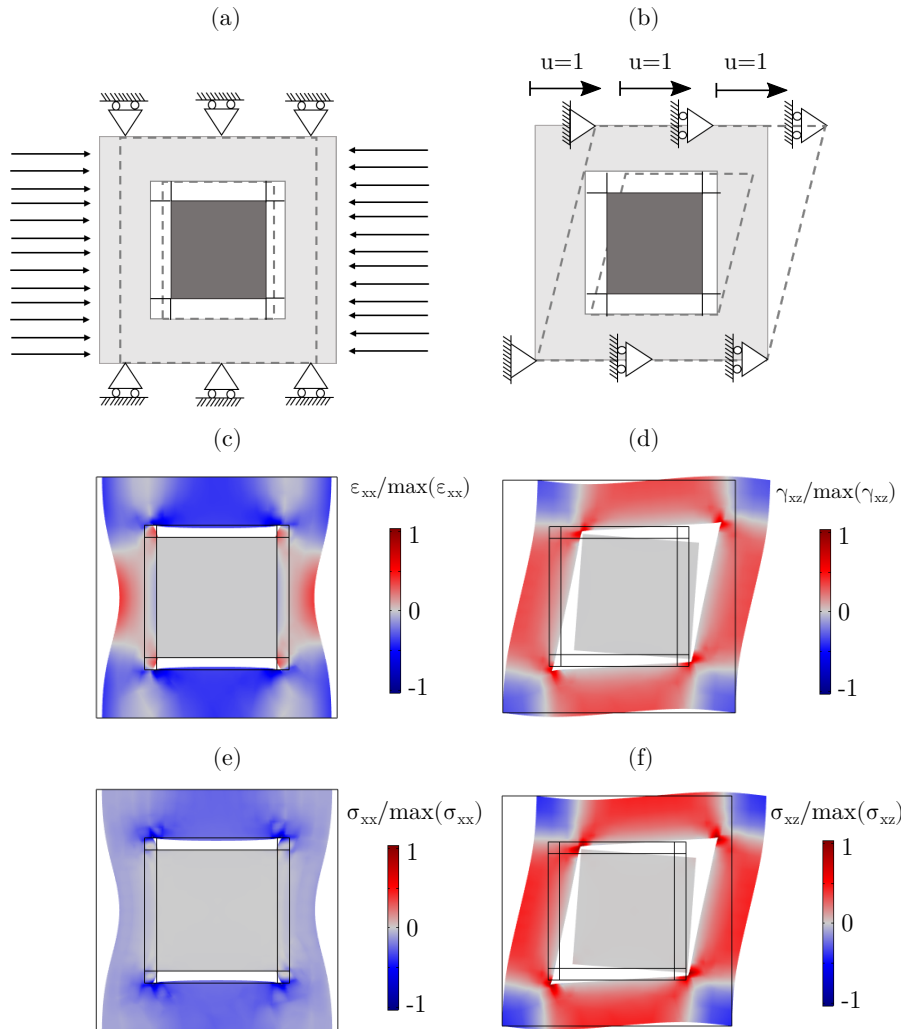


Figure 3.4: (a) Schematics of the FE model used to calculate the longitudinal modulus M_{eff} , and (b) shear modulus μ_{eff} of the resonant barrier. Longitudinal strain (c) and stress (e) components are associated with the uniaxial constrained deformation state. Shear strain (d) and stress (f) components are associated with the pure shear deformation state.

x -direction), considering the symmetry of the resonant cell. The eigenfrequency response of the resonant cell in the long-wavelength regime is plotted in Fig. 3.4b. $c_{L,est} = 153 [m/s]$ and $c_{T,est} = 49 [m/s]$ are the estimated longitudinal and shear wave speeds obtained from blue and red tangent lines, respectively. These values are extracted from small wavenumbers ($k \approx 0$), where the dispersion curve presents almost linear trends.

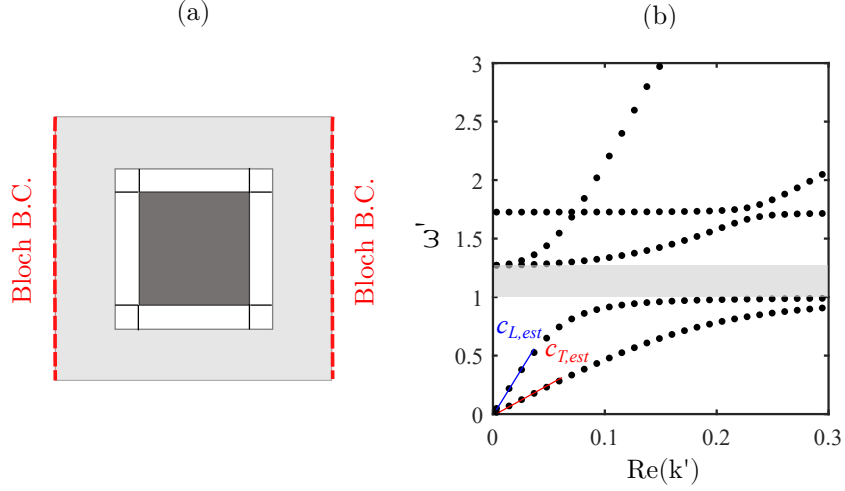


Figure 3.5: (a) Developed FE unit cell in Comsol Multiphysics. (b) Numerical dispersion relation of the unit cell used to extract the equivalent shear and longitudinal velocities of the cell.

We use the estimated velocities to calculate the elastic modulus, Poisson's ratio, and elastic moduli of the resonant composite as follow:

$$\begin{aligned}
 E_{est} &= \rho_{st} c_{T,est}^2 \left(\frac{3c_{L,est}^2 - 4c_{T,est}^2}{c_{L,est}^2 - c_{T,est}^2} \right)^2, \\
 \nu_{est} &= \frac{c_{L,est}^2 - 2c_{T,est}^2}{2(c_{L,est}^2 - c_{T,est}^2)}, \\
 \mu_{est} &= \frac{E_{est}}{2(1 + \nu_{est})}, \\
 \lambda_{est} &= \frac{E_{est}\nu_{est}}{(1 + \nu_{est})(1 - 2\nu_{est})},
 \end{aligned} \tag{3.38}$$

The effective description of the considered resonant metamaterial defines dispersive longitudinal $c_{L,eff}(\omega)$ and shear $c_{T,eff}(\omega)$ effective bulk velocities as:

$$c_{T,eff}(\omega) = \sqrt{\frac{\mu_{est}}{\rho_{eff}(\omega)}} \tag{3.39}$$

$$c_{L,eff}(\omega) = \sqrt{\frac{\lambda_{est} + 2\mu_{est}}{\rho_{eff}(\omega)}} \quad (3.40)$$

We remark that the effective bulk velocities obtained from Eq.(3.40) and Eq.(3.39) are identical to those of Eq.(3.4) and Eq.(3.5).

Effective bulk velocities

The value of the effective density calculated as per Eq. (3.1) is reported in Fig. 3.6a in terms of normalized density $\rho' = \rho_{eff}/\rho_0$ and normalized angular frequency $\omega' = \omega/\omega_r$. As shown in the literature, the effective density assumes negative values in the interval $\omega' \in [1, (1/(1-\alpha))^{1/2}]$ due to the out-of-phase motion between the internal oscillator and the host medium. Conversely, in the long-wavelength (low-frequency) limit, the density recovers its static value $\rho_{eff}(\omega = 0) = \rho_0$, while in the high-frequency limit it approaches $\rho_{eff}(\omega = \infty) = m_h/V$, namely the resonator mass does not contribute to the unit cell effective inertia.

Knowledge of the effective density and effective longitudinal and shear moduli allow us calculating the bulk velocities of the resonant layer to approximate the dynamics of the seismic barrier in the low-frequency range.

In Fig. 3.6b, the values of the bulk velocities, which are normalized by the shear velocity of host medium $c_{T,h}$, are reported in the normalized frequency range $\omega' = [0, 3]$. As expected, in the frequency range where the effective mass density of the cell assumes negative values, the effective bulk velocities have null real components (Fig. 3.6b) and non-null imaginary values with an asymmetric profile (Fig. 3.6c) characteristic of a resonant type frequency bandgap (BG). It is noted that the BG of both the bulk modes occurs within the same frequency region due to the isotropic behavior of the resonators.

3.3.2 Dispersive properties of a deep seismic barrier modeled as a resonant half-space

We start our investigation considering a configuration where the depth of the barrier, namely the depth of the resonant layer, has a thickness of $H \gg \lambda$. In this scenario, we can neglect the presence of the homogeneous substrate and exploit the analytical relation derived for the case of a resonant half-space, Eq. (3.37), to predict the dispersive properties of Rayleigh-like waves.

In particular, we seek for the complex wavenumbers $k = \Re(k) + i\Im(k)$ of Eq. (3.37) in the dimensionless angular frequency range $\omega'=[0, 2.5]$, where the resonance modes of the unit cell should be found. The real $\Re(k')$ vs. ω' and imaginary $\Im(k')$ vs. ω' dispersion curves, calculated using a bisection root-finding scheme, are shown in Fig. 3.7a, and Fig. 3.7b, respectively, by continuous black

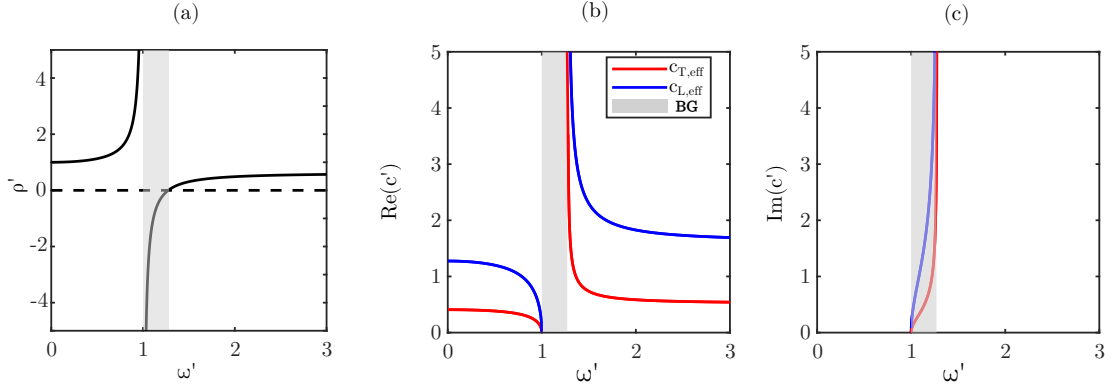


Figure 3.6: Effective properties of the resonant barrier. (a) Effective mass density. (b) Effective velocities of propagating bulk waves and (c) evanescent bulk waves. Shaded areas indicate the bandgap associated with negative EMD and purely imaginary values of the effective velocities.

lines. The black dashed line in Fig. 3.7a denotes the non-dispersive roots of the Rayleigh wave solutions in the homogeneous soil (hosting medium).

We observe that the resonant half-space is characterized by a BG for the surface waves in the frequency range where the EMD is negative. This result can be interpreted by recalling that a Rayleigh wave stems from the interaction between the bulk longitudinal and shear waves. Hence, in the frequency range where bulk waves are impeded by the resonant metamaterial, the Rayleigh solutions cannot propagate too.

Additionally, we observe that the Rayleigh mode in the resonant medium decay with an attenuation, i.e., $\Im(k_{R,eff})$, that is comparable to the one of a shear wave ($\Im(k_{T,eff})$) and greater than the one of the longitudinal bulk mode ($\Im(k_{L,eff})$), see Fig. 3.7b. This occurs because the imaginary component of the wavenumber is inversely proportional to the imaginary component of the velocity, namely $\Im(k) = \frac{\omega}{\Im(c)}$. Thus, the ratio $\frac{\Im(k_{R,eff})}{\Im(k_{L,eff})}$ is equal to the ratio of the velocities $\frac{\Im(c_{L,eff})}{\Im(c_{R,eff})}$ (compare Fig. 3.6b to Fig. 3.7d). Interestingly, the ratio of the velocities does not vary within the gap and is equal to the ratio of the real components $\frac{\Re(c_{L,eff})}{\Re(c_{R,eff})}$, calculated at any frequency outside the gap (compare Fig. 3.7c to Fig. 3.6a). Since the latter ratio is always larger than 1 for any material, the same result applies to the ratio $\frac{\Im(k_{R,eff})}{\Im(k_{L,eff})}$. Similar arguments apply to the comparison between Rayleigh and shear waves.

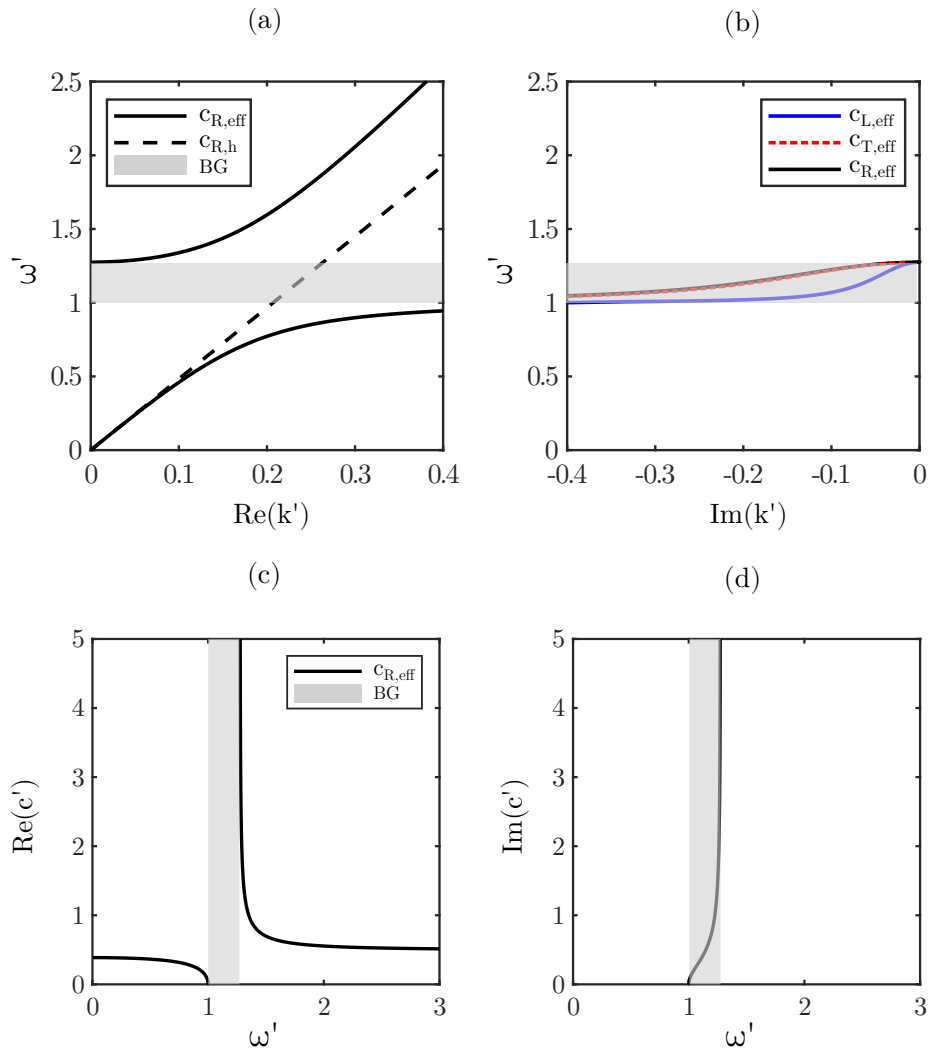


Figure 3.7: (a) Real and (b) imaginary wavenumber for the dispersion of Rayleigh waves propagating across a full resonant half-space, respectively. (c) Real and (d) imaginary parts of the effective Rayleigh wave velocity in the resonant medium, respectively.

Rayleigh-like mode shapes in the resonant half-space

We now exploit the effective medium description to reconstruct the Rayleigh-like mode shapes within the resonant half-space as [96]:

$$\begin{aligned} u_r &= -ikB_1e^{-\eta z} + B_2\zeta e^{-\zeta z} \\ w_r &= -\eta B_1e^{-\eta z} - ikB_2e^{-\zeta z} \end{aligned} \quad (3.41)$$

where u_r and w_r are the amplitudes of the horizontal and vertical components of the eigenmode, respectively, $\eta = (k^2 - (\omega/c_{L,eff})^2)^{1/2}$, $\zeta = (k^2 - (\omega/c_{T,eff})^2)^{1/2}$, and z is the coordinate depth of the resonant half-space. The constants B_1 and B_2 are arbitrarily chosen to satisfy Eq. (3.41), for example $B_2 = 1$ and $B_1 = (-2i\zeta k)/(\zeta^2 + k^2)$.

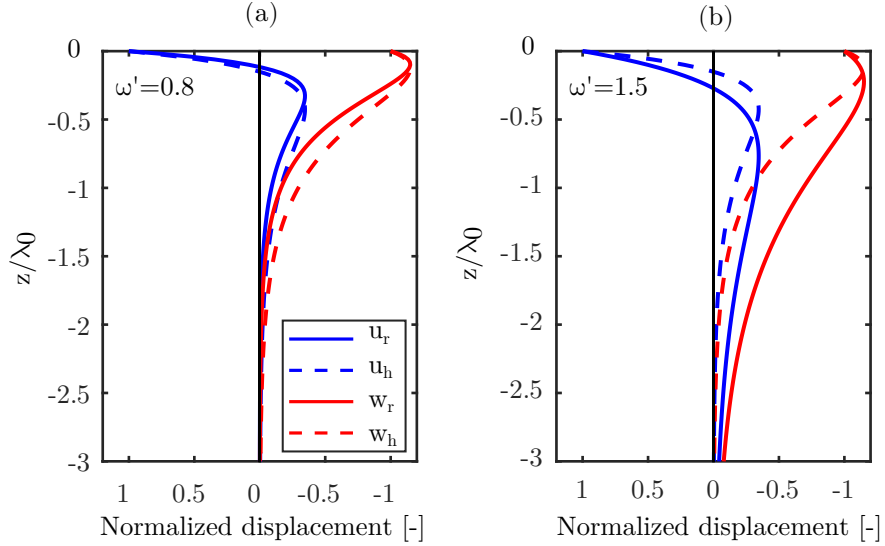


Figure 3.8: Rayleigh wave mode shapes in resonant half-space (continuous lines) and in the host medium (dashed lines) computed for a dimensionless circular frequency of (a) $\omega' = 0.8$ (in-phase), and (b) $\omega' = 1.5$ (out-of-phase).

Examples of Rayleigh-like mode shapes propagating within the resonant half-space at the normalized frequency $\omega' = 0.8$ and $\omega' = 1.5$ corresponding to the in-phase (lower) and the out-of-phase (upper) dispersive branches are shown in Fig. 3.8a and 3.8b, respectively. The reader can compare these eigenshapes with those of the Rayleigh wave propagating in the homogeneous host medium (u_h, w_h), i.e., soil with no resonators (dashed lines in Fig. 3.8). The displacements are normalized by their corresponding absolute value at $z = 0$ and are represented along the normalized depth coordinate z/λ_0 , where $\lambda_0 = 2\pi c_{R,h}/\omega_r$, and $c_{R,h} = 113.5$ [m/s] denotes the Rayleigh velocity of the host material. Comparison between Rayleigh

modes in the resonant and non-resonant half-spaces propagating at a frequency slightly lower than the BG reveals that the mode is more confined to the surface due to the lower effective velocity. In analogy, modes above the bandgap are less confined due to the larger effective velocity.

FE Validation

To verify the analytical predictions provided by the proposed effective medium approach, we develop a bi-dimensional Finite Element (FE) model to compute the roots of the dispersion relation. To this aim, we model a representative strip of the resonant half-space in plane-strain condition, with a depth of $3\lambda_0$ and a width equal to that of the resonant unit cell $a \ll \lambda_0$, as shown in Fig. 3.9a. The depth of the strip is adequate to simulate a half-space domain in the frequency range around the unit cell resonance.

The base displacement of the strip in Fig. 3.9a is restricted both horizontally and vertically to prevent any undesirable rigid motion. Bloch boundary conditions are applied along the side edges of the model to replicate the dynamics of an infinite half-space in the x -direction. To accurately model the shortest wavelength at the highest frequency of interest, the domain is discretized by Lagrange quadrilateral elements with minimum and maximum dimensions of $d_{min} = a/10$ and $d_{max} = a/5$, respectively.

The eigensolutions of the FE problem for given real wavenumbers from zero to $k' = 0.4$ are marked by dots in Fig. 3.9b, whereas our analytical solutions of Eq. (3.37) are reported in continuous black lines. The numerical model predicts a plethora of solutions that include several bulk-like modes. To discriminate between surface solutions and the bulk modes, we use a selection criterion based on the position of the displacement shape centroid G_r within the strip depth:

$$G_r = \frac{\int_0^{3\lambda_0} |w|z dz}{\int_0^{3\lambda_0} |w| dz} < 0.9\lambda_0 \quad (3.42)$$

thus selecting only those modes with a displacement centroid located within the uppermost region of the model depth. The analytical predictions well match the surface modes selected according to this criterion, which are marked by blue dots in Fig. 3.9b. Furthermore, the numerical model predicts a flat branch of eigensolutions at $\omega' = 1.72$, resulting from the rotational motion of the resonators (see detail in Fig. 3.9d).

We now analyze some of the mode shapes obtained from the numerical model. For better visualization, we display the wavefield by replicating the eigenmode of the unit cell with a phase shift e^{ikx} along the direction of wave propagation. The surface mode with angular frequency $\omega' = 0.91$, and wavenumber $k' = 0.3$ is shown

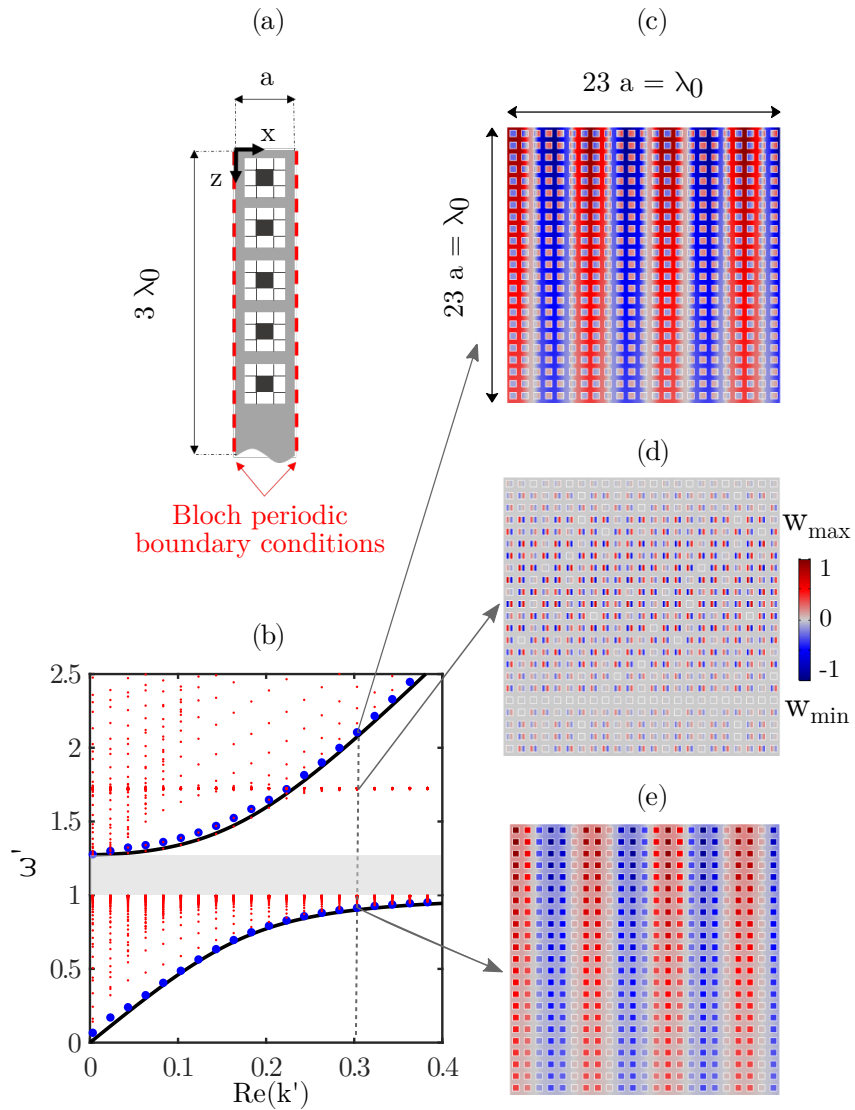


Figure 3.9: (a) Schematic of a strip of the resonant half-space. (b) Dispersion relation of the resonant half-space. Solid lines present the analytical solutions, and circles mark the FE eigensolutions (blue dots denote the surface modes). (c) Zoom-in on the wavefield ($H = \lambda_0$) of a surface mode computed at $\omega' = 2.11$ and $k' = 0.3$ showing an out-of-phase displacement between the internal mass and the host medium; (d) rotating mode at $\omega' = 1.72$ and $k' = 0.3$; (e) surface mode computed at $\omega' = 0.91$ and $k' = 0.3$ with in-phase motion between the host medium and the internal resonant mass.

in Fig. 3.9e. We note that each resonator moves in-phase with the motion of the host medium (the color in Fig. 3.9e denotes the w displacement amplitude), as observed along the acoustic branch of any resonant waveguide. Conversely, the wavefield at $\omega' = 2.11$ and $k' = 0.3$ is characterized by an out-of-phase motion between the resonator and the hosting medium, which is typical of the optical branch of resonant materials (see Fig. 3.9c).

3.3.3 Dispersion of finite-depth seismic barriers

We now generalize our investigation by calculating and discussing the dispersive properties of Rayleigh-like waves traveling in a seismic barrier of depth H , modeled as a resonant layer of the same depth, overlaying a half-space of homogeneous soil. We aim to find the roots of $\det(\mathbf{D}(k, \omega)) = 0$, calculated as per Eq. (3.33), within the frequency range where we expect to observe the Rayleigh wave bandgap. To this purpose, we calculate the determinant within the frequency range $\omega' = [0, 2.5]$ and wavenumber range $k' = [0, 0.5]$, and visualize its minimal values in Fig. 3.10a for a resonant layer of depth $H = \lambda_0$. Note that this depth corresponds roughly to a barrier of 23 unit cells.

Different from the resonant half-space scenario, the bilayer medium supports the propagation of multiple surface modes (marked by blue lines in Fig. 3.10a). These surface waves are hybridized by the unit cell resonant modes. The hybridization leads to the generation of a low-frequency resonant bandgap, bounded between the resonance frequency of the barrier ω_r and the crossing point between the bulk shear velocity $c_{T,h}$ of the half-space, and fundamental hybridized mode marked as a continuous black line in Fig. 3.10a.

The half-space shear velocity identifies the $(\omega' - k')$ domain, labeled as sound-cone and highlighted by a dark gray area in Fig. 3.10a, where purely surface-confined modes cannot exist because s_2^* in Eq. (3.21) assumes imaginary values. Inside this domain, we should instead observe leaky surface modes, which radiate part of their energy into the half-space. For example, by tracking the fundamental mode, i.e., by solving $\det(\mathbf{D}(k, \omega)) = 0$ numerically for the unknown complex wavenumbers $k = \Re(k) + i\Im(k)$, we can verify that a branch of this mode extends within the sound-cone. Additionally, we observe that the same mode becomes evanescent $\Re(k) = 0$, and $\Im(k) \neq 0$, within the frequency BG of the bulk modes, where both r_1 and s_1 in Eq. (3.19) assume imaginary values (see Fig. 3.10b).

We extend our investigation considering configurations with different resonant layer depths, $H = [0.2, 0.5, 1, 2]\lambda_0$, with $H = 0.2\lambda_0$ roughly corresponding to a barrier of five unit cells and $H = 2\lambda_0$ corresponding to a barrier of 46 unit cells along with the depth of the resonant layer, respectively. The related real dispersive properties are shown in Figs. 3.11(a)-(d). A comparison between the analyzed scenarios shows that an increase in the thickness of the resonant layer widens the

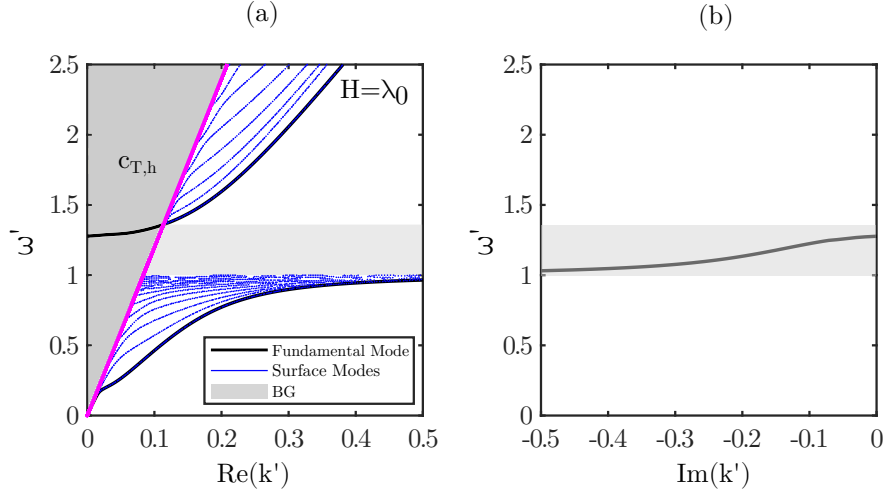


Figure 3.10: Dispersion relation of (a) propagating and (b) evanescent Rayleigh waves in a resonant layer with a depth of $H = \lambda_0$ overlaying a homogeneous half-space. The fundamental surface mode is marked by black lines.

frequency range of the BG. To quantify this behavior, we calculate the BG extension for different depths of the resonant layer by visually inspecting the crossing point of fundamental surface mode and shear velocity of half-space.

The bandgap evolution in terms of normalized angular frequency is shown in Fig. 3.11e for the normalized variation depth (H/λ_0) of the resonant layer. We observe a linear trend for resonant layers with $H < 0.5\lambda_0$. The BG extension reaches a maximum value $\omega'_{RL} = 1.37$ for $H \geq 0.5\lambda_0$, which is larger than the bandgap of a resonant half-space, whose upper edge ω'_{HS} is indicated in Fig. 3.7a. The latter result can be interpreted by recalling that in the resonant layered system two attenuation mechanisms contribute to prevent the propagation of Rayleigh waves. First, as in the case of a fully resonant half-space, the bulk modes within the resonant layer are impeded within the frequency range where the effective density assumes negative values. As a result, the surface modes which stem from the superposition of these bulk modes (see Eq. (3.18)) are inhibited. Second, within an additional frequency range above the bulk waves BG, the apparent phase velocity of the surface modes assumes values $c > c_{T_h}$. This condition allows only the existence of leaky modes that disperse their energy in the half-space region, as discussed for the barrier with $H = \lambda_0$.

Regarding the case of a thin resonant layer, we underline that its dispersive properties can be equally predicted by treating the presence of the resonators as a stress boundary condition on the half-space (see Appendix A). This description, widely employed in literature to describe the dynamics of metasurfaces, yields a

closed-form estimation of the upper edge frequency of the BG [88]:

$$\omega'_{MS} = \beta + \sqrt{\beta^2 + 1}, \quad (3.43)$$

where:

$$\beta = \frac{m_{res} \omega_r}{2a_{res} \rho_h c_{T,h}} \sqrt{1 - \left(\frac{c_{T,h}}{c_{L,h}}\right)^2}. \quad (3.44)$$

The reader can appreciate that this prediction, marked by a red dashed line in Fig. 3.11e, well matches the BG extension of a thin $H = 0.05\lambda_0$ resonant layer, i.e., approximately a single unit cell layer, calculated according to our framework.

A single-resonator barrier modeled as a locally resonant metasurface

The dynamics of a resonant layer with a very thin depth, for example, the case of a barrier with one unit cell ($H = a$), can be adequately described as a resonant metasurface (see Fig. 3.12a), an array of subwavelength mass-spring resonators attached to the free surface of a homogeneous elastic half-space. Such a configuration can be analyzed by modeling the presence of the resonator as a stress distribution applied on the free surface of the half-space [151]. According to this description, the dispersion relation of the resonant metasurface interacting with vertically polarized surface waves reads [153]:

$$\begin{aligned} & \left(\left(\frac{\omega}{\omega_r} \right)^2 - 1 \right) \left[\left(2 - \left(\frac{\omega}{k c_{T,h}} \right)^2 \right)^2 - 4 \sqrt{1 - \left(\frac{\omega}{k c_{L,h}} \right)^2} \sqrt{1 - \left(\frac{\omega}{k c_{T,h}} \right)^2} \right] \\ & = \frac{m_{res} \omega^4}{A \rho_h c_{T,h}^4 k^3} \sqrt{1 - \left(\frac{\omega}{k c_{L,h}} \right)^2} \end{aligned} \quad (3.45)$$

where $A = a_r t$ is an average area where each resonator exerts its stress. In Fig. 3.12b, we compare the dispersive properties of a single layer $H = a$ resonant barrier modeled according to the metasurface description (Eq. (3.45), red dashed lines in Fig. 3.12b) and the framework proposed in our work (Eq. (3.33), black lines in Fig. 3.12b). Both developed models provide analogous results in the case of a thin resonant layer.

FE Validation

To verify the dispersion results found analytically, we develop a dedicated finite element numerical model and perform numerical simulations.

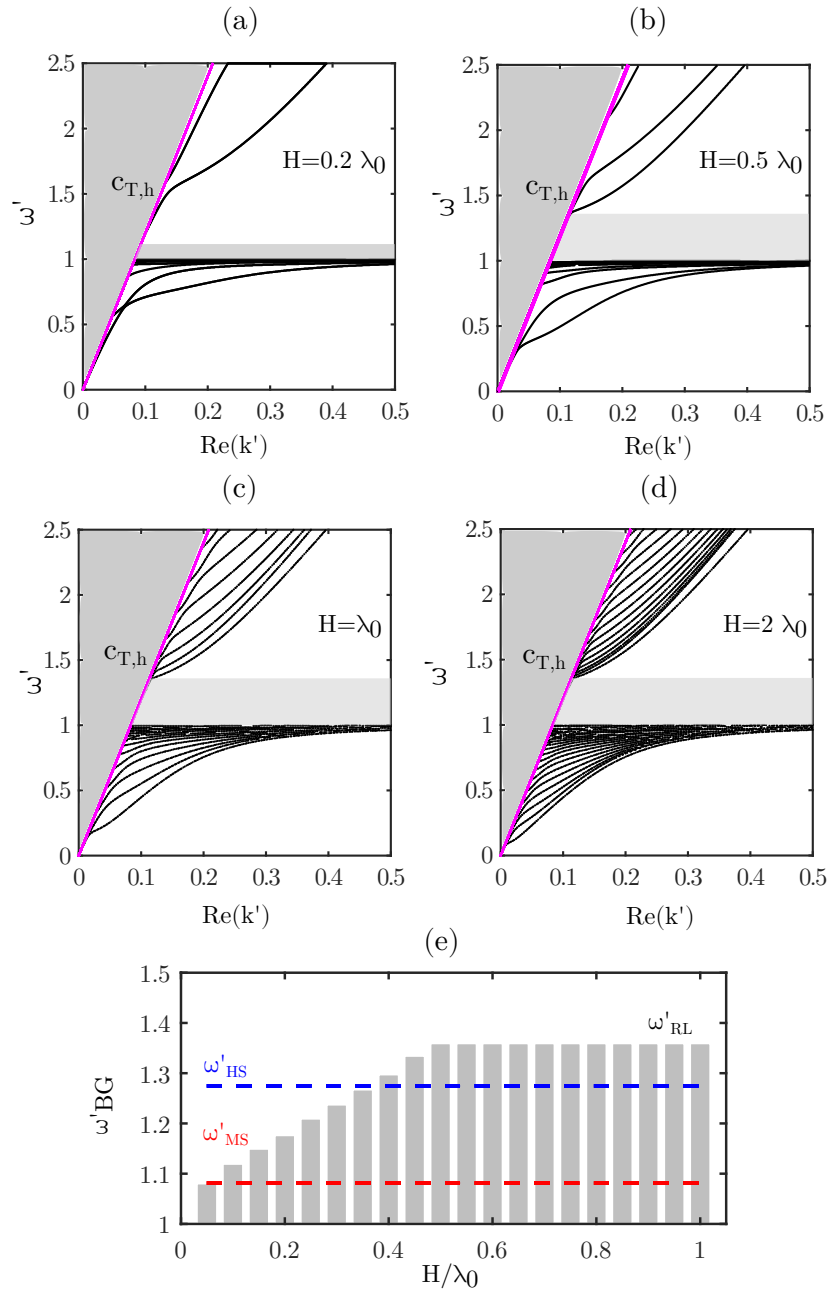


Figure 3.11: Dispersion curves of real wavenumbers for a semi-infinite resonant medium consisting of a homogeneous half-space below a resonant layer with the depth of (a) $H = 0.2\lambda_0$, (b) $H = 0.5\lambda_0$, (c) $H = \lambda_0$, and (d) $H = 2\lambda_0$, respectively. (e) bandgap width in normalized angular frequency vs. normalized depth of the resonant layer. The dashed blue line indicates the BG upper edge of a resonant half-space, while the dashed red line indicates the upper edge for a metasurface.

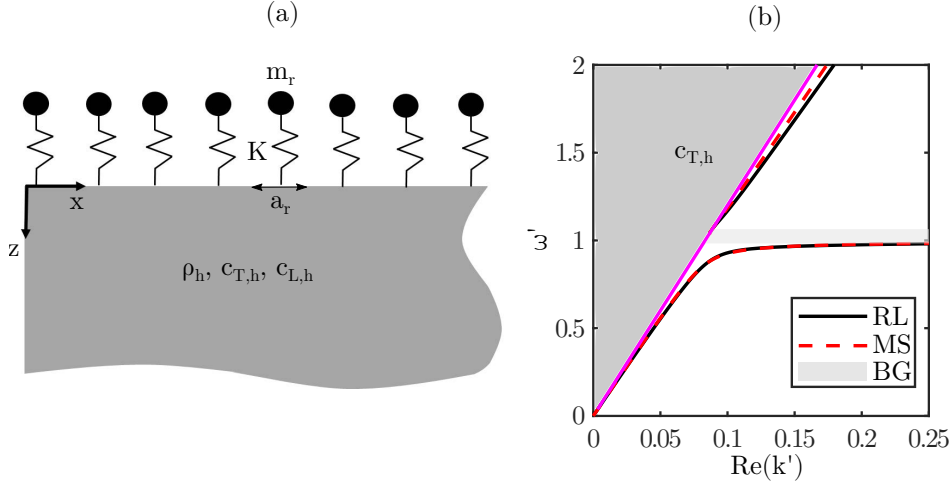


Figure 3.12: (a) Schematic of the metasurface layer attached to the free surface of a homogeneous half-space. (b) Dispersion of the resonant layer composed of single unit cell embedded to host material (RL) vs. locally resonant metasurface (MS).

The FE model depicted in Fig. 3.13c consists of a strip of resonators with depth H placed on top of a homogeneous soil. Following the procedure described for the derivation of the numerical dispersion of the resonant half-space (Sec. 3.2), the numerical eigensolutions (marked by dots) are calculated and over-imposed to the analytical dispersion curves for the two scenarios of thin ($H = 0.2\lambda_0$) and thick ($H = \lambda_0$) resonant layer in Fig. 3.13a and b, respectively. Among all the numerical eigenmodes, surface solutions, highlighted by blue dots, are selected using the identification criterion reported in Eq. (3.42). We note that the numerical model also accounts for multiple rotational modes of the resonators as previously seen in the case of resonant half-space (see Fig. 3.9b), which results in an additional flat branch around $\omega' = 1.72$.

We highlight that the numerical and analytical outcomes are in good agreement. In particular, numerical simulations confirm the same variation of the BG concerning the resonant layer thickness found analytically. Additionally, insight on the dispersive properties of the fundamental surface mode confirms its “leaky” behavior within the sound-cone domain, evident by visualizing the full wavefield of the mode at $k' = 0.08$ and $\omega' = 1.33$, as shown in Fig. 3.13d. The same mode remains instead confined to the surface when computed outside the sound-cone region (see Fig. 3.13e).

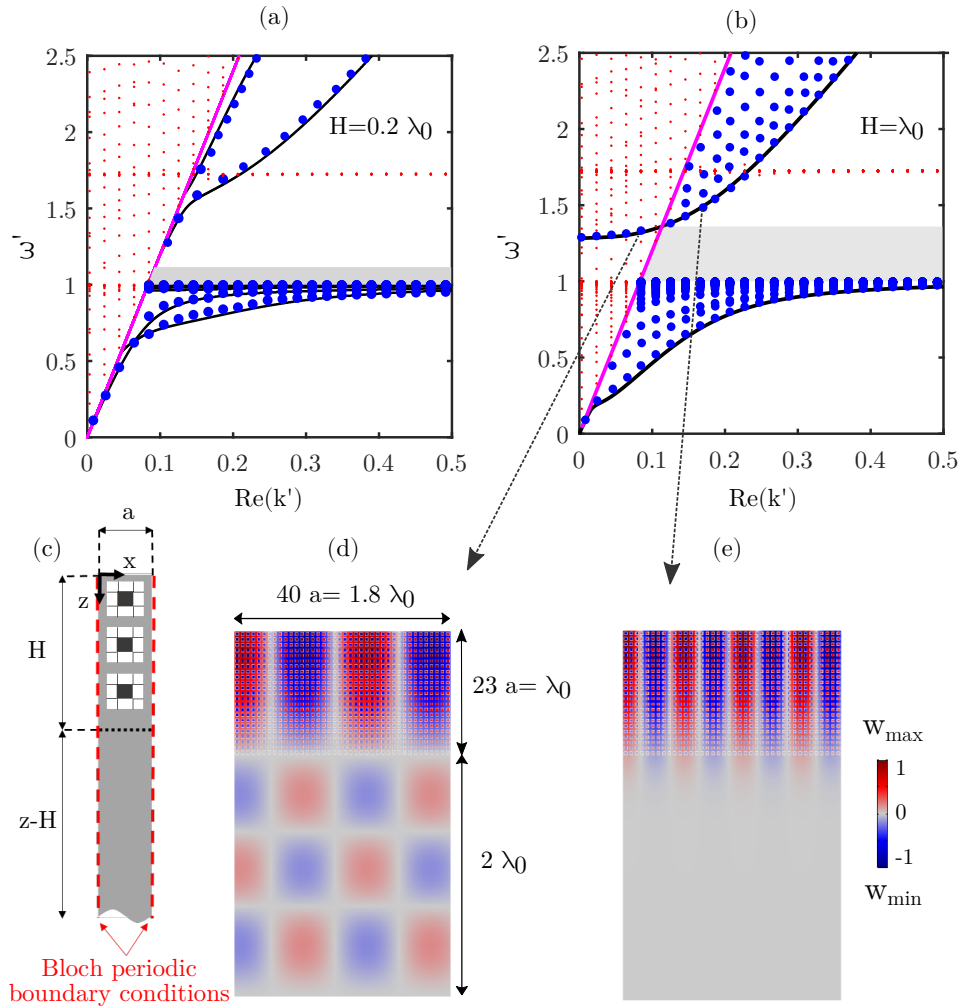


Figure 3.13: (a) FE surface modes (blue dots), discriminated according to the criterion reported in Eq. (3.42), and over-imposed to the analytical dispersion relation (solid lines) for $H = 0.2\lambda_0$ and (b) $H = \lambda_0$. (c) A representative unit cell of a resonant barrier on top of a homogeneous soil. (d) The vertical displacement wavefields of a leaky surface mode corresponding to $k' = 0.08$ and $\omega' = 1.33$. (e) The vertical displacement wavefield of the fundamental surface mode for $k' = 0.18$ and $\omega' = 1.54$. Note that the resonators move out-of-phase with respect to the host medium.

3.4 Rayleigh waves transmission through a finite-length seismic barrier

In this section, we investigate the propagation of Rayleigh waves within a domain composed of a resonant barrier of finite dimensions embedded within a homogeneous non-resonant half-space. Our aim is twofold: first, we want to verify the accuracy of the effective medium description for harmonic analyzes; second, we want to evaluate the attenuation properties of the finite length resonant barrier. To this end, we develop two dedicated finite element models: the first model accounts for the true geometry and materials of the barrier, the second, instead, utilizes an effective resonant medium to replace the barrier. In both models, the domain of interest $L_t \times H_t$, depicted in Fig. 3.14a, has dimensions of $10\lambda_0 \times 3\lambda_0$, respectively. The barrier is located at a distance of $5\lambda_0$ from the input source, with a length of $2\lambda_0$ and a variable depth H . A vertical unitary displacement, applied at a distance $d_s = \lambda_0$ from the domain edge, is used as a point source to generate surface Rayleigh waves. An output region of length $L_{out} = 2\lambda_0$ is used to recover the signal amplitude after the resonant portion. Low reflecting boundary conditions (LRBCs) are applied at the lateral and bottom edges to reduce wave reflections. Both the domains are discretized by Lagrange quadrilateral elements with a minimum and maximum mesh dimension of $d_{min} = a/10$ and $d_{max} = \lambda_0/5$, respectively.

Frequency-domain analyzes are performed within the range of $\omega' = [0.7, 2.5]$ for a resonant layer of thickness $H = \lambda_0$. We define a transmission coefficient calculated as [150]:

$$T(\omega') = \frac{\int_0^{L_{out}} |w_r| dx}{\int_0^{L_{out}} |w_p| dx} \quad (3.46)$$

where w_r is the vertical nodal displacement as calculated from the FE simulations along with the output domain, while w_p is the vertical nodal displacement calculated within the same domain using a twin reference model where the resonant domain is substituted by the homogeneous non-resonant material ($c_{T,h}, c_{L,h}, \rho_h$).

The true barrier model and the effective resonant layer provide analogous values of the transmission coefficient within the whole frequency range of interest (see Fig. 3.14b). Similarly, the vertical displacement wavefields obtained utilizing two FE models (true barrier and effective layer) are in excellent agreement for harmonic analyzes within and outside the bandgap region (see Fig. 3.15a,b for harmonic simulations at $\omega' = 1$ and Fig. 3.15c,d for harmonic simulations at $\omega' = 1.3$). Following the prediction of the dispersion curve reported in Fig. 3.13b, the Rayleigh wave propagation is hindered through the resonant layer for a harmonic excitation within the BG range (see Fig. 3.15b). Besides, Fig. 3.15d highlights the attenuation of a leaky surface mode, which spreads part of its elastic energy below

the barrier.

These results confirm the possibility of using the effective model within a FE approach. Thus, we perform a parametric study and calculate the transmission coefficients of resonant layers with thickness $H = [0.2, 0.5, 1]\lambda_0$. The results are displayed in Fig. 3.16 and prove that the barrier attenuation frequency range varies with the barrier depth, as predicted by the proposed dispersion laws.

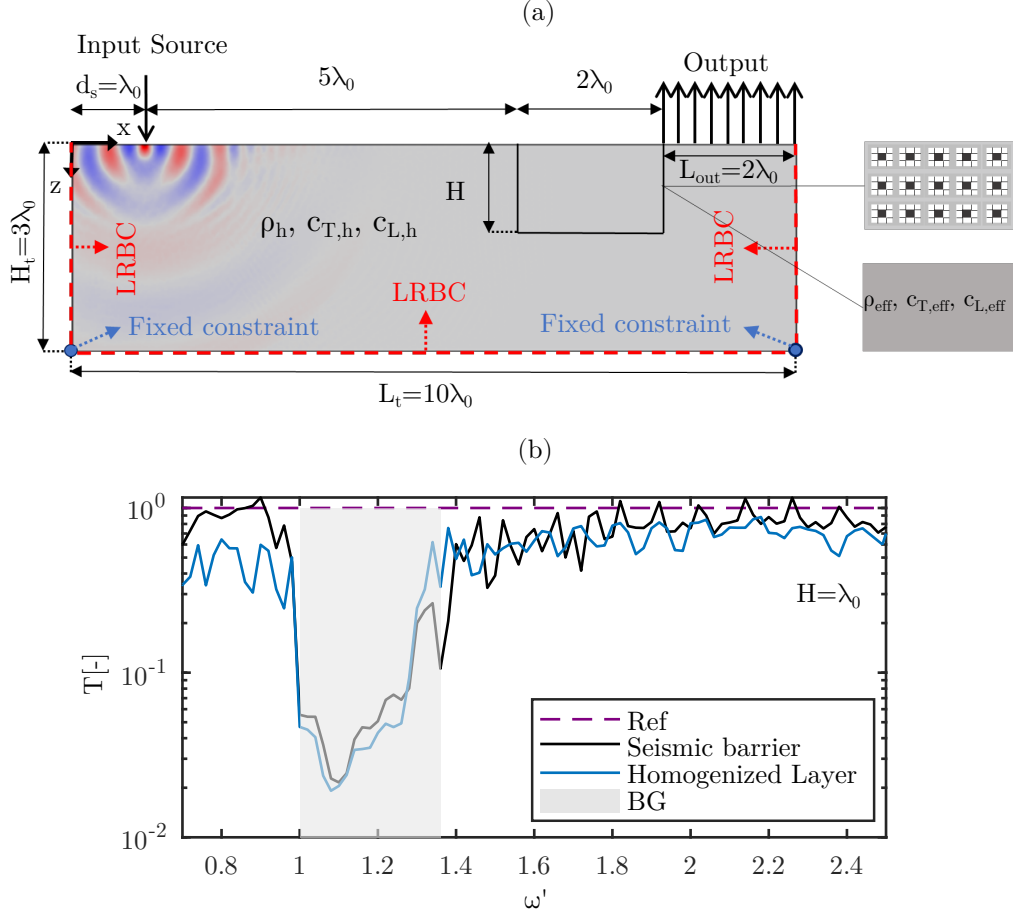


Figure 3.14: (a) Schematic of the FE model used for the calculation of the transmission coefficients. (b) Comparison of transmission coefficients $T(\omega')$ calculated for the seismic barrier and homogenized layer with an identical depth of $H = \lambda_0$.

Similarly, the attenuation efficiency of the resonant layer increases with an increase in the barrier depth. For all the cases, the attenuation peaks are located in the frequency range close to the metamaterial resonance, where the EMD assumes large negative values. Within this frequency range, a negligible part of the energy is transmitted in the form of surface solutions traveling below the resonant layer

(see Fig. 3.15a). Conversely, the transmission coefficients assume larger values outside the negative EMD region, since Rayleigh waves are attenuated only due to energy leakage. Attenuation due to leakage is indeed much less effective than attenuation due to negative EMD (see Fig. 3.16) and would require a much longer barrier to significantly reduce the surface Rayleigh wave amplitude.

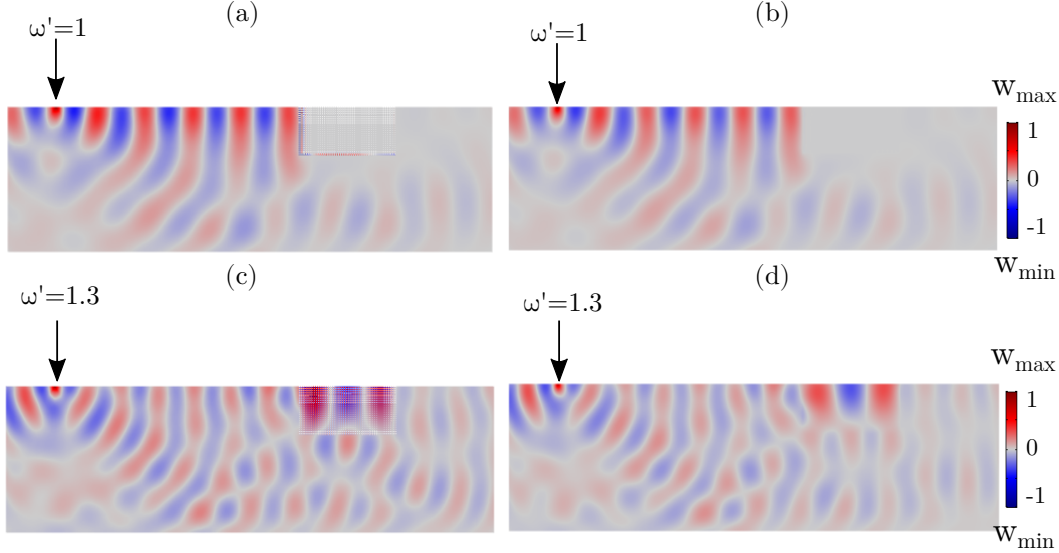


Figure 3.15: Snapshots of the vertical displacement field (z -axis) for (a) the seismic barrier and (b) its equivalent resonant layer driven by a vertical harmonic excitation at $\omega' = 1$ and for (c) the seismic barrier (d) and (d) its equivalent resonant layer is driven by a vertical harmonic excitation at $\omega' = 1.3$.

3.5 Design of a resonant metamaterial plate

Finally, we extend our study to design a small-scale prototype metamaterial plate capable to capture the dispersive properties of a resonant metamaterial discussed analytically in previous sections. To this end, we implement Bloch wave theory [18] to numerically design the metamaterial plate containing embedded resonators. We plan to exploit SLVD to measure the displacement and velocity of the plate in the table-top experimental campaign and to use PZTs as the excitation source. The fabrication of the metamaterial plate is currently under development and experimental analysis of the plate is postponed.

The design procedure commences by the realization of the phononic unit cell made of PVC material, with material properties given in Table.3.1, and will be concluded by periodically arranging them inside the pristine PVC plate. The unit

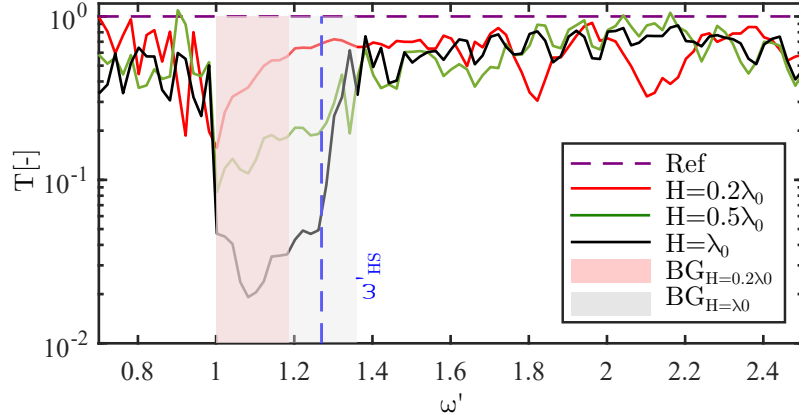


Figure 3.16: Transmission coefficients of resonant layers with different thicknesses, $H = [0.2, 0.5, 1]\lambda_0$. The red box highlights the bandgap of $H = 0.2\lambda_0$, while the shaded gray region marks the bandgap of $H = 0.5\lambda_0$ and $H = \lambda_0$. (c)

cell is designed to have a dimension of $35 \times 35 \times 10 \text{ mm}$ as shown in Fig. 3.17a, which is much smaller than the wavelength of Rayleigh wave in PVC material $a \ll \lambda_{RW,PVC}$. The resonator is realized by perforating a concentric hole inside the phononic cell and press-fitting the steel cube inside the hole as shown in Fig. 3.17b. The cubic mass has a dimension of $10 \times 10 \times 10 \text{ mm}$. The mechanical properties of steel mass are, $\rho_{stl} = 7850 \text{ kg/m}^3$, $E_{stl} = 210 \text{ GPa}$, and $\nu_{stl} = 0.3$ which are mass density, elastic modulus, and Poisson's ratio, respectively. The resonator is attached to the phononic cell via four elastic connectors, each having a dimension of $3 \times 2 \times 2 \text{ mm}$.

Material	ρ [kg/m^3]	E [GPa]	ν [-]	c_L [m/s]	c_T [m/s]	c_R [m/s]
PVC	1470	3.4	0.4	2032	910	853

Table 3.1: Mechanical parameters of the metamaterial plate.

Following the WFEM approach earlier discussed in Sec.3.3, we evaluate the dispersion curve for the phononic cell in the absence and presence of resonator as shown in Fig. 3.17c and d, respectively. As expected, the introduction of the resonator substantially modifies the dispersive properties of the phononic cell, and opens a low-frequency bandgap (see the shaded area in Fig. 3.18a) in the dispersion of bulk waves, in analogy to what we observed in the numerical simulations of 2D resonant cell reported in Fig.3.7a. The lower edge of the BG is marked by the resonant frequency of the resonator $f_{r,PVC} = 4640 \text{ Hz}$. Furthermore, the flat mode $f = 5123 \text{ Hz}$ inside the BG corresponds to the rotational motion of the resonator

with respect to the PVC casing.

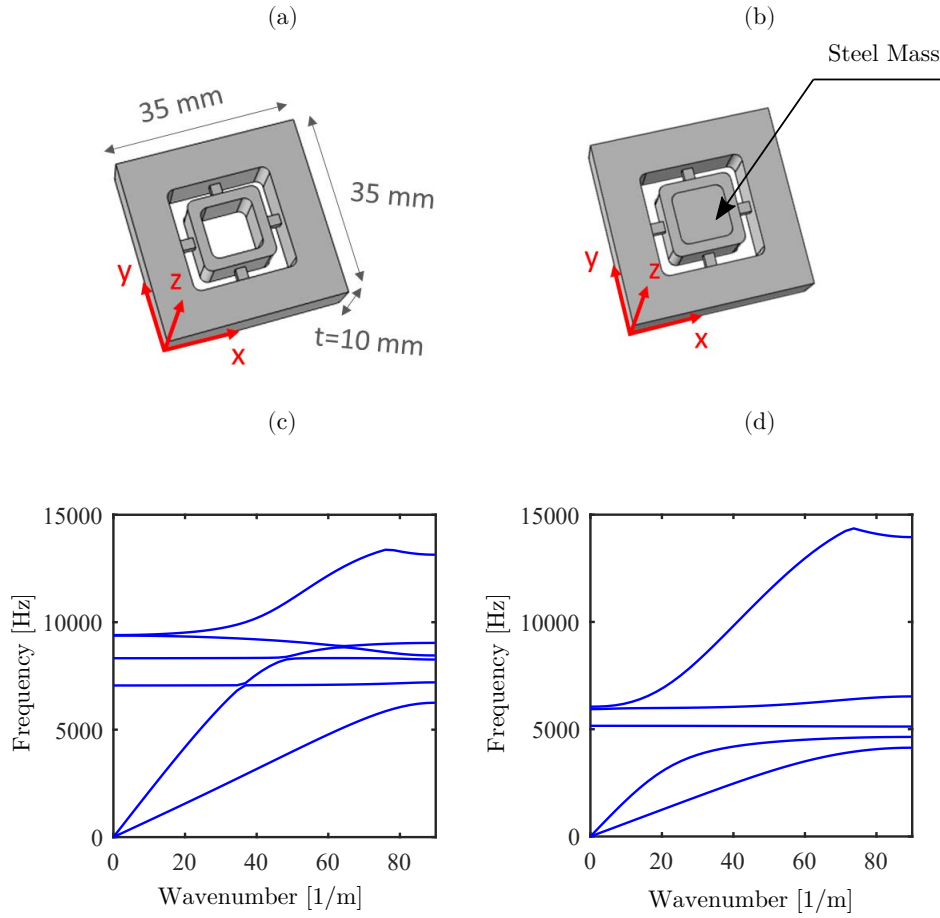


Figure 3.17: (a) Schematics of the phononic cell. (b) Schematics of the resonant unit cell. Bulk waves dispersion curves for (c) the basic and (d) resonant cells, respectively.

We compare the bulk dispersion of the resonant cell in its 3D configuration with the equivalent 2D model, to justify the simplification of exploiting the 2D model of the phononic cell with local resonance used in the analytical study of Sec. 3.2. By assuming a unitary out-of-plane dimension of 2D configuration, $K = K_r/4$ becomes the equivalent axial stiffness of each spring, where $K_r = \rho_{stl} \times A_{stl} \times 1 \times (2\pi f_r)^2$ is the total axial stiffness of elastic connectors in 3D geometry. Next, we evaluate the numerical dispersion relation of the equivalent 2D model as shown in Fig.3.19a by gray lines. Apart from the prediction of rotational mode, which we did not account for in our analytical approach, the 2D approximation proved to be sufficient to capture the fundamental dispersive features of the resonant cell, including the

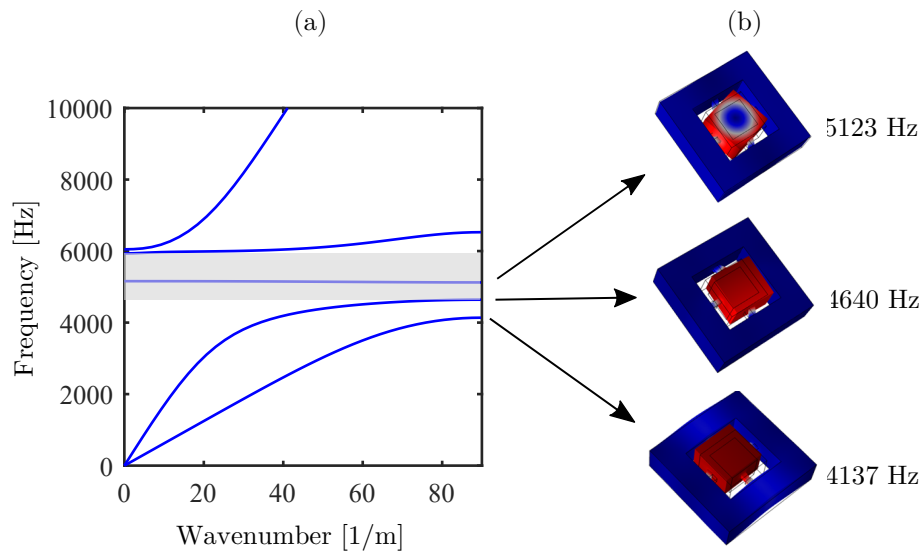


Figure 3.18: (a) A zoom in the bulk dispersion of the resonant unit cell (see Fig.3.18b). (b) Bulk modes are obtained from eigenfrequency analysis of the unit cell.

low-frequency BG and identical mode shapes (see Fig.3.19b), however, a minor shift in the frequency spectrum is observed.

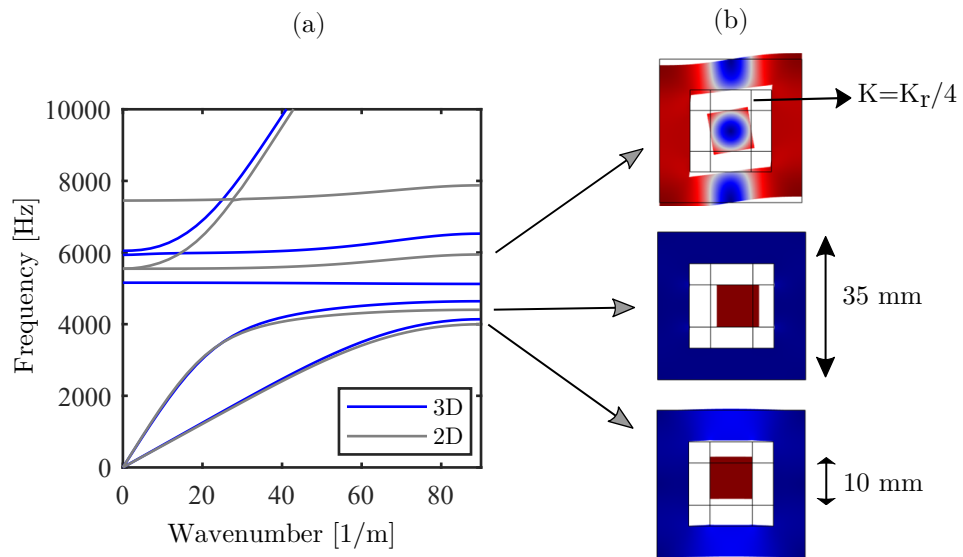


Figure 3.19: (a) Bulk dispersion of the 3D resonant unit cell vs. equivalent 2D model. (b) Bulk modes of the equivalent 2D unit cell.

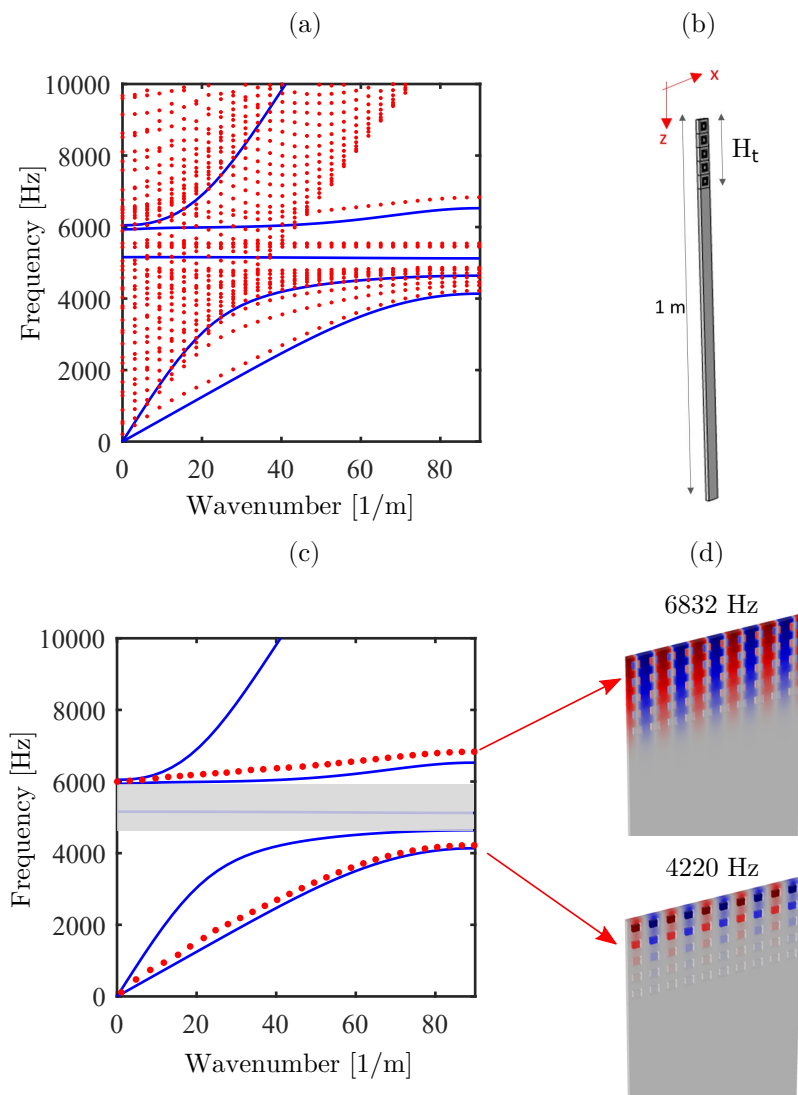


Figure 3.20: (a) Bulk dispersion of a resonant layer over a non-resonant PVC half-space over-imposed by the FE dispersion (red dots). (b) Schematics of the unit cell for FE Rayleigh mode extraction with the depth of 1 m . The resonant part includes 5 resonators with a depth of one wavelength (λ). (c) Bulk dispersion with filtered surface modes. (d) Vertical displacement wavefield for in-phase and out-of-phase branches. Highlighted gray region denotes the low-frequency surface wave bandgap.

We investigate the dispersion of Rayleigh waves in a dedicated unit cell with the length and width of 35 mm and depth of 1 m, made of 5 rows of resonators (H_t) placed atop of the PVC material layer with the total depth of 1 m, as shown in Fig.3.20b. Such a dimension is sufficiently large that the PVC layer can be considered as a homogeneous half-space. Following the WFEM approach introduced in Sec.3.3, we calculate the numerical eigenmodes (see red dots in Fig.3.20a) overimposed to bulk dispersion (solid blue lines). In order to discriminate the surface and bulk modes, we used the criterion in Eq.(3.42).

Fig.3.20c depicts the extracted Rayleigh modes using the criterion in Eq.(3.42), where the existence of two surface modes at 4220 Hz and 6832 Hz, are reported, respectively. These surface modes identify the edges of the surface bandgap frequency region. We note that Rayleigh waves become evanescent in this frequency range, in analogy to what we have seen in our numerical and analytical framework in Sec.3.3. We highlight the in-phase and out-of-phase surface modes in Fig.3.20d. Additionally, other surface modes marked inside the BG are numerical artifacts whose existence can be neglected by adjusting different threshold values of the surface mode selection criterion of Eq.(3.42), by using, for instance, $0.2H_t$ instead of $0.3H_t$.

Finally, we designed the metamaterial plate according to the numerical findings of this section, such that the designed metamaterial plate confirms the analytical framework of the study. The plate has a dimension of $1000 \times 1000 \times 10$ mm as shown schematically in Fig.3.21b and c. The top view of the 2D basic cell is also illustrated in Fig.3.21a. The metamaterial plate is fashioned by the regular repetition of the basic cells in a periodic arrangement. Two wave barriers with different thicknesses (five and three resonant cells along with the thickness) are designed to examine the variation of barrier thickness on the dispersion of surface Rayleigh waves. We expect to observe higher surface wave attenuation for the Rayleigh waves propagation across the thick barrier of embedded mechanical resonators.

3.6 Conclusions

We have investigated the propagation of Rayleigh waves in bulk and layered resonant metamaterials analytically and numerically. In more detail, a finite-depth resonant layer coupled to an elastic half-space is analyzed to reveal the dispersion of Rayleigh-like waves in such a composite medium. Then, we have shown how a metamaterial plate can be properly designed to verify the numerical and analytical findings of this research.

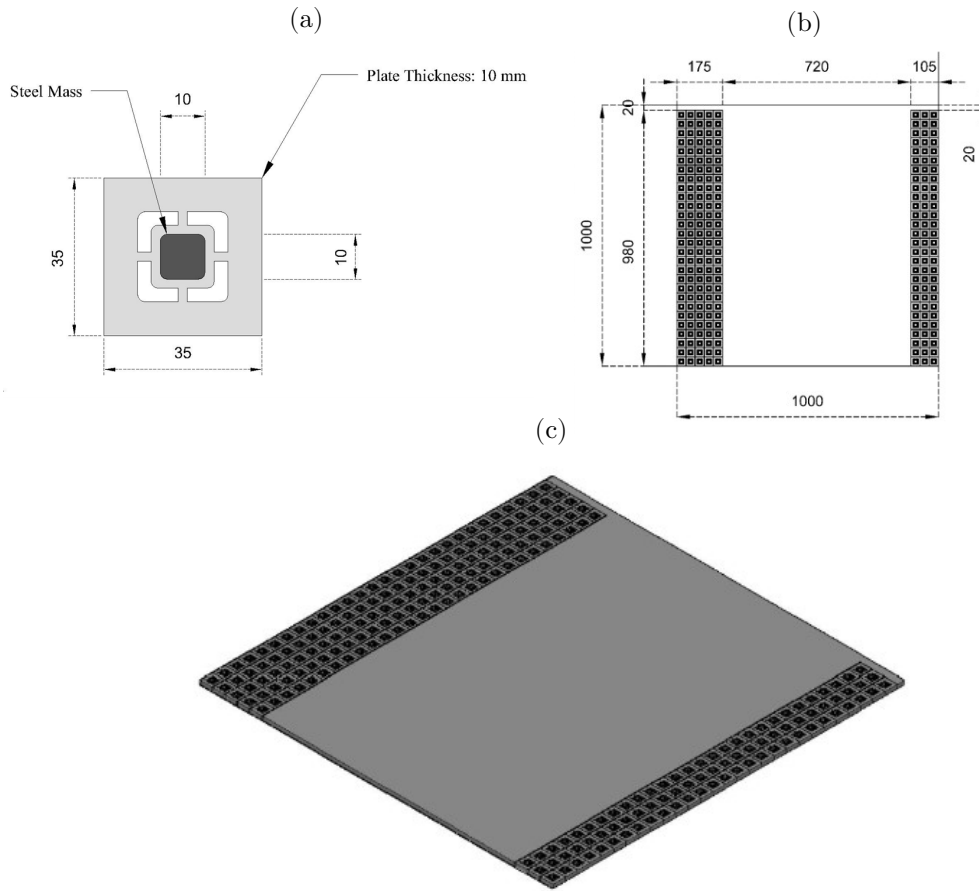


Figure 3.21: (a) 2D Schematic design of the resonant unit cell and (b) metamaterial plate. (c) 3D view of the designed metamaterial plate.

The resonant layer is characterized by randomly distributed resonators attached to the host medium via elastic connectors. We assumed an equivalent homogenized model of the resonant material exploiting a simple static homogenization approach to obtain the effective mechanical properties of composite in the low-frequency (i.e., long-wavelength) regime. By assuming such an effective description, we were able to develop an original analytical dispersion law for vertically polarized surface waves interacting with a resonant layer laid over a homogeneous half-space.

According to our model, the resonant layer supports the propagation of multiple surface modes, which get hybridized by the localized resonances of the resonators and generate a bandgap in the spectrum of Rayleigh waves.

We performed a parametric study to investigate the effect of the resonant layer depth on the size of the spectral bandgap. We showed that an increase in the resonant layer thickness leads to a larger BG, eventually broader than the one of

a full resonant half-space. The resonant half-space presents a BG width, which coincides with that of its bulk waves. The Rayleigh wave bandgap existence is ascribable to the occurrence of negative values of effective mass densities, which in turn cause an exponential decay of both bulk and Rayleigh waves.

Besides, for the layered scenario, we observed the existence of a leaky mode, i.e., a surface mode with a phase velocity higher than the shear velocity of the host material, in a narrow frequency region above the bulk BG. The frequency region where this surface mode leaks its energy into the half-space contributes to extend the BG of a layered resonant system. All these observations were confirmed via FE numerical simulations both in terms of dispersion properties and transmission coefficients.

Finally, a metamaterial plate with embedded local resonators is designed according to the analytical framework of this research. We expect that the metamaterial plate verifies the existence of the low-frequency surface wave bandgap analogous to what we have seen in the analytical and numerical study of the partially resonant waveguides. We aim to test the efficiency of the locally resonant barriers with variable thickness by measuring the transmission of Rayleigh-like waves through the designed metamaterial plate.

Overall, our work provides the analytical insight to extend current studies on locally resonant metasurfaces by accounting for the effective depth of the resonant layer. Such an analytical framework can be used to design low-frequency wave barriers viable for surface waves control across different disciplines.

3.7 Acknowledgments

Some contents and figures of the presented chapter are adopted and reproduced with permission from Ref. [167] Copyright 2021, Elsevier Ltd. The author acknowledges the DICAM department of the University of Bologna for the “Marco Polo Incentive” fellowship to support conducted research of this chapter.

3.8 Funding

This study is supported by the project “Seismology and Earthquake Engineering Research Infrastructure Alliance for Europe (SERA)”. This project has received funding from the European Union’s Horizon 2020 research and innovation programme under grant agreement No.730900.

Chapter 4

A medium-size scale resonant wave barrier

Abstract

The emergence of seismic metamaterials has led to the development of several novel isolation devices viable for seismic and ground-borne vibration control. Locally resonant barriers, also known as metabarriers, are one of those devices made of a cluster of near-surface mechanical resonators. The resonant frequency of these meter-size resonators is tuned to fall within the frequency spectrum of seismic surface waves. Resonant wave barriers can be placed around the vulnerable structures or infrastructures to attenuate the Rayleigh-induced ground motions and mitigate the risk of seismic hazards. Although the vibration attenuation capabilities of the resonant wave barriers are validated through multiple numerical studies and a few small-scale experiments, their full-scale experimental validation is still unexplored. In this chapter, we validate the attenuation performance of a medium-size scale locally resonant wave barrier operating at the frequency range between 50 to 100 Hz.

Real soil properties of the Euroseistest site (Mygdonia, Greece) are incorporated to develop the numerical simulations aimed at designing the resonant wave barrier. In specific, the dispersive properties of the bare soil, a configuration of “dead masses” placed over the soil surface, and a locally resonant metasurface, are compared numerically. The locally resonant wave barrier introduces a significant amplitude reduction of the surface Rayleigh waves in a narrow frequency range around the collective resonant frequency of the resonators. Frequency-varying barriers are designed with increasing, decreasing, and random resonant frequencies to enlarge the attenuation frequency band of Rayleigh waves. This variable-frequency design approach is obtained by tuning either the mass or stiffness of the resonators.

We expect that the medium-scale experimental tests, designed according to the presented numerical framework, will confirm the attenuation of the ground motion in the presence of the resonant wave barrier.

4.1 Introduction

Periodic foundations, locally resonant metafoundations, and locally resonant wave barriers are rationally designed metastructures able to attenuate the propagation of seismic surface waves. These novel isolation devices can represent a breakthrough for the safeguarding and the preservation of historic and critical infrastructures including hospitals, schools, and industrial plants [69, 70, 168, 71, 72, 88]. These metastructures, commonly referred to as "seismic metamaterials" in the literature [74], found their seismic isolation capabilities on the physical concepts well established in the fields of resonant metamaterials and phononic crystals (PCs) [9].

As it is explained before in Chapter 1.1.1.1, phononic crystals are periodic materials that can present large stopbands, frequency spans where the propagation of waves with wavelengths in the order of material periodicity is prohibited. For seismic-scale applications, meter-size phononic crystals made of cylindrical holes in sedimentary soil have proved the possibility of reflecting seismic waves and attenuating the ground accelerations at a frequency range around 50 Hz [74]. More recently, a similar rationale has been used to design seismic metalenses with large gradient-index able to bypass the target structure [90]. Although revolutionary in their conceptualization, engineering application of the phononic-based isolation devices at the long-wavelength (i.e., low-frequencies) nature of seismic events (< 30 Hz) requires giant structures since the wavelengths of typical seismic waves can be several meters. Besides phononic crystals, resonant metamaterials exploit an array of locally resonant inclusions embedded in a host material capable to interact with propagating waves at a sub-wavelength scale (see Chapter 1.1.1.2). Henceforth, for seismic waves characterized by long-wavelengths, resonant metamaterials allow for the design of viable isolation devices with practical dimensions from the engineering perspective. To this end, sub-wavelength structures, in the form of resonant foundations [86, 87, 82] or resonant metasurfaces [72, 88, 169, 170] have been proposed in recent years to protect buildings and infrastructures from the incoming seismic longitudinal waves or to shield them from surface Rayleigh [88, 103, 171] and Love waves [90, 92], respectively.

Although the physics behind the resonant wave barriers has been predicted analytically and verified numerically at different frequency ranges [132, 88, 172], the experimental proof of the bandgap mechanism and attenuation capabilities of the resonant metabarriers are up to now restricted to a few small-scale experimental tests [88, 102, 105, 131]. Nonetheless, preliminary numerical simulations at the

geophysical scale encourages the realization of an experimental proof of the resonant metasurface concept in the real-scale scenario.

In this chapter, we aim at making another step towards the realization of one-to-one scale resonant metabarriers for Rayleigh waves by testing the efficiency of a resonant wave barrier at a medium-size scale, within a [50 – 100] Hz frequency range, taking into account the inevitable variability in stiffness and strength of the soil and the components of the resonators. To this end, the design of an experimental campaign under development at the Euroseistest TA facility [173] is presented. The barrier is designed according to the in-situ soil properties and the available operative frequency range of the measuring equipment. An array of geophones are used to measure the soil response for surface wave excitation in the frequency range of 50 – 100 Hz for three scenarios including (I) the bare soil, (II) along with an array of dead mass over the soil, and (III) surface resonant wave barrier. The test setup is expected to confirm an attenuation of the ground motion in the presence of the resonant wave barrier considering the soil heterogeneity nature.

The chapter is organized as follows. In Sec.4.2, the soil properties, metabarrier components, and their different design configurations of the resonant barrier are discussed. In Sec.4.3, the attenuation performance of the metabarrier is analyzed through numerical dispersion analysis and finite element simulations. Besides, graded resonant metabarriers with increasing, decreasing, and random resonant frequencies are designed in Sec. Sec.4.4 to enlarge the attenuation frequency band of the proposed seismic barrier. Sec.4.5 presents the results of the preliminary experimental campaign where the case of the dead mass and bare soil condition are compared. Finally, some conclusions are drawn in Sec.4.5.

4.2 A medium-scale resonant wave barrier

4.2.1 Experimental field site description

Previous studies proved that soil properties can highly influence the amplitude decay of seismic surface waves propagating across the upper layer of the earth [174]. This is also valid for surface waves propagating across a small-scale resonant wave barrier [102], suggesting first to analyze the main characteristics of soil stratigraphy to properly design the metabarrier. We aimed at performing the test in the Euroseistest site. Euroseistest is a geotechnical test site located in the center of a tectonically active graben of Mygdonia, about 30 km to the NE of the city of Thessaloniki in northern Greece [175]. Euroseistest site was the epicenter of the Thessaloniki earthquake (1978) with a magnitude of 6.5 M_w . The soil stratification, mechanical, and dynamic properties of the Euroseistest have been carefully analyzed through

seismic - geophysical experiments, in-situ geotechnical surveys, and laboratory testings [175, 176, 173, 177]. The well-documented depth-dependent longitudinal and shear bulk wave speeds and density of the soil ($\rho = 1500 \text{ kg/m}^3$) allows for a viable design of the metabarrier (see Fig. 4.1).

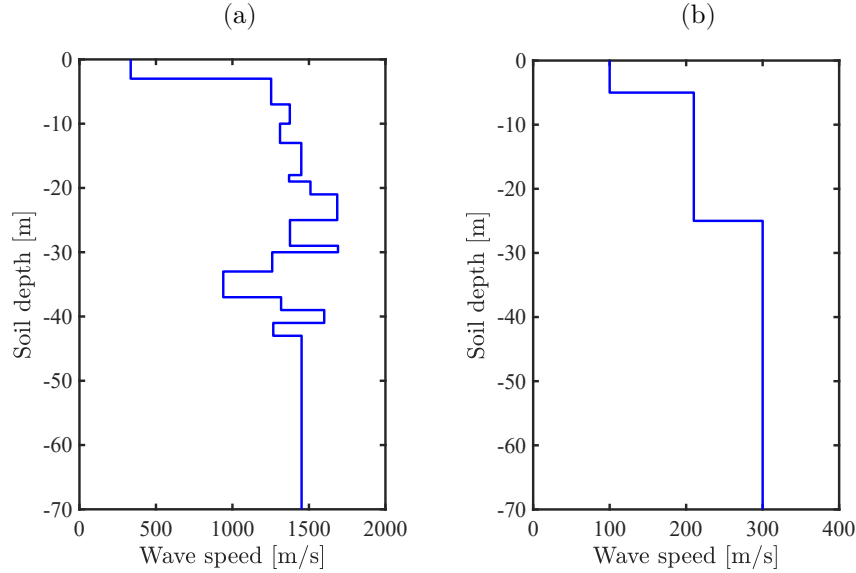


Figure 4.1: (a) Longitudinal and (b) shear waves speed profiles of the Euroseistest site. Reproduced with permission [177], Reproduced with permission, Copyright 2018, Elsevier Ltd.

4.2.2 Description of the locally resonant wave barrier

We design a locally resonant wave barrier, also referred to as metabarrier, made of an array of 5 by 10 surface resonators fashioned in a regular grid with equal spacing of 0.7 m (see the sky view in Fig. 4.2a). The dimensions of the resonators are rationally set to be small enough to guarantee that resonators and surface Rayleigh waves interact at a sub-wavelength scale. Similar configurations have been numerically studied to assess the attenuation of seismic surface waves exploiting the horizontal [71] and vertical [88] vibration modes of the resonators. In this chapter, we focus our attention on the interaction of the vertical component of Rayleigh waves with the vertical resonance f_r of the oscillators which governs the fundamental dynamics of resonant wave barriers.

In this chapter, we propose an easy-to-implement and economic design strategy for the resonators by incorporating commonly used construction materials such as steel springs and cylindrical PVC barrels filled with dry sand, as shown in Fig. 4.2b. The preliminary design of the resonator consists of a PVC barrel (with a 60

liter of volume, diameter 40 cm, and height of approximately 50 cm), two steel plates ($40 \times 40 \times 1$ cm) suspended by four to eight vertical steel springs. The base plate is anchored to the soil surface via four steel bolts. The barrels are filled with dry sand to reach an overall mass of 100 kg. Besides, a twin design configuration is proposed to study the effect of an array of “dead masses”, PVC barrels simply placed directly over the soil, as shown in Fig. 4.2c.

The resonant frequency of the mechanical oscillators is set to provide a surface wave attenuation in the frequency range interval of $[45 - 50]$ Hz, well above the operating frequency range of seismic waves (< 10 Hz). We note that by modifying the volume of the pouring sand in the barrels (or the number of steel springs and), we are able to modify the overall mass (or stiffness) of the resonators, to achieve a modular design of the locally resonant metabarrier during experiments. As an example, for total inertia of 100 kg and a tuned resonant frequency $f_r = 50$ Hz, the overall springs stiffness is $K_{tot} = 100 \cdot (2\pi f_r)^2 = 9869.6$ kN/m. Also, the proposed design approach allows the realization of the multiple-frequency wave barrier, an array of the graded resonators with increasing, decreasing, or random resonant frequencies, to enlarge the attenuation frequency band of the locally resonant wave barrier.

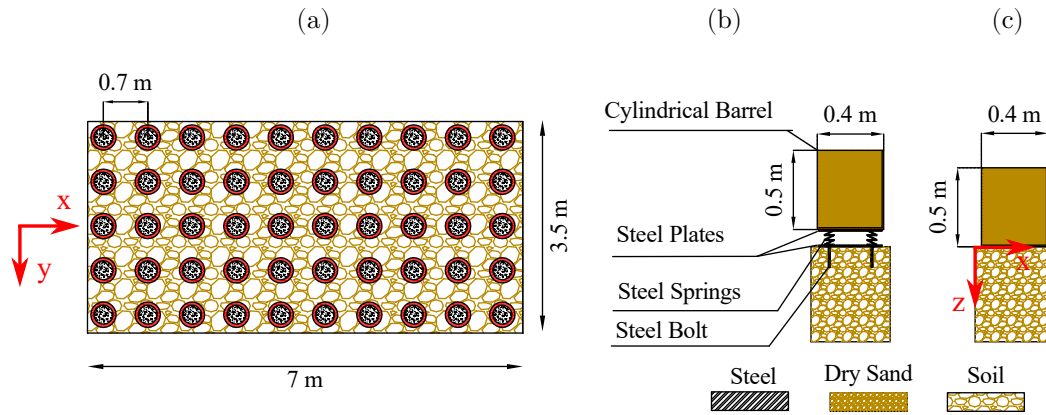


Figure 4.2: (a) An array of 5 by 10 resonators forming the metabarrier design (top view). (b) Schematics of a single resonator. (c) Schematics of a dead mass placed over the soil layer without the presence of steel plates and springs. Reproduced with permission [162], Copyright 2020, Taylor and Francis.

4.3 Finite element analysis of the resonant barrier

We develop numerical models exploiting Finite Element Analysis (FEA) to mimic and envisage the seismic isolation capability of the proposed locally resonant wave barrier. To this end, we first calculate the dispersion of surface Rayleigh waves propagating through the array of the wave barrier following WFEM approach, similar to what we have done in previous chapters for the IAR metasurface and resonant layer, respectively. Next, we incorporate the developed unit cell as the building block of the fully developed FE models to assess the Rayleigh wave attenuation performance of the proposed resonant wave barrier.

4.3.1 Numerical dispersion analysis of the barrier

In this section, we develop 2D unit cell models in Comsol Multiphysics [161] to evaluate the dynamics of Rayleigh waves traveling through the array of the locally resonant wave barrier. In specific, we numerically investigate the fundamental dynamic features of three cases: (I) a section of bare soil referred to as reference soil model (RSM), (II) a soil section containing dead mass on its surface layer (DM), and (III) a portion of soil with the resonant metabarrier (MB) attached to its surface.

For the RSM case, we consider a soil column with a height of $h = 70$ m, and the length of $w = 0.7$ m, as shown in Fig. 4.3a. The depth-dependent bulk waves velocity profiles of the soil presented in Fig. 4.1 are assigned to the model. The unit cell domain is discretized by quadratic quadrilateral elements with a maximum dimension of $d_{max} = 0.7$ m. Periodic Bloch condition is applied to the lateral edges of the FE model to obtain the surface modes of the bare soil column.

The frequency-dependent properties of the stratified bare soil (RSM) model in the frequency span of 10 – 70 Hz are shown in Fig. 4.3b, altogether with the extracted phase velocities reported in Fig. 4.3c. In opposition to the case of bare homogeneous soil where only a single surface mode can propagate [96], a plethora of surface modes can be found due to the heterogeneous nature of the soil profile in real conditions. Here, we just report the four lowest-order surface modes (e.g., M1 to M4). An approximated analytical prediction of the lowest-order surface mode in the considered heterogeneous RSM model is obtained via classical Rayleigh wave dispersion relation of a homogeneous semi-infinite media [96]:

$$\left(2 - \left(\frac{\omega}{k c_T}\right)^2\right)^2 - 4\sqrt{1 - \left(\frac{\omega}{k c_L}\right)^2}\sqrt{1 - \left(\frac{\omega}{k c_T}\right)^2} = 0 \quad (4.1)$$

where, k is the wavenumber, ω is the angular frequency, c_L , and c_T are the

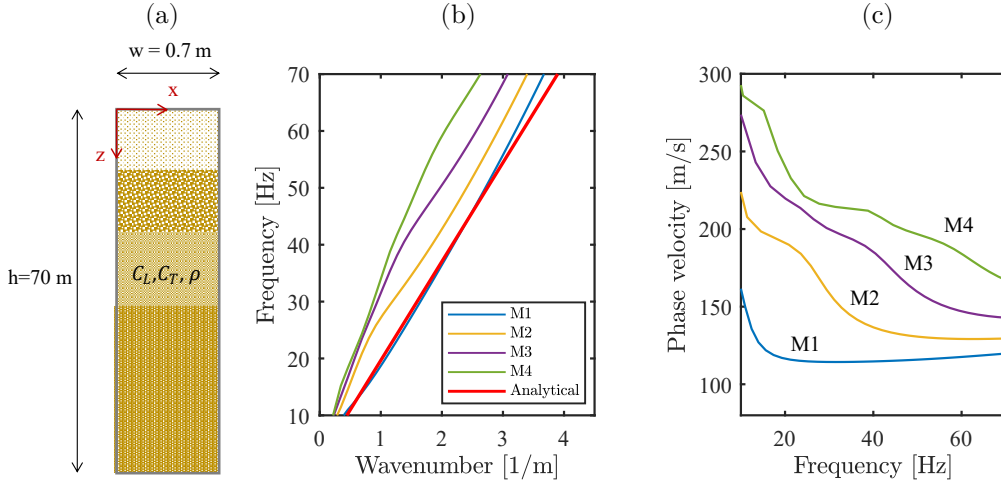


Figure 4.3: (a) Reference soil model (RSM) unit cell. Dispersion curves in terms of (b) frequency vs. wavenumber, and (c) phase velocity vs. frequency. Analytical prediction of the fundamental mode according to Eq. (1) (red line) is over-imposed to the dispersion curves. Reproduced with permission [162], Copyright 2020, Taylor and Francis.

longitudinal and shear wave velocities of the upper layer of the heterogeneous soil with 5 m of depth extracted from Fig.4.1a and b, respectively.

The dead mass (DM) configuration is modeled by introducing the dead mass to the previously developed RSM model, as shown in Fig.4.4a. The surface wave dispersion relations of the dead mass on the soil surface are displayed in Fig.4.4b. By comparing Fig.4.4c to Fig.4.3c, one can conclude that the introduction of the dead mass slightly modifies the velocity of all surface modes in the high-frequency range (e.g., $> 60 \text{ Hz}$).

Similar to the RSM case, the fundamental dispersive features of the lowest-order Rayleigh mode of DM configuration can be approximated analytically via Eq. (4.2), where the classical Rayleigh wave dispersion relation for a homogeneous semi-infinite media is modified by considering the effect of the dead masses via their exerting inertia forces at the free surface of the homogeneous waveguide [160] as:

$$\left(2 - \left(\frac{\omega}{k c_T}\right)^2\right)^2 - 4\sqrt{1 - \left(\frac{\omega}{k c_L}\right)^2} \sqrt{1 - \left(\frac{\omega}{k c_T}\right)^2} = \frac{-M \omega^4}{S \rho c_T^4 k^3} \sqrt{1 - \left(\frac{\omega}{k c_L}\right)^2} \quad (4.2)$$

In Eq. (4.2) ρ is the approximated density of the soil, $S = w \times t$ is the influence area of the dead mass, M is the mass of the DM, c_L , and c_T are the longitudinal

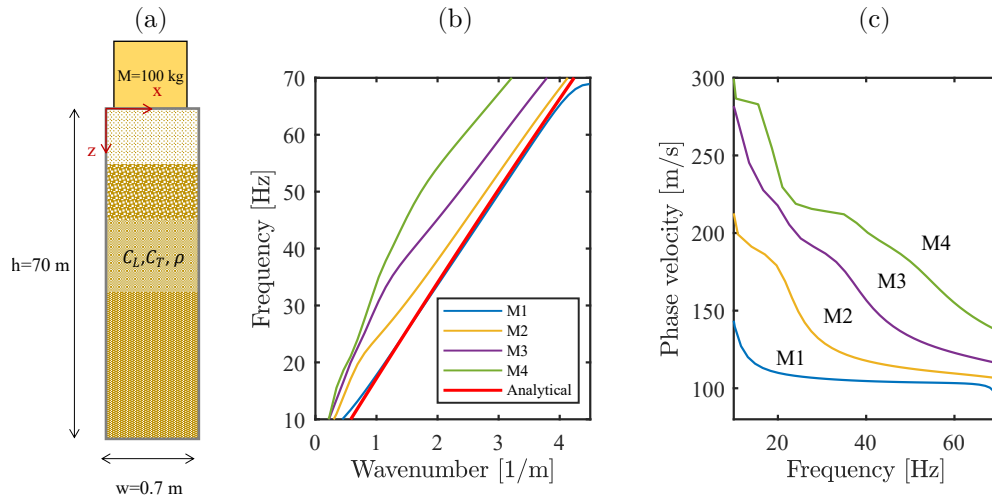


Figure 4.4: (a) Dead Mass (DM) unit cell. Dispersion curves in terms of (b) frequency vs. wavenumber, and (c) phase velocity vs. frequency. The over-imposed red curve in panel (b) has been obtained using Eq. (4.2). Reproduced with permission [162], Copyright 2020, Taylor and Francis.

and transverse wave speed of the fundamental surface mode of the bare soil at $f = 44$ Hz (extracted from Fig.4.3c), respectively. The analytical dispersion curve of Eq. (4.2) is over-imposed to the numerical FE solutions and marked as a solid red line in Fig. 4.4b. As expected, the analytical prediction of the homogeneous soil captures just the fundamental surface mode (e.g., M1) of the heterogeneous soil, emphasizing the importance of using FE models to accurately describe the dynamics of DM over the stratified soil condition.

We now focus our attention on the modeling of the resonant wave barrier based on the FE model of the dead mass. Thus, we develop the resonant barrier unit cell model by adding two steel springs, each having vertical stiffness of $K_s = K_{tot}/2$, between the soil and the mass of the DM model (see Fig. 4.5a). The frequency vs. wavenumber relation of Rayleigh-type surface waves interacting with the surface resonator is extracted from eigenfrequency analysis and plotted in Fig. 4.5b. The mechanical oscillator induces a flat dispersive branch around 44 Hz (see M1 mode in Fig. 4.5b), corresponding to the vertical motion of the resonator. The lowest-order surface mode asymptotically approaches the nominal resonant frequency of the resonators.

We note that the upper layer of the soil behaves as a very soft spring, reducing the nominal resonant frequency of the resonators attached to the soil surface, namely at 50 Hz. We compare the numerical predictions obtained via FE simulation with an analytical estimation of the Rayleigh fundamental mode interacting with the barrier via Eq. (4.3) [88] similar to what is observed for the RSM and DM cases. The

theoretical prediction is specialized to consider the interaction between the resonant barrier and surface Rayleigh waves propagating in an idealized homogeneous and isotropic soil with longitudinal and transverse wave speeds obtained from the phase velocity of the fundamental surface mode of the bare stratified soil (see Fig.4.3c) at $f = 44$ Hz:

$$\begin{aligned} & \left(\left(\frac{\omega}{\omega_r} \right)^2 - 1 \right) \left[\left(2 - \left(\frac{\omega}{k c_T} \right)^2 \right)^2 - 4 \sqrt{1 - \left(\frac{\omega}{k c_L} \right)^2} \sqrt{1 - \left(\frac{\omega}{k c_T} \right)^2} \right] \\ & = \frac{M \omega^4}{S \rho c_T^4 k^3} \sqrt{1 - \left(\frac{\omega}{k c_L} \right)^2} \end{aligned} \quad (4.3)$$

In Eq. (4.3), $\omega_r = 2\pi f_r$ is the natural frequency, and $S = 0.7m^2$ is the diameter of the PVC barrels which marks the influence area of resonators.

The solution of the analytical dispersion relation obtained from the Bisection root-finding scheme is over-imposed to the FE numerical solutions as a continuous red line in Fig. 4.5b. For an idealized homogeneous soil media, the analytical expression predicts the existence of a surface wave bandgap (gray box in Fig. 4.5b), identified by a flat dispersive branch (bottom edge) and the intersection between the fundamental surface mode with the bulk shear wave speed (upper edge) [88, 97]. Inside the frequency bandgap, Rayleigh waves cannot propagate, and they will propagate to the soil bulk in the form of shear waves [88, 98] as a result of surface-to-shear conversion. This phenomenon is not observed here in the case of layered soil medium, as it can be concluded from Fig. 4.5b, where the indicated frequency bandgap of the homogeneous soil is crossed by the higher-order surface modes [102]. Although, also for a stratified soil profile, the presence of the resonators induces the generation of a flat branch around the natural frequency of resonators $f_r = 44$ Hz. Around this frequency, a remarkable wave attenuation is expected due to the strong impedance mismatch at the interface between the bare soil and soil equipped with the sub-wavelength resonators.

In addition, we also investigate another metabarrier configuration where the resonant barrier is installed over the soil inside a trench. The trench has dimensions of 0.5×0.5 m, as it is shown in Fig. 4.6a. Excluding the presence of the trench, the soil column computational model is unchanged and the surface wave dispersion extraction follows the same procedure as the pristine soil. An additional flat branch in the low-frequency range of around 20 Hz (Fig. 4.6b) is observed for the case of embedded metabarrier in comparison to the surface resonator. The presence of this mode is linked to the resonant behavior of the lateral cantilevered soil columns. In practice, this mode is prevented by utilizing stiffer material or by employing retaining walls. Within the remaining frequency range, no significant change in the dispersion curve is found, as shown in Fig. 4.6c.

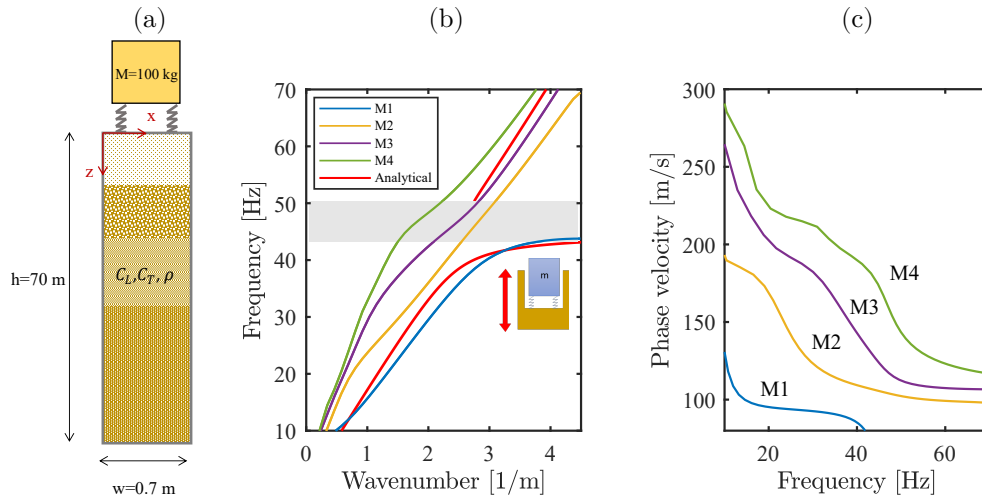


Figure 4.5: (a) Resonant wave barrier (MB) unit cell. Dispersion curves in terms of (b) frequency vs. wavenumber, and (c) phase velocity vs. frequency. The curves reported as red lines in panel (b) have been obtained by Eq. (4.3). Reproduced with permission [162], Copyright 2020, Taylor and Francis.

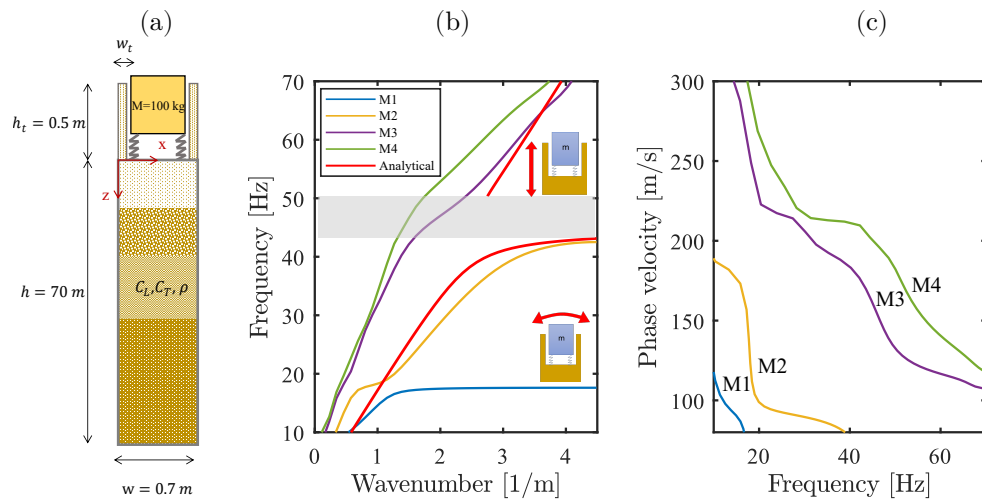


Figure 4.6: (a) Buried Metabarrier inside a trench (MB) unit cell. Dispersion curves in terms of (b) frequency vs. wavenumber, and (c) phase velocity vs. frequency. The curves reported as red lines in panel (b) have been obtained by Eq. (4.3).

Complementary to the dispersive properties, we also investigate the vertical mode profile of the soil column extracted from Bloch-FE dispersion relations at the resonance ($f_r = 44$ Hz) comparing the DM and MB cases with the bare soil reference model. The vertical displacements of 701 points equally distributed along

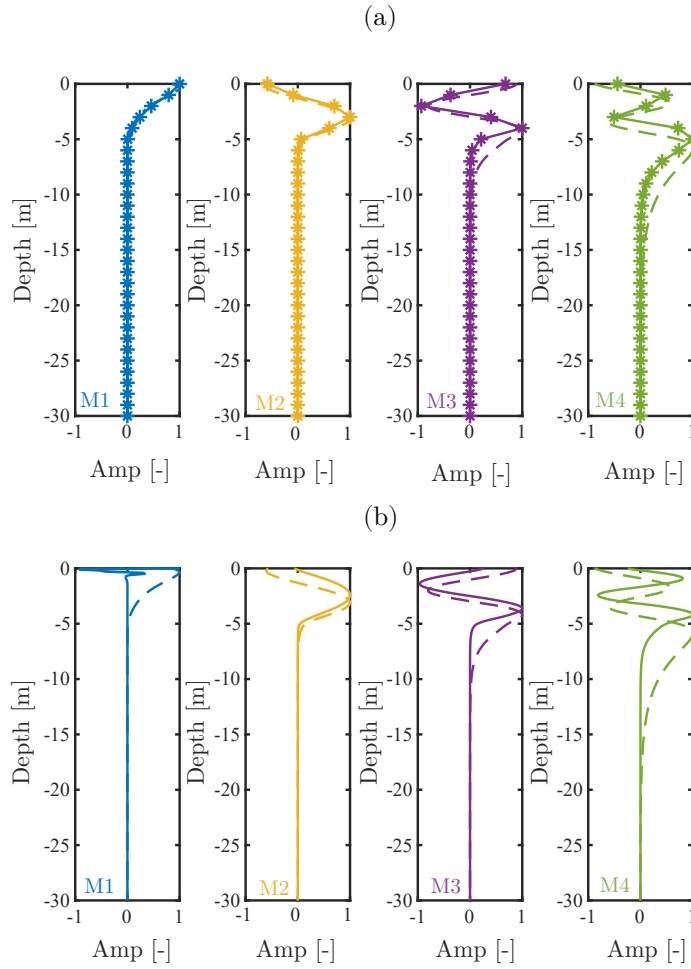


Figure 4.7: Normalized amplitude obtained from vertical nodal displacement for the dead mass (panel a) and metabarrier (panel b) cases vs. the RSM (dashed lines) at the resonant frequency of resonators ($f_r = 44 \text{ Hz}$). In the presence of metabarrier, all the surface modes are characterized by a vanishing displacement at the soil surface (continuous lines in the panel (b)).

the depth of the soil column with equal spacing of 0.1 m are extracted. The results are normalized by the maximum vertical nodal displacement of the corresponding mode and plotted versus the depth in Fig. 4.7 for M_1 , M_2 , M_3 , and M_4 surface modes, respectively. We observe that the addition of dead masses to the soil surface does not substantially modify the soil displacement (see solid lines with asterisk marker in panel a of Fig. 4.7). Conversely, the presence of the resonator significantly changes the vertical displacement of the soil. In particular, the fundamental mode gets confined to the surface due to the coupling with the resonators, while all the

higher-order modes assume almost vanishing displacement amplitude at the surface level $z = 0$ (see continuous lines in Fig. 4.7b). Hence, we expect that these modes do not contribute to the surface wavefield for the frequencies around the natural frequency of the resonator.

4.3.2 Time transient analysis

We develop 2D FE models to simulate the field experimental setup, and time history analyses are performed under the plane-strain conditions to validate the numerical predictions of the dispersion analyzes. Likewise the dispersion analysis, three full-scale numerical models are compared: (I) the reference soil model (RSM), (II) the case with an array of masses place over the soil without elastic connectors (DM), and (III) the resonant wave barrier placed over the soil surface (MB). The numerical 2D domain with a dimension of 30 m \times 70 m (see the model schematics in Fig. 4.8a) is developed to model the propagation of a surface Rayleigh wave traveling through bare soil, an array of dead mass, and an array of resonant metabarrier. Two bottom corners of the model are restrained in both x and z directions to prevent any undesired rigid motion. Besides, Low Reflective Boundary Conditions (LRBCs) are applied to the lateral and bottom boundaries of the model to minimize the wave reflection effects from the boundaries. Soil density ($\rho = 1500 \text{ kg/m}^3$) and depth-dependent bulk velocity profiles of Fig. 4.1 are assigned to the model. The field domain is discretized by the same mesh type and size used in dispersion analysis of Sec. 4.3.1 (quadratic quadrilateral elements with a maximum dimension of $d_{max} = 0.7 \text{ m}$).

Fig. 4.8b shows the schematics of the experimental setup, where the location of the source, mechanical resonators, and measuring instrumentation are reported. Eighteen geophones are incorporated for the data acquisition, half of them (geophones A to I) measure the soil response along the barrier, namely output 1, and the rest (geophones J to R) measure the soil response after the barrier, namely output 2. A Mexican hat wavelet with a central frequency of 50 Hz, able to illuminate the whole frequency range of interest (0 – 100 Hz), generates surface Rayleigh waves from the source location, with an offset of 5 m from the edge of the model. The output wavefields are evaluated as the averaged vertical nodal displacement extracted over an array of 9 points with an overall length of 6.3 m (i.e., equivalent to the array of geophones in the design of experiments) distributed along (e.g., output 1) and after the barrier (e.g., output 2).

Frequency spectra of the averaged nodal displacements for RSM, DM, and MB configurations are calculated to quantify the attenuation performance of the resonant wave barrier in terms of amplitude and frequency range. The results are presented for the array output 1 and 2 in Fig. 4.9a and b, respectively. The introduction of dead masses (DM) to the soil surface does not yield a remarkable

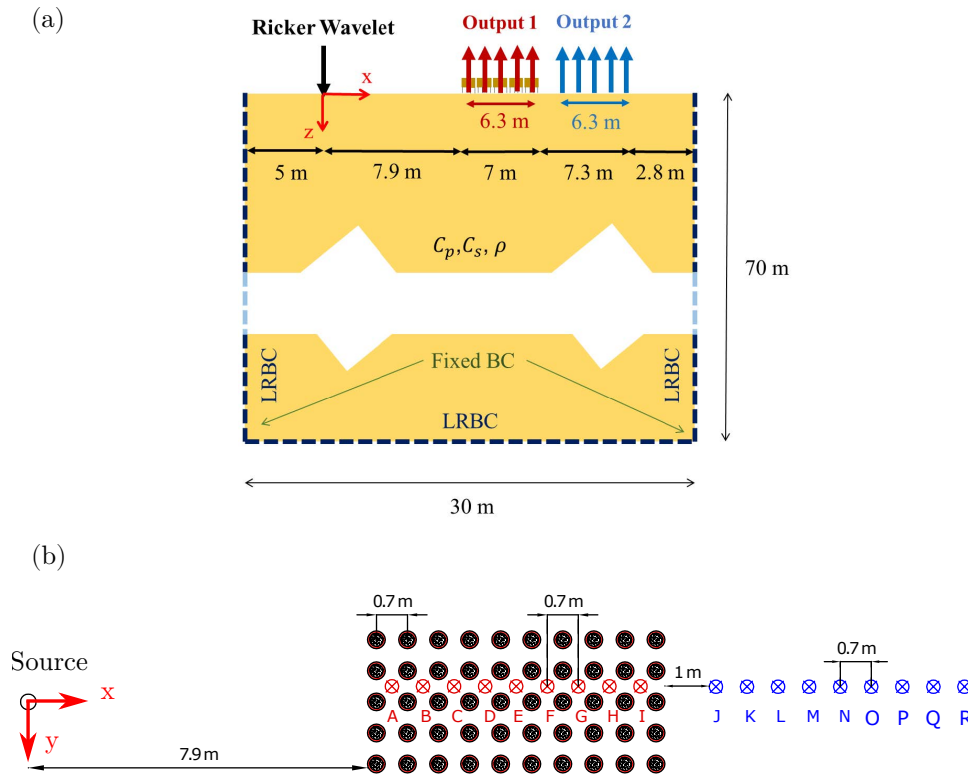


Figure 4.8: (a) Schematics of the full 2D FE model used in time history analyzes. (b) The layout of on-field experimental test setup (instrumentation, source offsets, and barrier arrangement). Reproduced with permission [162], Copyright 2020, Taylor and Francis.

reduction in the surface wave spectrum. Comparison between the outputs extracted within (output 1) and outside (output 2) the DM array evidence minor changes in the spectrum ascribable to the dispersive effects in heterogeneous soils.

Conversely, the introduction of the resonators (MB) yields a considerable, although narrow, amplitude reduction around the resonant frequency of resonators $f_r = 44$ Hz, confirming the significant impedance mismatch between the resonant wave barrier and Rayleigh waves. In the case of frequency spectra obtained from the output measured within the barrier area (output 1), the amplitude reduction is accompanied by an amplitude peak (see Fig.4.9a) for frequencies approaching the barrier resonance, as a result of the surface confinement of the fundamental surface mode, displayed in Fig.4.7b. This peak disappears in the output recorded after the barrier (Fig.4.9b).

We perform a Two-Dimensional Fast Fourier Transform (2D FFT) to derive the Rayleigh wave dispersion (frequency vs. wavenumber) from time responses

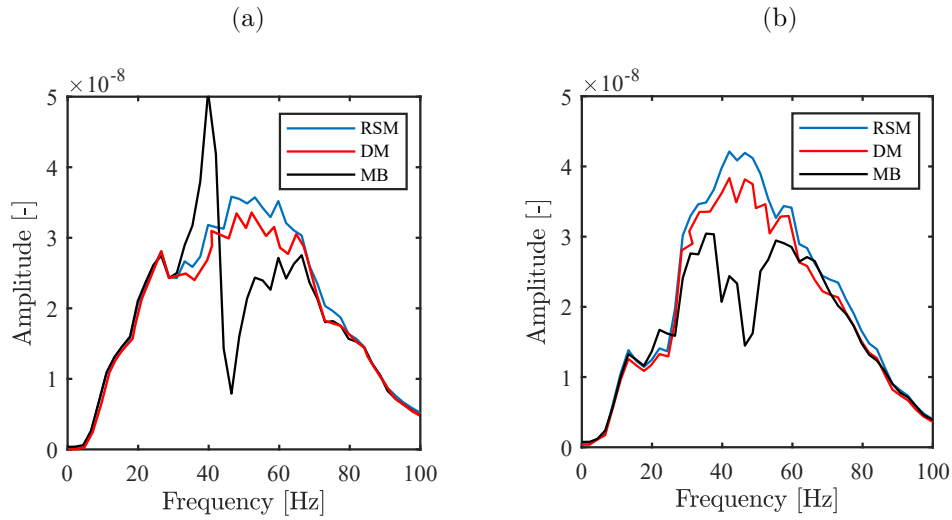


Figure 4.9: Frequency spectra of the vertical displacement fields generated by a Ricker wavelet with a central frequency of 50Hz obtained from the measurement (a) along the barrier (e.g., output 1), and (b) after the barrier (e.g., output2) for the RSM, DM, and MB configurations. Reproduced with permission [162], Copyright 2020, Taylor and Francis.

calculated along with a line across the barrier (e.g., output 1). The 2D Fourier spectrum for the DM case is displayed in Fig. 4.10a. The numerical dispersion obtained from the eigenfrequency analysis of the unit cell (see Fig. 4.4b) is overimposed to the figure. Although the resolution in the wavenumber is limited due to the finite length of the measurement array, we can observe that the spectral amplitude of the surface displacement is located along the lowest-order mode predicted by the numerical dispersion curve.

The 2D Fourier spectrum of the Rayleigh waves traveling through an array of the resonant wave barrier (metabARRIER) is shown in Fig. 4.10b. Similar to the previous case, the surface modes calculated using the unit cell eigenfrequency analysis (Fig. 4.5b), are added to the figure. The results obtained from the numerical dispersion and time history analysis are in good agreement. The flat dispersive branch around the resonance frequency, as well as the frequency bandgap (gray box in Fig. 4.10b), are well-predicted and the lack of surface wave amplitude in the frequency region above the resonance confirms that higher-order modes do not contribute to the surface wavefield around the resonance.

The vertical displacement fields of the RSM, and MB configurations, obtained from the time transient analyzes at the time instant $t = 0.3\text{ s}$, are presented in Fig. 4.11a,b, respectively. The wavefield map confirms a surface displacement reduction for the metabARRIER case, ascribable to the dispersive nature of Rayleigh-type waves

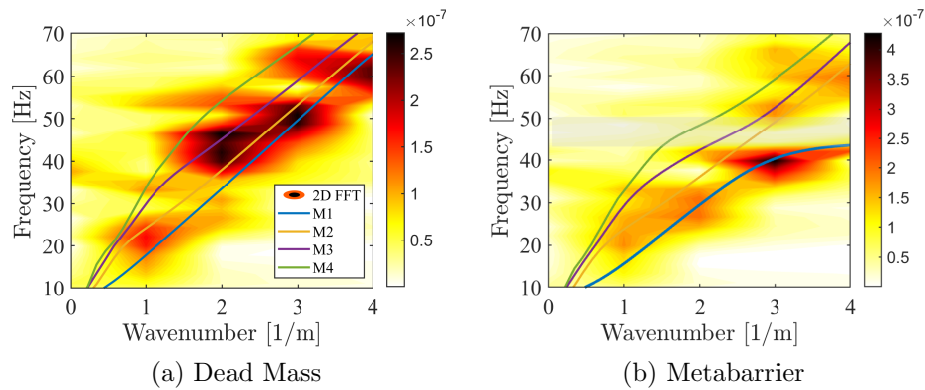


Figure 4.10: Dispersion spectra obtained from 2D FFTs of the time-domain surface displacements for the DM and MB cases (output 1). The dispersion curves predicted by the WFEM models in the Sec.4.3.1 are over-imposed as continuous lines. The gray box denotes the Rayleigh-induced bandgap. Reproduced with permission [162], Copyright 2020, Taylor and Francis.

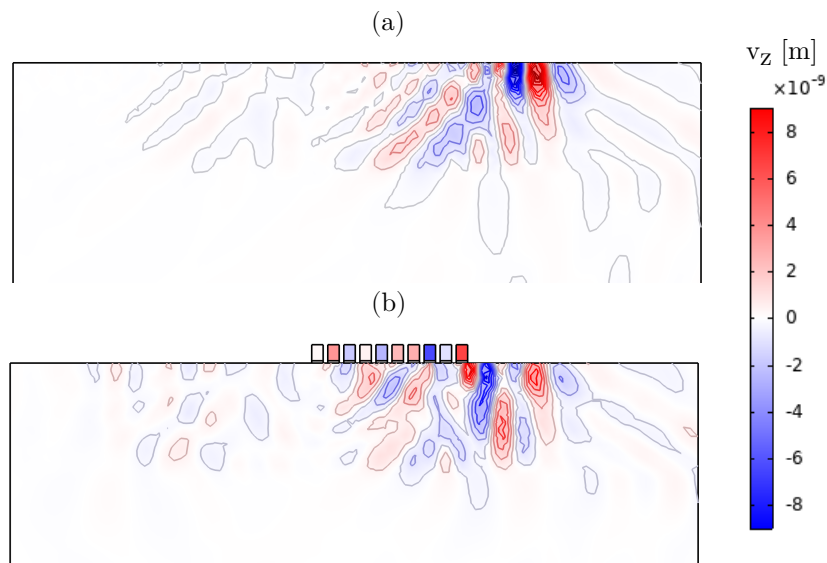


Figure 4.11: The vertical displacement field of (a) RSM, and (b) metabarrier (MB) configurations. Gray box denotes the bandgap region. Reproduced with permission [162], Copyright 2020, Taylor and Francis.

propagation through the array of near-surface resonators and to the modified displacement profile, which gets confined below the surface.

4.4 Frequency-variable resonant wave barrier

We take advantage of the modular design of the resonant wave barrier designed in this chapter to propose frequency-variable barriers, e.g., locally resonant wave barriers with graded resonant frequencies, for broadband attenuation purposes. The approach follows the idea of the “rainbow trapping”, originally presented in Ref. [100] to discuss the dynamics of Rayleigh waves interacting with an array of elastic beams with increasing or decreasing frequencies.

The multiple-frequency resonant barrier is made by a regular arrangement of equally-distributed resonators with increasing, decreasing, or random resonant frequencies. The resonant frequencies of the resonators can be tailored by varying either the mass (e.g., pouring different volumes of dry sand into the PVC barrels) or the vertical stiffness (e.g., changing the number of steel springs) of the resonator. In the first case, by linearly increasing the mass of the resonators from 55 to 100 kg and keeping the number of springs constant ($K_{tot} = 9869.6 \text{ kN/m}$), we reduce the natural frequency of resonators with a factor $1/\sqrt{d}$, where d is the resonator location along with the array, as shown in Fig.4.12a. This approach yields a wave barriers with decreasing mass for a constant stiffness, to obtain a barrier with increasing frequency (Fig.4.12b). In both cases, the outputs are measured within (output 1) and after the barrier (output 2) exploiting 9 geophones (see Fig.4.8a).

On one hand, we remind that the interaction of surface Rayleigh waves and a graded wave barrier with decreasing frequency (the so-called classical metawedge [100]) is able to open a wide bandgap for a homogeneous and isotropic soil half-space, where the Rayleigh waves are confined and back-reflected by an array of the mechanical oscillators. In this study where the soil modeled is more complicated and soil stratification plays a significant role, the overall behavior of the graded resonant wave is similar. The wave motion is confined and amplified along the wave barrier, as evidenced by the wider amplitude peak shown in Fig.4.12c. After the resonant wave barrier array (see Fig.4.12e), a significant attenuation is observed as a result of the wave reflection effect.

On the other hand, for an increasing frequency wave barrier overlaying a homogeneous soil (i.e., the inverse metawedge [100]), the amplitude reduction is ascribable to the surface-to-shear wave conversion, with no displacement confinement along the barrier. In our heterogeneous soil scenario, although the surface-to-shear wave conversion is partially prevented by the higher-order surface modes, the behavior of the barrier is similar. The surface wave energy is attenuated inside the barrier in a broader frequency range of approximately 40 – 70 Hz, and no significant amplifications are observed (see Fig.4.12d). The amplitude in the attenuation frequency zone increases gradually as the resonant frequency increases. After the barrier (see Fig.4.12f), the attenuation performance remains similar, although a sharper peak attenuation is observed around 55 Hz.

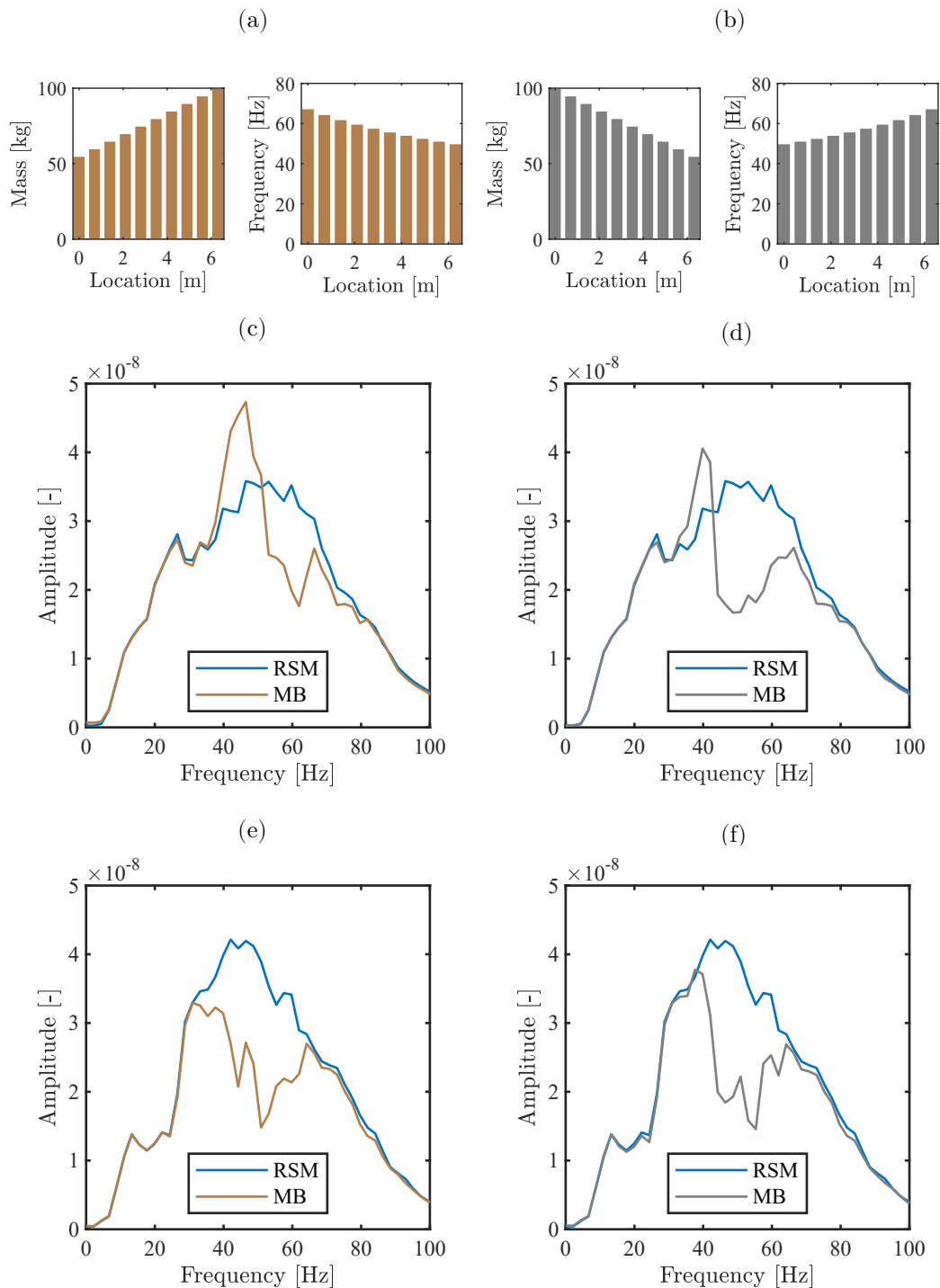


Figure 4.12: Mass distribution and the resonant frequency of the graded resonant barrier with increasing mass (a), and decreasing mass (b). Frequency spectra calculated along the graded barrier (output 1) with increasing mass (c), and decreasing mass (d) for a constant stiffness of the resonators. Frequency spectra after the graded barrier (output 2) with increasing mass (e), and decreasing mass (f) for a constant stiffness of the resonators ($K_{tot} = 9869.6 \text{ kN/m}$). Reproduced with permission [162], Copyright 2020, Taylor and Francis.

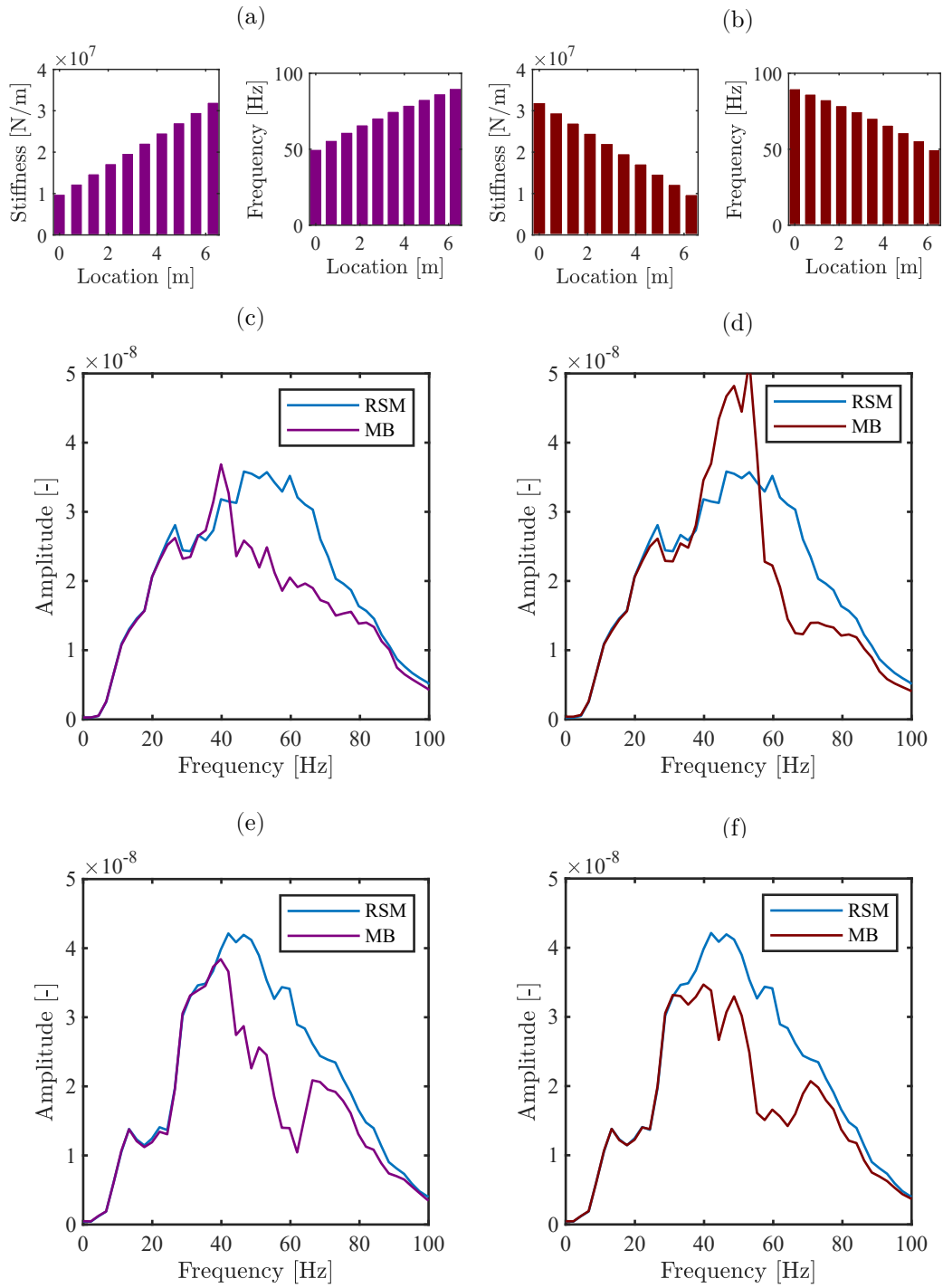


Figure 4.13: Stiffness and the resonant frequency of the graded resonant barrier with increasing stiffness (a), and decreasing stiffness (b). Frequency spectra calculated along the graded barrier (output 1) with increasing vertical stiffness (c), and decreasing vertical stiffness (d) for a constant mass of the resonators. Frequency spectra are calculated after the graded barrier (output 2) with increasing vertical stiffness (e) and decreasing vertical stiffness (f) for a constant mass of the resonators ($M = 100$ kg). Reproduced with permission [162], Copyright 2020, Taylor and Francis.

Similar results can be achieved by designing graded resonant wave barriers with constant mass (e.g., $M = 100$ kg) and varying stiffness of increasing or decreasing resonant frequencies, as shown in Fig.4.13a and b, respectively. For instance, we can design a resonant wave barrier with an increasing number of springs per resonator, starting with a resonator with 4 springs and reaching up to 13 springs for the last resonator of the barrier. The increasing frequency barrier (with increasing stiffness) shows a dynamic behavior similar to the case with decreasing mass, as shown in Fig. 4.13c and e, for attenuation measurements along and after barrier, respectively. Conversely, by mirroring the distribution of the resonator along with the array, so to obtain a barrier with decreasing frequency, a wider range of frequency where surface waves are confined and amplified within (Fig. 4.13d) and after the barrier (Fig. 4.13e) is obtained. The broader frequency range covered by the barrier allows us to obtain a wider frequency range of attenuation.

Given the fact that during the experiments, some factors may lead to an unexpected variation of the nominal resonant frequency of the resonators, we propose the design of a random frequency varying barrier. The source of error during the experiments can be the variation of resonator mass, production of steel springs with different length and axial stiffness, variation in the dimensions of the steel plates, rocking motion of the resonators during the excitation, horizontal and vertical motion of the steel bolts inside the soil, etc.

We investigate the attenuation performance of random-frequency barriers, considering three cases whose masses are randomly distributed between 55 and 100 kg while their stiffness is kept constant, as shown in Fig.4.14a, b, and c. The attenuation frequency range of the random barriers shifts to higher frequencies with higher amplitude in comparison with the resonant frequency of the single-frequency barrier reported in Fig. 4.9b.

4.5 Preliminary Experimental Test: Dead Mass over the soil surface

The experimental tests were planned to be carried out in two different phases (P1) and (P2). The first phase (P1) has been executed in the Euroseistest facility and comprised two sets of tests:

1. T_0 : Ambient noise, vibration testing (pneumatic vibrators), and impact load (Sledgehammer loading) on the soil in pristine conditions. This primary set of tests aimed at defining a baseline of records with different vibrating sources, various source offsets, defining the operational frequency range of the sources, the amplitude of the records within the test field, and the dispersive features of the records (see Fig. 4.15a).

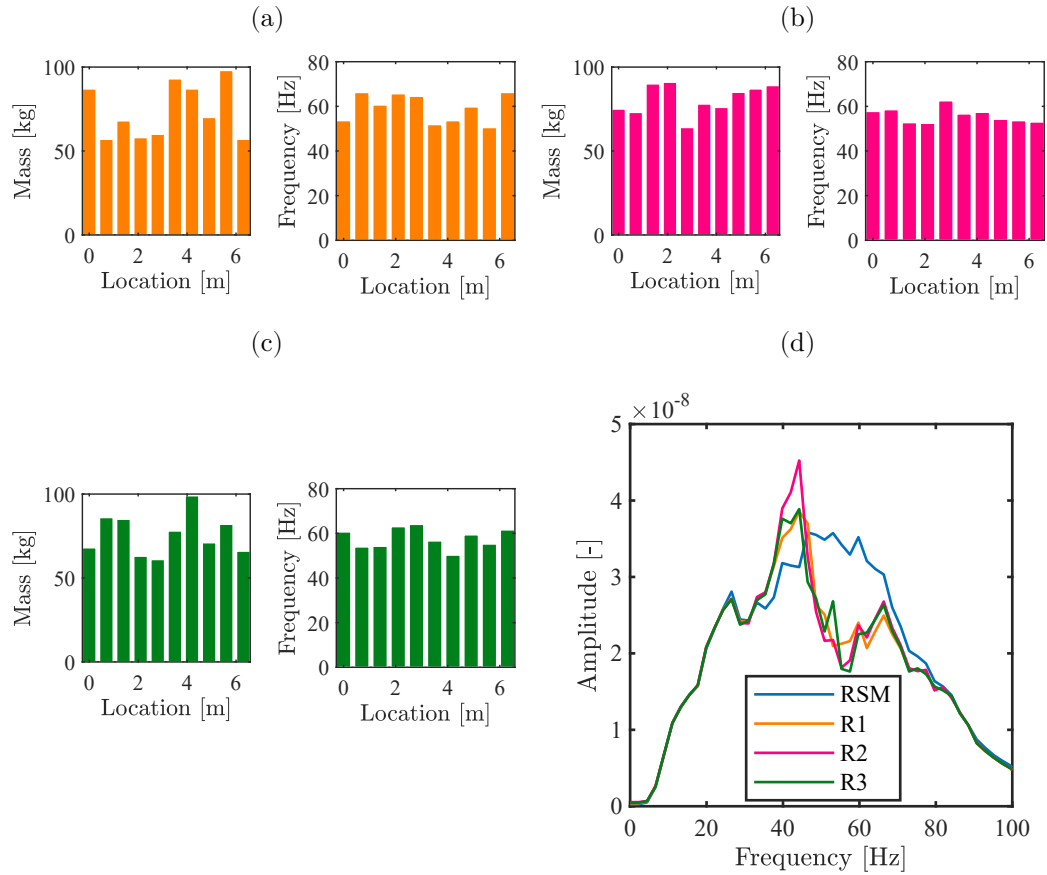


Figure 4.14: Mass and resonant frequency of three random resonant barriers (a), (b), and (c), respectively. (d) Comparison between the frequency spectra (output 1) of the three random cases.

2. T_1 : Ambient noise, vibration testing, and impact load on the soil equipped with an array of 5×10 ($3.5 \text{ m} \times 7 \text{ m}$) masses placed directly over the soil surface, e.g., dead mass (DM) configuration, in compliance with the numerical models (see Fig. 4.15b).

The second phase of the experiments is delayed due to the spread of the SARS-CoV-2 pandemic; therefore, we just report the results of the P1 in what follows.

4.5.1 Instrumentation setup

The soil organic horizon of the test site was removed, and the soil surface was compacted to prepare the pristine condition suitable for the experiments. The

measuring instruments were placed over the soil surface according to the designed test setup earlier reported in Fig. 4.2a. The test field equipped with the sensor placement shown in Fig. 4.15a is set to execute the line measurement from geophones A to N for the T_0 setting (see the schematics of Fig. 4.8b). A sequence of multiple tests was run to measure the ambient noise and soil response for different source types in different positions. Fifty PVC barrels with a volume of 60 liters, filled with dry sand with an approximate weight of 981 N were used to realize the dead mass (see Fig. 4.15b) analogous to the numerical dispersion discussed in Fig. 4.4b. The array of dead masses over soil was arranged following the dimensions and specifications of the designed configuration shown in Fig. 4.2b.



Figure 4.15: (a) On-field line measurement setup across DM length on soil pristine (T_0 setting) (b) Dead mass configuration (barrel with 100 kg of mass) atop of soil pristine (T_1 setting).

4.5.2 Source characterization

Three types of loading sources (Linear Pneumatic Vibrator NTP-25, Rotary Pneumatic Vibrator VT-24, and Hammer impact) were used to generate surface waves. We fairly analyzed the characteristics of each source first, considering the limitations of the sensor nodes discussed above, and then compared the recorded results for the dead mass case (T_1) to the soil (T_0). To this end, we perform Fast Fourier Transform (FFT) of the signals recorded from the specific geophone of choice, at this stage we select accelerometer at location H (see Fig.4.2a) inside the DM array, to describe the frequency spectra of the source. The sampling frequency is set to 200 Hz, and a high-pass filter is used to allow the high-frequency signals to pass from the source to the sensor.

The frequency content of both linear and rotary pneumatic vibrators (with different input pressures) falls within two separated frequency windows; hence, the application of pneumatic vibrators are not adequate for the assessment of the

resonant wave barrier dynamics, which is expected within the frequency range from 40 to 70 Hz. Therefore, we just report the outcomes of the hammer impact loading excited the test field from source location 2, as shown in Fig.4.16a.

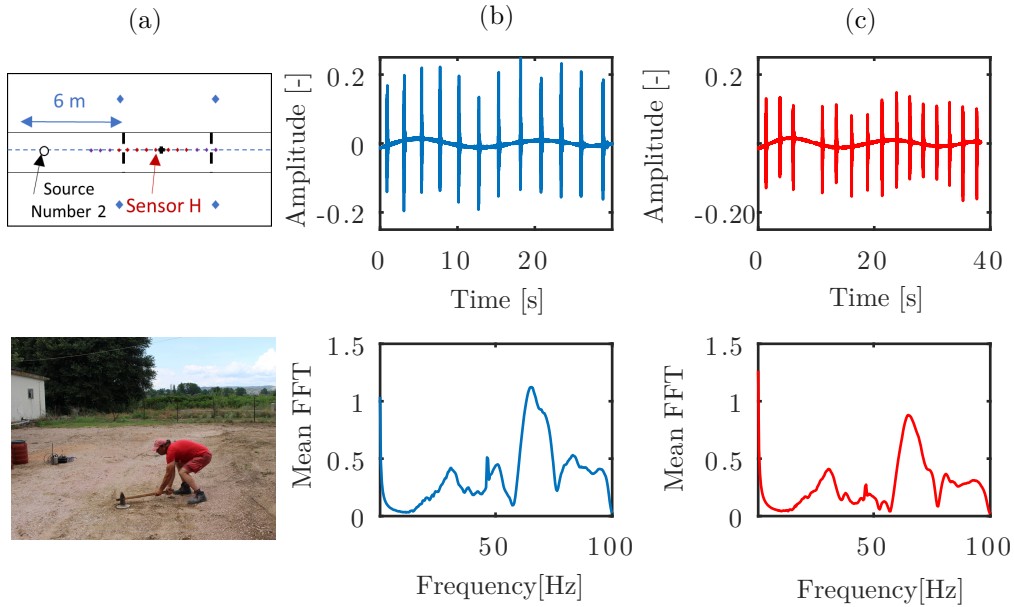


Figure 4.16: Sledgehammer impact. (a) The source excites the far-field from position 2, and sensor H (accelerometer) measures the response. (b) Signal time trace and mean of the FFTs of the recorded signal for the free field and (c) dead mass conditions.

The sledgehammer was used to generate the surface waves when the operator hit a steel disk. In general, between 10 to 15 strikes were recorded for T_0 and T_1 in different test configurations. We characterize the frequency spectra of the hammer input by chopping the received signal for each impact into time intervals of 0.5 sec. We then perform the FFTs of the corresponding time traces of each strike and eventually calculate the mean spectrum, as depicted in Fig. 4.16b and c for soil and dead mass, respectively. The frequency content of the hammer impact obtained from a series of strikes spreads in the whole frequency range of interest from 0 to 100 Hz, which makes it suitable to investigate the signal attenuation introduced by the resonators in metabarrier (MB) configuration. We remark that the location (inside or outside of DM zone) and type (seismometer or accelerometer) of the geophone are highly influencing the recorded response of the DM configuration.

4.5.3 Experimental Results

We compare the response of the soil in the presence and absence of the dead masses, both numerically and experimentally. We plot the mean FFTs of soil and dead mass reported in Fig.4.16b and c together in Fig. 4.17a. Amplitude reduction of the surface waves observed in the low-frequency regime is negligible. While, in the high-frequency range, the amplitude reduction becomes more significant, where the wavelength becomes comparable to the influence area of the masses.

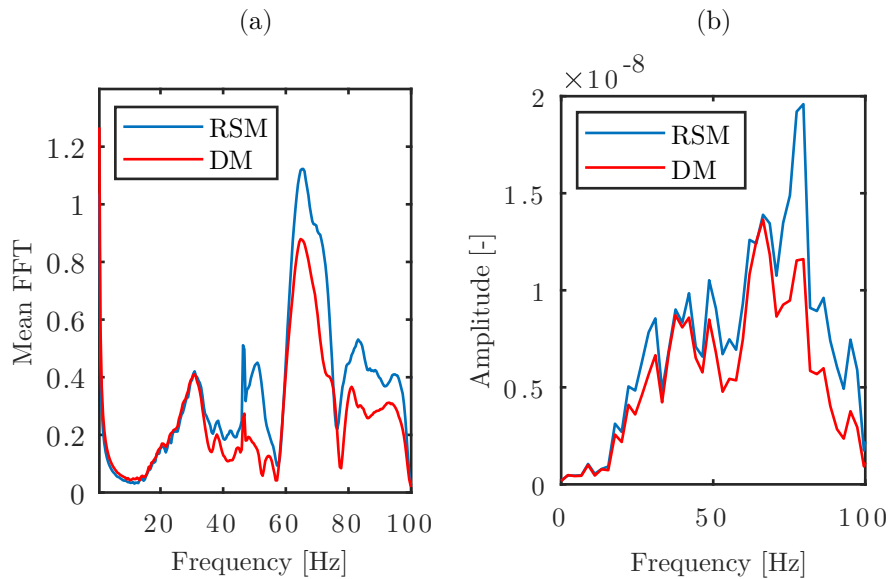


Figure 4.17: Comparison between soil (RSM) and dead mass (DM) from (a) experimental tests, and (b) numerical simulations.

We adopt the numerical model used in Fig.4.9a and move the location of the input source to location 2 (6 m apart from the dead mass area) to correctly replicate the test setup scenario. The hammer impulse recorded by geophone H from the free field condition is used as the benchmark input source (see Fig.4.16b). A total number of 12 sub-signals extracted for each strike are applied to the model. The output field is measured separately for each strike according to what we have done in Sec.4.3.2 for the Ricker excitation. The mean of the 12 output frequency spectra is then calculated and displayed for the DM and RSM, as shown in Fig.4.17b. The amplitude reduction in the frequency spectra of the DM resulted from the numerical simulation, which confirms the experimental findings.

4.6 Conclusions

The resonant wave barrier consists of an array of locally resonant oscillators which can be installed close to the soil surface around the target structure or infrastructure to be protected from incident surface Rayleigh waves. Since their installation does not require any intervention on the existing structure, the resonant wave barrier can be represented as an innovative approach for seismic retrofitting of vulnerable structures and infrastructures of prior importance for public safety (e.g., schools, hospitals, power plants, etc.). In this chapter, the seismic wave attenuation capability of a medium-scale resonant wave barrier placed on top of the heterogeneous soil is evaluated numerically, to provide the required guidelines of an experimental campaign aimed at assessing the isolation performance of the seismic barrier in the real geophysical scenario.

The numerical investigations of this chapter showed that while a deep trench inside the soil provides seismic attenuation due to scattering at frequencies related to the depth of the trench, the resonant wave barrier exploits the local resonance mechanism to attenuate the seismic motion at frequency ranges related to the natural frequency of resonators. We have shown that a resonant barrier of periodically distributed resonators placed directly over the soil surface provides attenuation performance identical to that of the barrier inside the trench while it can simplify the test realization and minimize its costs.

Some numerical simulations were performed on a finite-length resonant barrier according to the WFEM approach, to measure the attenuation of Rayleigh-type surface waves traveling within and after the resonant barrier. Besides the resonant barrier, an array of dead masses directly placed over the soil surface is evaluated as a case study, and the numerical results of these two cases were compared to the reference soil model (RSM). Besides, the graded resonant barriers with increasing, decreasing, and random resonant frequencies along with the array of resonators are designed for large-bandwidth attenuation of Rayleigh waves.

Complimentary to the numerical simulations, a preliminary experimental campaign (P1) is designed to test the resonant wave barrier in the Euroseistest site (Mygdonia, Greece). In particular, dead mass (DM) configuration (metabarrier without elastic connectors) is compared to the soil in pristine condition. The experimental outcomes showed a marked amplitude reduction of the soil response in the presence of dead masses analogous to what we have observed in the numerical predictions. Further experimental tests (P2) can be designed to examine the isolation performance of resonant wave barrier by adding steel bolts, plates, and springs to the dead mass according to the design strategy of the resonant barrier, allowing the oscillation of the tuned-resonator. In this scenario, The MASW technique can be incorporated to measure the soil response. The numerical and experimental outcomes of this research can provide a better understanding of the dynamics of

locally resonant devices for surface wave manipulation and allow the design and fabrication of full-scale resonant barriers in the future.

4.7 Acknowledgments

The author would like to remark that partial contents and figures of this chapter are adopted and reproduced from Ref. [162] with Copyright 2020, Taylor and Francis.

4.8 Funding

This study is supported by the project "Seismology and Earthquake Engineering Research Infrastructure Alliance for Europe (SERA)". This project has received funding from the European Union's Horizon 2020 research and innovation programme under grant agreement No.730900.

Chapter 5

Conclusions, ongoing research activities, and future outlook

The presented dissertation addresses the design and analysis of locally resonant metamaterials developed for the manipulation of surface Rayleigh waves across different frequency ranges. Specific considerations are devoted to the development of resonant wave barriers capable to hinder the propagation of seismic surface waves with the application of safeguarding vulnerable structures/infrastructures. To this purpose, a detailed literature review of periodic and resonant elastic metamaterials is provided in Chapter. 1. Chapter. 2 conceptualizes the design of an enhanced locally resonant metasurface to overcome the limits of classical mass-spring metasurfaces. Chapter. 3 proposes a rigorous analytical approach to study the dispersive properties of a thick resonant layer of resonant metamaterials, and design a deep seismic resonant barrier buried inside the soil surface. Finally, Chapter 4 presents the numerical design of a medium-size scale resonant wave barrier for the attenuation of seismic surface waves. Although detailed conclusions are provided at the end of each chapter, here we summarize the main findings of the dissertation and describe the current research activities followed by an overview of the possible future research outlooks.

5.1 Conclusions of Chapter II

Chapter. 2 proposed an advanced class of locally resonant metasurfaces, namely Inertial Amplified Resonator (IAR) metasurface. IAR metasurface is rationally designed to enhance the overall dynamic properties of the elastic metasurfaces to control the propagation of surface waves. The main conclusions of the chapter are listed as follows:

1. The natural frequency of the IAR metasurface can be controlled via two

design parameters, e.g., the internal angle of the rhomboid geometry and the mass distribution ratio between the mass-stiffness system and additionally embedded inerters.

2. The dynamic interaction between the IAR metasurfaces arranged over an elastic half-space and Rayleigh-type surface waves was described through a closed-form dispersion law (i.e., frequency vs. wavenumber relation) exploiting the effective medium approach. The dispersion relation revealed three interesting key frequency regions, e.g., resonance, anti-resonance, and zero-stress frequency, which can be controlled via design parameters. The coupling between the metasurface and propagating surface waves has led to the generation of a low-frequency bandgap. By distributing the total inertia among mass-spring and embedded inertial systems, IAR metasurface has been capable to open wider bandgaps in comparison with the classical metasurfaces. Numerical simulations were performed to confirm the dispersive features of the advanced metasurfaces predicted by analytical dispersion laws.
3. Surface wave propagation is prohibited inside the bandgap region. Nevertheless, the advanced metasurface becomes transparent to the Rayleigh waves at zero-stress frequency. The strong impedance mismatch between the metasurface and Rayleigh waves was observed in the high-frequency regime, where the advanced metasurface presented a similar behavior analogous to dead masses placed over the free surface of an elastic half-space.
4. Graded resonant metasurfaces were designed to enlarge the resonance-induced stopband by modifying one of the design parameters (e.g., by keeping the inertia constant and varying the internal angle of the resonators).
5. A seismic wave barrier was proposed based on the tunable and dispersive characteristics of the IAR metasurface. The resonant wave barrier showed the capability of steering the seismic wave trajectory into the soil medium as shear bulk waves and filtering them within the bandgap frequency range.

5.2 Conclusions of Chapter III

Chapter. 3 is dedicated to the study of the surface waves propagation through partially resonant waveguides constituted of a resonant layer over an elastic half-space. The resonant layer is realized by resonant metamaterials with dimensions much smaller than the wavelength of incident surface waves. In brief, the findings of the chapter are listed as follows:

1. The dynamics of the resonant metamaterial have been described via a mixed static-dynamic homogenization. The mass density of the locally resonant metamaterials is derived by the dynamic homogenization technique in the long-wavelength regime, followed by a static homogenization used for the derivation of elastic moduli. Consequently, effective bulk waves speed of the homogenized medium were explicitly obtained. The out-of-phase motion of the resonators with respect to the host material yields a low-frequency bandgap in the dispersion of bulk waves.
2. The dispersion of Rayleigh waves propagating in a homogenized thick resonant layer attached to the surface of an elastic semi-infinite medium is studied analytically.
3. The existence of a bandgap in the frequency spectrum of the Rayleigh waves and the relation between its frequency width and the thickness of the resonant metamaterial layer were discussed analytically. Indeed, increasing the thickness of the resonant layers extends the bandgap frequencies range. Numerical Finite Element models were developed to confirm the analytical predictions made by analytical dispersion laws.
4. The layered resonant half-space system supports the propagation of multiple surface modes, which are hybridized around the low-frequency bandgap. In addition, the generation of leaky surface waves was observed which contribute to the extension of the bandgap width.
5. The developed analytical framework successfully captured the fundamental dynamic properties of an ultra-thin resonant layer analogous to the locally resonant metasurface. Besides, a limit scenario of the full resonant half-space has been also investigated, where the surface BG is confluent to that of the bulk waves.
6. A seismic wave barrier of deep resonators buried in the soil layer was selected as a case study. Numerical simulations confirmed the surface waves attenuation of a deep finite-length seismic barrier. The proposed resonant wave barrier can be installed as subsurface resonant structures around the infrastructure we aim to shield.

5.3 Conclusions of Chapter IV

Chapter. 4 presented the numerical strategy to design a medium-size scale resonant wave barrier for the control of seismic surface waves. The prototype barrier was constructed with commonly used construction materials including steel, rubber,

and sand to simplify the cost of realization. In what follows, the main outcomes of the chapter are highlighted.

1. A simple and cost-effective medium-scale resonant wave barrier with the operating frequency ranging from 50 to 100 Hz was numerically designed via the Wave Finite Element approach considering the real soil properties. In more detail, numerical dispersion curves were obtained using Comsol Multiphysics [161] to design a barrier with optimal geometry to operate at the target frequency range. The resonant barrier consists of mechanical mass-spring oscillators, e.g., a base plate anchored to the soil, four to eight steel springs suspended between the base and overhead plate, and a plastic barrel filled with sand placed over the steel plate.
2. The proposed passive seismic isolation system was tailored to interact with the vertical motion of the Rayleigh waves at specific frequencies. Once activated, the coupling between the resonant barrier and propagating incident waves remarkably influences the frequency spectra and amplitude decay of the seismic surface waves. This observation was confirmed via time history FE analysis.
3. Graded resonant barriers with increasing and decreasing resonant frequencies were designed to extend the attenuation frequency bandwidth. To account for the frequency variation of the resonators along the array of the metasurface in the real scenario, the seismic isolation performance of a barrier with random resonant frequencies was also studied.
4. A preliminary experimental campaign was conducted to investigate the soil bulk waves speeds, and to characterize the source and measuring equipment. In this set of tests, two scenarios were investigated and compared; (i) the soil in pristine condition and (ii) an array of dead masses (plastic barrels filled with sand) directly placed over the soil surface. The test result confirmed the amplitude reduction of the soil response in the presence of the dead masses. The outcomes of the experiments will serve as a benchmark for the experimental investigation of the designed resonant wave barrier planned to be run in the Euroseistest site.

5.4 Ongoing research

This section provides a brief description of two ongoing experimental research projects, which had been delayed due to the spread of the COVID-19 pandemic. One project addresses the experimental testing of a resonant metamaterial plate

fabricated according to the design principles discussed in Sec.3.6 of Chapter. 3. The other project is dedicated to the final experimental phase of the medium-scale seismic barrier testing. The preliminary experimental test results of the project were reported in Sec. 4.5 of Chapter. 4.

5.4.1 Experimental investigation of surface waves in a resonant metamaterial plate

As discussed in Chapter.3, a metamaterial plate (designed according to the schematic in Fig.3.21) is fabricated to unveil the dispersive nature of surface waves in bulk resonant metamaterials. To confirm the previously discussed analytical and numerical findings, a set of experiments is designed on the metamaterial plate and a reference pristine plate. Both plates are made of PVC material, whereas their mechanical properties are reported in Table.3.1. The metamaterial plate is perforated in accordance with the repetition pattern of the designed phononic cell using a CNC machine, as shown in Fig. 5.1a. In total, 250 basic cells (see Fig. 5.1c) are designed to realize two different wave barrier configurations with different thicknesses along the sides of the plate. Three steel bars with the dimension of $10 \times 10 \times 1000 \text{ mm}$ are cut into 300 steel cubes with dimensions of $10 \times 10 \times 10 \text{ mm}$. Next, steel cubes are press-fitted inside the holes of each unit cell (see Fig. 5.1b) to form the metamaterial plate, as shown in Fig. 5.1d.

Before starting with the perforated plate, a pristine PVC plate was tested. The plate was placed horizontally over an anti-vibration table as shown in Fig.5.2a. A piezoelectric disk was glued at the edge of the plate (see 5.2b) to generate surface waves at the frequency range of interest (e.g., 5000 Hz), where we expect to observe the surface bandgap for the case of resonant metamaterial plate. The Optomet Scanning Laser Doppler Vibrometer (SLVD) was exploited to generate a wave signal and measure the response over the edge of the plate in terms of displacement. An emitter was connected to an amplifier, and the SLVD was connected to a computer, monitor, and amplifier. Fig. 5.2d depicts the dispersion of the surface waves propagation within the pristine plate obtained by performing the Fast Fourier Transform (FFT) of the measured displacement amplitudes in time and space. Analytical dispersion of longitudinal, shear, and Rayleigh waves are over-imposed to the figure in blue, red, and green lines, respectively. In addition, a FE model was developed similar to the one used in Chapter.3 to extract eigenfrequencies of the PVC plate. Fig. 5.2c shows the fundamental surface mode. The analytical, numerical, and experimental results are in good agreement. These experimental findings can be used as a base for the experimental dispersion analysis of the surface waves of the perforated metamaterial plate.

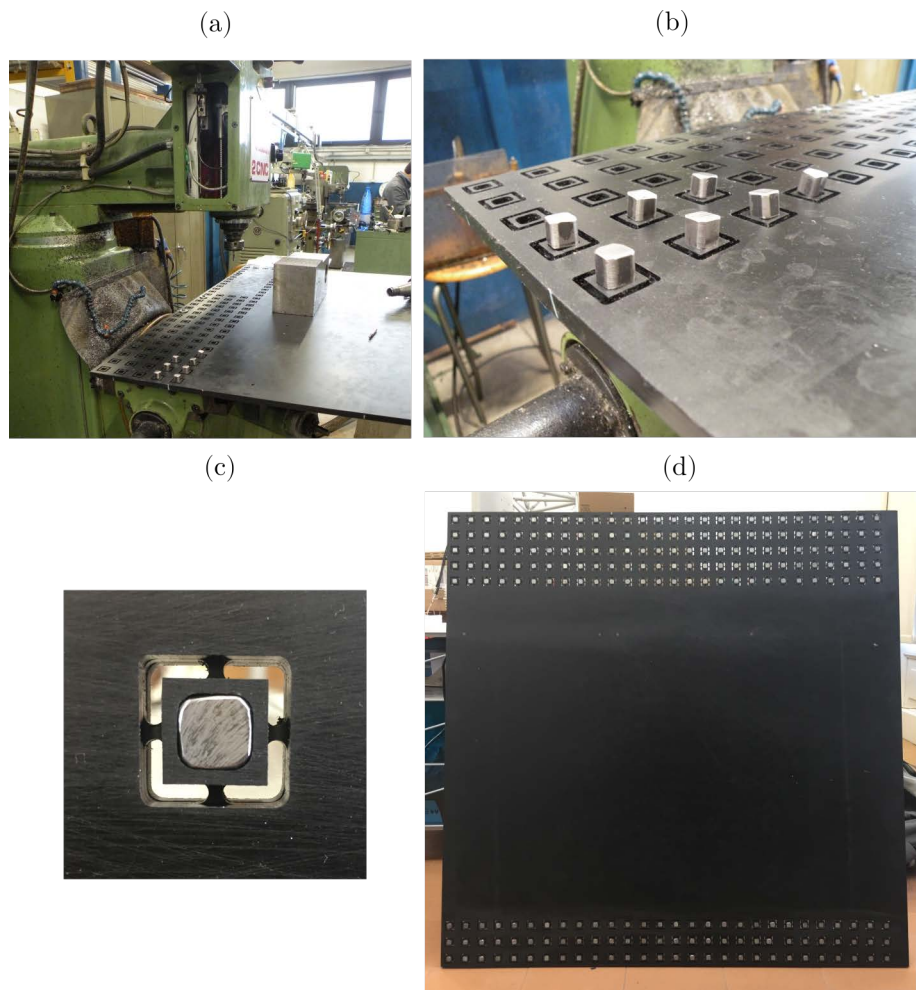


Figure 5.1: (a) A CNC machine is used to perforate the PVC plate. (b) Steel masses are press-fitted inside each basic cells of the plate. (c) The phononic unit cell is realized with four elastic connectors holding a resonating rigid mass. (d) Resonant metamaterial plate made by the regular repetition of the phononic cell. Metamaterial plate includes two barriers with different thicknesses (three and five rows of the resonant cells on the top and bottom edges of the plate, respectively).

5.4.2 Experimental assessment of an innovative proof-of-concept medium-size scale resonant wave barrier

As stated in Chapter.4, the proposed preliminary design of the resonant wave barrier is planned to be experimentally assessed on the field. Considering the results obtained from the first set of experiments (see Sec.4.5 of Chapter.4), several factors can be identified as a possible source of discrepancies between numerical

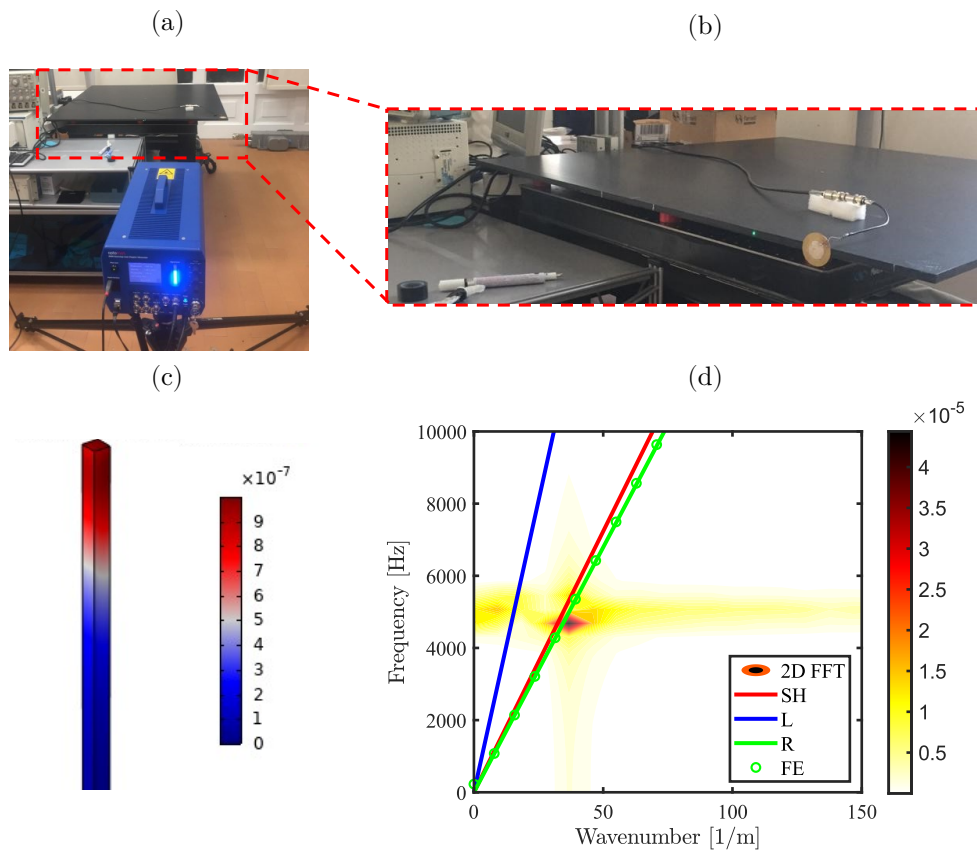


Figure 5.2: (a) Experimental test setup. (b) Pristine PVC plate excited with a piezoelectric buzzer to generate surface waves. (c) The fundamental surface mode of the plate (e.g., $f=5\text{ kHz}$ and $k=56\text{ rad/m}$) is obtained from FE analysis. (d) Surface wave dispersion obtained from FFT response in time and space for excitation at 5 kHz .

and experimental outcomes. Among those factors that can remarkably impact the accuracy of the tests, we can refer to the complex dynamic nature of the soil, instrument errors, excitation source variability, etc. Putting these variables into consideration, it is highly important to first test the dynamic response of a single resonator (see Fig. 5.2b) to achieve full control over the functionality of the barrier during experiments. To do so, the dynamic response of a single resonator, which is purposely designed to operate at 50 Hz , was investigated under vertical loading in a collaboration with the laboratory of Soil Mechanics, Foundation, and Geotechnical Earthquake Engineering of the Aristotle University of Thessaloniki.

The prototype resonator comprised of two steel plates and eight steel springs were placed on the surface of the floor. Two uniaxial accelerometers were installed to measure the vertical response of the resonator; one was placed at the center

of the top plate and the second at one corner of the top plate, as shown in Fig. 5.2a. Additionally, a triaxial accelerometer was installed at the same corner with the uniaxial accelerometer to validate the vertical measurement and to record the possible translational motion of the resonator. Next, a static mass of 100 kg was placed over the plates, as shown in Fig. 5.2b. An elastic hammer was then used as the input source.

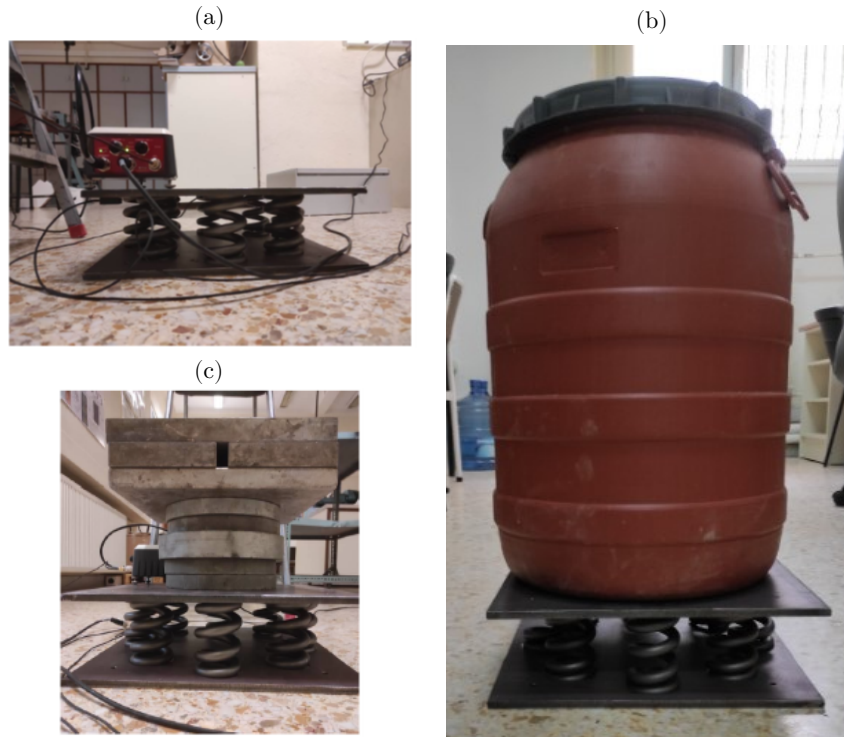


Figure 5.3: (a) Instrumented resonators without the presence of the static mass. (b) The realization of the prototype resonator as the building block of the medium-scale resonant wave barrier. (c) Instrumented resonators with 100 kg of the mass.

The dynamic testing of the resonator has resulted in a nominal resonant frequency of 25 Hz for the resonators, approximately one-half of the designed value. In-depth investigations proved that this discrepancy is due to the imperfect connection between springs and plates. In more detail, only 3 out of 8 springs were in full contact with two plates. This happens due to the fact that some of the steel springs have small discrepancies of 0.5 mm to 1 mm in their lengths. Should all the springs are manufactured with very small variations, the vertical resonant frequency of the resonator will match with the analytical and numerical results. The outcomes of the free vibration testing of a single resonator proved to be decisive to predict the dynamic behavior of the resonant seismic waves barrier on the field.

The minimization of spring defects to achieve the desired frequency response for each resonator.

5.5 Future outlook

The analytical frameworks of this dissertation are developed under simplified assumptions. One of those assumptions is to neglect the damping effect of the locally resonant metasurfaces. Previous studies showed that energy dissipation does not have a significant impact on the fundamental dynamic behavior of resonant metamaterials [9, 94, 178]. One of the possible future research directions is to include the damping effect in the physical models of the locally resonant devices (e.g., IAR metasurface or the concept of the resonant layer), however, it is not going to substantially modify the overall dynamic response of the elastic metasurface.

The preliminary design of the medium-scale resonant wave barrier exploits common construction materials like steel, concrete, sand, and elastomer bearings. The availability, durability, carbon emission, and more importantly the cost of the materials should also be considered in the design procedure. A systematic cost–benefit analysis is necessary to design economically viable locally resonant devices.

Complimentary to the vertically polarized surface waves (Rayleigh waves), future research could aim at the designing of the resonant wave barriers able to filter the propagation of horizontally polarized surface waves, namely Love waves. Since Love waves contribute to the wavefield of earthquakes propagating in the complex stratified soil, special attention should be devoted to the control of this type of mechanical surface wave. While the locally resonant metasurfaces were not able to open bandgaps in the frequency spectrum of horizontally polarized waves [104, 105], the presented analytical approach of the resonant layers comprised of bulk resonant metamaterials can tackle this problem.

More sophisticated analytical models of the resonant metamaterials for seismic surface waves manipulation purposes can be developed to include seismic site effect, wave focusing, the nonlinear behavior of soil, complex soil topography effect, and basin effect. It would be interesting to investigate soil models considering a representative elementary volume consist of air-water-soil composition. Additionally, the effects of nonlinearity should be foreseen also in the design of the resonant metamaterials components.

Complementary to the passive locally resonant devices, active resonant metamaterials can be designed for the filtering, guiding, sensing, and actuation of elastic surface waves across different frequency ranges.

Bibliography

- [1] P. A. Deymier *et al.*, *Acoustic metamaterials and phononic crystals*. Springer, 2013, vol. 173.
- [2] V. G. Veselago, “The electrodynamics of substances with simultaneously negative values of ϵ and μ ,” *Phys. Usp.*, vol. 10, no. 4, pp. 509–514, 1968.
- [3] J. B. Pendry, “Negative refraction makes a perfect lens,” *Phys. Rev. Lett.*, vol. 85, pp. 3966–3969, Oct 2000.
- [4] E. Yablonovitch, “Inhibited spontaneous emission in solid-state physics and electronics,” *Phys. Rev. Lett.*, vol. 58, pp. 2059–2062, May 1987.
- [5] S. John, “Strong localization of photons in certain disordered dielectric superlattices,” *Phys. Rev. Lett.*, vol. 58, pp. 2486–2489, Jun 1987.
- [6] P. Gay-Balmaz and O. J. F. Martin, “Electromagnetic resonances in individual and coupled split-ring resonators,” *Journal of Applied Physics*, vol. 92, no. 5, pp. 2929–2936, 2002.
- [7] M. Kadic, T. Bückmann, R. Schittny, and M. Wegener, “Metamaterials beyond electromagnetism,” *Reports on Progress in Physics*, vol. 76, no. 12, p. 126501, 2013.
- [8] A. Colombi, S. Guenneau, P. Roux, and R. V. Craster, “Transformation seismology: composite soil lenses for steering surface elastic rayleigh waves,” *Scientific reports*, vol. 6, p. 25320, 2016.
- [9] D. Mu, H. Shu, L. Zhao, and S. An, “A review of research on seismic metamaterials,” *Advanced Engineering Materials*, vol. 22, no. 4, p. 1901148, 2020.
- [10] S. Brûlé, S. Enoch, and S. Guenneau, “Emergence of seismic metamaterials: Current state and future perspectives,” *Physics Letters A*, vol. 384, no. 1, p. 126034, 2020.

- [11] S. Brûlé, E. H. Javelaud, S. Enoch, and S. Guenneau, “Experiments on seismic metamaterials: Molding surface waves,” *Phys. Rev. Lett.*, vol. 112, p. 133901, 2014.
- [12] C. Bacquet, “Dispersion and dissipation in viscoelastic metamaterials: theory, experiments and applications,” Master’s thesis, University of Colorado, 2018.
- [13] L. Yang, N. Yang, and B. Li, “Reduction of thermal conductivity by nanoscale 3d phononic crystal,” *Scientific reports*, vol. 3, p. 1143, 01 2013.
- [14] R. Lucklum, M. Ke, and M. Zubtsov, “Two-dimensional phononic crystal sensor based on a cavity mode,” *Sensors and Actuators B: Chemical*, vol. 171-172, pp. 271 – 277, 2012.
- [15] M. Badreddine Assouar, M. Senesi, M. Oudich, M. Ruzzene, and Z. Hou, “Broadband plate-type acoustic metamaterial for low-frequency sound attenuation,” *Applied Physics Letters*, vol. 101, no. 17, p. 173505, 2012.
- [16] Z. Liu, X. Zhang, Y. Mao, Y. Y. Zhu, Z. Yang, C. T. Chan, and P. Sheng, “Locally resonant sonic materials,” *Science*, vol. 289, no. 5485, pp. 1734–1736, 2000.
- [17] J. C. Maxwell, *A Treatise on Electricity and Magnetism*. Oxford University Press, 1873.
- [18] L. Brillouin, *Wave propagation in periodic structure*. New York, NY: McGraw-Hill, 1946.
- [19] V. Narayanamurti, H. L. Störmer, M. A. Chin, A. C. Gossard, and W. Wiegmann, “Selective transmission of high-frequency phonons by a superlattice: The ”dielectric” phonon filter,” *Phys. Rev. Lett.*, vol. 43, pp. 2012–2016, Dec 1979.
- [20] M. M. Sigalas and E. N. Economou, “Elastic and acoustic wave band structure,” *Journal of Sound and Vibration*, vol. 158, no. 2, pp. 377 – 382, 1992.
- [21] M. M. Sigalas and E. N. Economou, “Band structure of elastic waves in two dimensional systems,” *Solid State Communications*, vol. 86, no. 3, pp. 141 – 143, 1993.
- [22] M. S. Kushwaha, P. Halevi, L. Dobrzynski, and B. Djafari-Rouhani, “Acoustic band structure of periodic elastic composites,” *Phys. Rev. Lett.*, vol. 71, pp. 2022–2025, Sep 1993.

- [23] F. R. Montero de Espinosa, E. Jiménez, and M. Torres, “Ultrasonic band gap in a periodic two-dimensional composite,” *Phys. Rev. Lett.*, vol. 80, pp. 1208–1211, Feb 1998.
- [24] J. O. Vasseur, P. A. Deymier, B. Chenni, B. Djafari-Rouhani, L. Dobrzynski, and D. Prevost, “Experimental and theoretical evidence for the existence of absolute acoustic band gaps in two-dimensional solid phononic crystals,” *Phys. Rev. Lett.*, vol. 86, pp. 3012–3015, Apr 2001.
- [25] T. Brunet, J. Vasseur, B. Bonello, B. Djafari-Rouhani, and A.-C. Hladky-Hennion, “Lamb waves in phononic crystal slabs with square or rectangular symmetries,” *Journal of Applied Physics*, vol. 104, no. 4, p. 043506, 2008.
- [26] F. Meseguer, M. Holgado, D. Caballero, N. Benaches, J. Sánchez-Dehesa, C. López, and J. Llinares, “Rayleigh-wave attenuation by a semi-infinite two-dimensional elastic-band-gap crystal,” *Phys. Rev. B*, vol. 59, pp. 12 169–12 172, May 1999.
- [27] S. Huber, “Lectures on mechanical metamaterials,” <https://cmt-qo.phys.ethz.ch/education/autumn-semester-2016--mechanical-metamaterials.html>, online; accessed 05-December-2020.
- [28] Z. Liu, C. T. Chan, and P. Sheng, “Analytic model of phononic crystals with local resonances,” *Phys. Rev. B*, vol. 71, p. 014103, Jan 2005.
- [29] Z. Liu, C. T. Chan, and P. Sheng, “Three-component elastic wave band-gap material,” *Phys. Rev. B*, vol. 65, p. 165116, Apr 2002.
- [30] J. Mei, Z. Liu, W. Wen, and P. Sheng, “Effective dynamic mass density of composites,” *Phys. Rev. B*, vol. 76, p. 134205, Oct 2007.
- [31] H. Larabi, Y. Pennec, B. Djafari-Rouhani, and J. O. Vasseur, “Multicoaxial cylindrical inclusions in locally resonant phononic crystals,” *Phys. Rev. E*, vol. 75, p. 066601, Jun 2007.
- [32] S. Guenneau, A. Movchan, G. Pétursson, and S. A. Ramakrishna, “Acoustic metamaterials for sound focusing and confinement,” *New Journal of Physics*, vol. 9, no. 11, pp. 399–399, nov 2007.
- [33] R. Sainidou, B. Djafari-Rouhani, Y. Pennec, and J. O. Vasseur, “Locally resonant phononic crystals made of hollow spheres or cylinders,” *Phys. Rev. B*, vol. 73, p. 024302, Jan 2006.

- [34] M. Nouh, O. Aldraihem, and A. Baz, “Vibration Characteristics of Meta-material Beams With Periodic Local Resonances,” *Journal of Vibration and Acoustics*, vol. 136, no. 6, pp. VIB–13–1435, 10 2014.
- [35] H. B. A. Ba’ba’a and M. Nouh, “Mechanics of longitudinal and flexural locally resonant elastic metamaterials using a structural power flow approach,” *International Journal of Mechanical Sciences*, vol. 122, pp. 341 – 354, 2017.
- [36] Y. Lai, Y. Wu, P. Sheng, and Z.-Q. Zhang, “Hybrid elastic solids,” *Nat Mater*, vol. 10, no. 8, pp. 620–624, aug 2011.
- [37] Z. Li, H. Hu, and X. Wang, “A new two-dimensional elastic metamaterial system with multiple local resonances,” *International Journal of Mechanical Sciences*, vol. 149, pp. 273 – 284, 2018.
- [38] A. Sridhar, L. Liu, V. Kouznetsova, and M. Geers, “Homogenized enriched continuum analysis of acoustic metamaterials with negative stiffness and double negative effects,” *Journal of the Mechanics and Physics of Solids*, vol. 119, pp. 104 – 117, 2018.
- [39] C. Yilmaz, G. M. Hulbert, and N. Kikuchi, “Phononic band gaps induced by inertial amplification in periodic media,” *Physical Review B*, vol. 76, no. 5, p. 054309, 2007.
- [40] C. Yilmaz and G. Hulbert, “Theory of phononic gaps induced by inertial amplification in finite structures,” *Physics Letters A*, vol. 374, no. 34, pp. 3576 – 3584, 2010.
- [41] E. Baravelli and M. Ruzzene, “Internally resonating lattices for bandgap generation and low-frequency vibration control,” *Journal of Sound and Vibration*, vol. 332, no. 25, pp. 6562 – 6579, 2013.
- [42] A. Bacigalupo and L. Gambarotta, “Simplified modelling of chiral lattice materials with local resonators,” *International Journal of Solids and Structures*, vol. 83, pp. 126–141, 2016.
- [43] N. X. Fang, D. Xi, J. Xu, M. S. Ambati, W. Srituravanich, C. Sun, and X. Zhang, “Ultrasonic metamaterials with negative modulus,” *Nature Materials*, vol. 5, pp. 452–456, 2006.
- [44] Z. Yang, J. Mei, M. Yang, N. H. Chan, and P. Sheng, “Membrane-type acoustic metamaterial with negative dynamic mass,” *Phys. Rev. Lett.*, vol. 101, p. 204301, Nov 2008.

- [45] G. W. Milton and J. R. Willis, “On modifications of newton’s second law and linear continuum elastodynamics,” *Proceedings of the Royal Society A: Mathematical, Physical and Engineering Sciences*, vol. 463, no. 2079, pp. 855–880, 2007.
- [46] H. Huang, C. Sun, and G. Huang, “On the negative effective mass density in acoustic metamaterials,” *International Journal of Engineering Science*, vol. 47, no. 4, pp. 610 – 617, 2009.
- [47] K. H. Matlack, A. Bauhofer, S. Krödel, A. Palermo, and C. Daraio, “Composite 3D-printed meta-structures for low frequency and broadband vibration absorption,” *Proceedings of the National Academy of Sciences of the United States of America*, vol. 113, no. 30, 2015.
- [48] W. Jiang, M. Yin, Q. Liao, L. Xie, and G. Yin, “Three-dimensional single-phase elastic metamaterial for low-frequency and broadband vibration mitigation,” *International Journal of Mechanical Sciences*, vol. 190, p. 106023, 2021.
- [49] M. I. Hussein and M. J. Frazier, “Metadamping: An emergent phenomenon in dissipative metamaterials,” *Journal of Sound and Vibration*, vol. 332, no. 20, pp. 4767 – 4774, 2013.
- [50] M. Lewińska, V. Kouznetsova, J. Van Dommelen, A. Krushynska, and M. Geers, “The attenuation performance of locally resonant acoustic metamaterials based on generalised viscoelastic modelling,” *International Journal of Solids and Structures*, vol. 126, pp. 163–174, 2017.
- [51] A. Aladwani and M. Nouh, “Mechanics of metadamping in flexural dissipative metamaterials: Analysis and design in frequency and time domains,” *International Journal of Mechanical Sciences*, vol. 173, p. 105459, 2020.
- [52] F. Vadalá, A. Bacigalupo, M. Lepidi, and L. Gambarotta, “Free and forced wave propagation in beam lattice metamaterials with viscoelastic resonators,” *International Journal of Mechanical Sciences*, p. 106129, 2020.
- [53] L. Bonanomi, G. Theocharis, and C. Daraio, “Wave propagation in granular chains with local resonances,” *Physical Review E*, vol. 91, no. 3, p. 033208, 2015.
- [54] A. Casalotti, S. El-Borgi, and W. Lacarbonara, “Metamaterial beam with embedded nonlinear vibration absorbers,” *International Journal of Non-Linear Mechanics*, vol. 98, pp. 32–42, 2018.

- [55] W. Jiao and S. Gonella, “Intermodal and subwavelength energy trapping in nonlinear metamaterial waveguides,” *Physical Review Applied*, vol. 10, no. 2, p. 024006, 2018.
- [56] M. Miniaci, A. Krushynska, A. S. Gliozzi, N. Kherraz, F. Bosia, and N. M. Pugno, “Design and fabrication of bioinspired hierarchical dissipative elastic metamaterials,” *Phys. Rev. Applied*, vol. 10, p. 024012, Aug 2018.
- [57] X. Xu, M. V. Barnhart, X. Li, Y. Chen, and G. Huang, “Tailoring vibration suppression bands with hierarchical metamaterials containing local resonators,” *Journal of Sound and Vibration*, vol. 442, pp. 237 – 248, 2019.
- [58] Y. Chen, X. Li, H. Nassar, A. N. Norris, C. Daraio, and G. Huang, “Nonreciprocal wave propagation in a continuum-based metamaterial with space-time modulated resonators,” *Physical Review Applied*, vol. 11, no. 6, p. 064052, 2019.
- [59] M. Attarzadeh, J. Callanan, and M. Nouh, “Experimental observation of nonreciprocal waves in a resonant metamaterial beam,” *Physical Review Applied*, vol. 13, no. 2, p. 021001, 2020.
- [60] J. Marconi, E. Riva, M. Di Ronco, G. Cazzulani, F. Braghin, and M. Ruzzene, “Experimental observation of nonreciprocal band gaps in a space-time-modulated beam using a shunted piezoelectric array,” *Physical Review Applied*, vol. 13, no. 3, p. 031001, 2020.
- [61] A. Srivastava, “Elastic metamaterials and dynamic homogenization: a review,” *International Journal of Smart and Nano Materials*, vol. 6, no. 1, pp. 41–60, 2015.
- [62] S. Taniker and C. Yilmaz, “Phononic gaps induced by inertial amplification in BCC and FCC lattices,” *Physics Letters, Section A: General, Atomic and Solid State Physics*, 2013.
- [63] N. M. M. Frandsen, O. R. Bilal, J. S. Jensen, and M. I. Hussein, “Inertial amplification of continuous structures: Large band gaps from small masses,” *Journal of Applied Physics*, vol. 119, no. 12, p. 124902, 2016.
- [64] S. Muhammad, S. Wang, F. Li, and C. Zhang, “Bandgap enhancement of periodic nonuniform metamaterial beams with inertial amplification mechanisms,” *Journal of Vibration and Control*, vol. 26, no. 15-16, pp. 1309–1318, 2020.

- [65] J. Zhou, L. Dou, K. Wang, D. Xu, and H. Ouyang, “A nonlinear resonator with inertial amplification for very low-frequency flexural wave attenuations in beams,” *Nonlinear Dynamics*, vol. 96, 04 2019.
- [66] Y. Shen, L. Chen, X. Yang, D. Shi, and J. Yang, “Improved design of dynamic vibration absorber by using the inerter and its application in vehicle suspension,” *Journal of Sound and Vibration*, 2016.
- [67] P. Brzeski, T. Kapitaniak, and P. Perlikowski, “Novel type of tuned mass damper with inerter which enables changes of inertance,” *Journal of Sound and Vibration*, 2015.
- [68] D. De Domenico, N. Impollonia, and G. Ricciardi, “Soil-dependent optimum design of a new passive vibration control system combining seismic base isolation with tuned inerter damper,” *Soil Dynamics and Earthquake Engineering*, vol. 105, pp. 37 – 53, 2018.
- [69] J. Bao, Z. Shi, and H. Xiang, “Dynamic responses of a structure with periodic foundations,” *Journal of Engineering Mechanics*, vol. 138, no. 7, pp. 761–769, 2012.
- [70] Z. Shi, Z. Cheng, and H. Xiang, “Seismic isolation foundations with effective attenuation zones,” *Soil Dynamics and Earthquake Engineering*, vol. 57, pp. 143–151, 2014.
- [71] S. Krödel, N. Thomé, and C. Daraio, “Wide band-gap seismic metastructures,” *Extreme Mechanics Letters*, vol. 4, pp. 111 – 117, 2015.
- [72] M. Miniaci, A. Krushynska, F. Bosia, and N. M. Pugno, “Large scale mechanical metamaterials as seismic shields,” *New Journal of Physics*, vol. 18, no. 8, p. 083041, 2016.
- [73] N. Kherraz, M. Miniaci, F. Bosia, A. S. Gliozzi, M. Onorato, and N. M. Pugno, “Hierarchical large-scale elastic metamaterials as an innovative passive isolation strategy for seismic wave mitigation,” in *2020 Fourteenth International Congress on Artificial Materials for Novel Wave Phenomena (Metamaterials)*, 2020, pp. 84–86.
- [74] S. Brûlé, E. H. Javelaud, S. Enoch, and S. Guenneau, “Experiments on seismic metamaterials: Molding surface waves,” *Phys. Rev. Lett.*, vol. 112, p. 133901, 2014.
- [75] S.-H. KIM and M. P. DAS, “Artificial seismic shadow zone by acoustic metamaterials,” *Modern Physics Letters B*, vol. 27, no. 20, p. 1350140, 2013.

- [76] Y. Chen, F. Qian, F. Scarpa, L. Zuo, and X. Zhuang, “Harnessing multi-layered soil to design seismic metamaterials with ultralow frequency band gaps,” *Materials and Design*, vol. 175, p. 107813, 2019.
- [77] X. Pu and Z. Shi, “Surface-wave attenuation by periodic pile barriers in layered soils,” *Construction and Building Materials*, vol. 180, pp. 177 – 187, 2018.
- [78] X. Pu and Z. Shi, “Periodic pile barriers for rayleigh wave isolation in a poroelastic half-space,” *Soil Dynamics and Earthquake Engineering*, vol. 121, pp. 75 – 86, 2019.
- [79] H. J. Xiang, Z. F. Shi, S. J. Wang, and Y. L. Mo, “Periodic materials-based vibration attenuation in layered foundations: experimental validation,” *Smart Materials and Structures*, vol. 21, no. 11, p. 112003, sep 2012.
- [80] Z. Cheng and Z. Shi, “Novel composite periodic structures with attenuation zones,” *Engineering Structures*, vol. 56, pp. 1271 – 1282, 2013.
- [81] A. Amendola, C. Smith, R. Goodall, F. Auricchio, L. Feo, G. Benzoni, and F. Fraternali, “Experimental response of additively manufactured metallic pentamode materials confined between stiffening plates,” *Composite Structures*, vol. 142, pp. 254 – 262, 2016.
- [82] M. Wenzel, O. S. Bursi, and I. Antoniadis, “Optimal finite locally resonant metafoundations enhanced with nonlinear negative stiffness elements for seismic protection of large storage tanks,” *Journal of Sound and Vibration*, vol. 483, p. 115488, 2020.
- [83] Z. Cheng, Z. Shi, A. Palermo, H. Xiang, W. Guo, and A. Marzani, “Seismic vibrations attenuation via damped layered periodic foundations,” *Engineering Structures*, vol. 211, p. 110427, 2020.
- [84] Z. Cheng and Z. Shi, “Composite periodic foundation and its application for seismic isolation,” *Earthquake Engineering and Structural Dynamics*, vol. 47, no. 4, pp. 925–944, 2018.
- [85] O. Casablanca, G. Ventura, F. Garescì, B. Azzerboni, B. Chiaia, M. Chiappini, and G. Finocchio, “Seismic isolation of buildings using composite foundations based on metamaterials,” *Journal of Applied Physics*, vol. 123, no. 17, p. 174903, 2018.
- [86] V. La Salandra, M. Wenzel, O. S. Bursi, G. Carta, and A. B. Movchan, “Conception of a 3d metamaterial-based foundation for static and seismic protection of fuel storage tanks,” *Frontiers in Materials*, vol. 4, p. 30, 2017.

- [87] F. Basone, M. Wenzel, O. S. Bursi, and M. Fossetti, “Finite locally resonant metafoundations for the seismic protection of fuel storage tanks,” *Earthquake Engineering and Structural Dynamics*, vol. 48, no. 2, pp. 232–252, 2019.
- [88] A. Palermo, S. Krödel, A. Marzani, and C. Daraio, “Engineered metabarrier as shield from seismic surface waves,” *Scientific Reports*, vol. 6, p. 39356, 2016.
- [89] V. K. Dertimanis, I. A. Antoniadis, and E. N. Chatzi, “Feasibility analysis on the attenuation of strong ground motions using finite periodic lattices of mass-in-mass barriers,” *Journal of Engineering Mechanics*, vol. 142, no. 9, p. 04016060, 2016.
- [90] A. Palermo and A. Marzani, “Control of love waves by resonant metasurfaces,” *Scientific Reports*, vol. 8, no. 1, p. 7234, 2018.
- [91] A. Maurel, J.-J. Marigo, K. Pham, and S. Guenneau, “Conversion of love waves in a forest of trees,” *Phys. Rev. B*, vol. 98, p. 134311, 2018.
- [92] A. Palermo, F. Zeighami, and A. Marzani, “Design principles of seismic metasurfaces to control love waves,” in *16ECEC conference proceedings*, 06 2018, pp. 1–8.
- [93] L. Xiao, F. Sun, and O. S. Bursi, “Vibration attenuation and amplification of one-dimensional uncoupled and coupled systems with optimal metafoundations,” *Journal of Engineering Mechanics*, vol. 146, no. 7, p. 04020058, 2020.
- [94] A. Colombi, R. Zaccherini, G. Aguzzi, A. Palermo, and E. Chatzi, “Mitigation of seismic waves: Metabarriers and metafoundations bench tested,” *Journal of Sound and Vibration*, vol. 485, p. 115537, 2020.
- [95] A. Franchini, O. S. Bursi, F. Basone, and F. Sun, “Finite locally resonant metafoundations for the protection of slender storage tanks against vertical ground accelerations,” *Smart Materials and Structures*, vol. 29, no. 5, p. 055017, mar 2020.
- [96] K. F. Graff, *Wave motion in elastic solids*, ser. Dover books on physics. New York, NY: Dover, 1991.
- [97] D. Colquitt, A. Colombi, R. Craster, P. Roux, and S. Guenneau, “Seismic metasurfaces: Sub-wavelength resonators and rayleigh wave interaction,” *Journal of the Mechanics and Physics of Solids*, vol. 99, pp. 379 – 393, 2017.

- [98] A. Colombi, P. Roux, S. Guenneau, P. Gueguen, and R. V. Craster, “Forests as a natural seismic metamaterial: Rayleigh wave bandgaps induced by local resonances,” *Scientific Reports*, vol. 6, p. 19238, 2016.
- [99] A. A. Maznev and V. E. Gusev, “Waveguiding by a locally resonant metasurface,” *Phys. Rev. B*, vol. 92, p. 115422, Sep 2015.
- [100] A. Colombi, D. J. Colquitt, P. P. Roux, S. Guenneau, and R. V. Craster, “A seismic metamaterial: The resonant metawedge,” *Scientific reports*, vol. 6, 2016.
- [101] A. Palermo, M. Vitali, and A. Marzani, “Metabarriers with multi-mass locally resonating units for broad band rayleigh waves attenuation,” *Soil Dynamics and Earthquake Engineering*, vol. 113, pp. 265 – 277, 2018.
- [102] A. Palermo, S. Krödel, K. H. Matlack, R. Zaccherini, V. K. Dertimanis, E. N. Chatzi, A. Marzani, and C. Daraio, “Hybridization of guided surface acoustic modes in unconsolidated granular media by a resonant metasurface,” *Phys. Rev. Applied*, vol. 9, p. 054026, 2018.
- [103] X. Pu, A. Palermo, Z. Cheng, Z. Shi, and A. Marzani, “Seismic metasurfaces on porous layered media: Surface resonators and fluid-solid interaction effects on the propagation of rayleigh waves,” *International Journal of Engineering Science*, vol. 154, p. 103347, 2020.
- [104] A. Palermo and A. Marzani, “Control of love waves by resonant metasurfaces,” *Scientific Reports*, vol. 8, p. 7234, 2018.
- [105] R. Zaccherini, A. Colombi, A. Palermo, V. K. Dertimanis, A. Marzani, H. R. Thomsen, B. Stojadinovic, and E. N. Chatzi, “Locally resonant metasurfaces for shear waves in granular media,” *Phys. Rev. Applied*, vol. 13, p. 034055, 2020.
- [106] L. Airoldi and M. Ruzzene, “Design of tunable acoustic metamaterials through periodic arrays of resonant shunted piezos,” *New Journal of Physics*, 2011.
- [107] F. Casadei, T. Delpero, A. Bergamini, P. Ermanni, and M. Ruzzene, “Piezo-electric resonator arrays for tunable acoustic waveguides and metamaterials,” *Journal of Applied Physics*, 2012.
- [108] Y. Y. Chen, G. K. Hu, and G. L. Huang, “An adaptive metamaterial beam with hybrid shunting circuits for extremely broadband control of flexural waves,” *Smart Materials and Structures*, 2016.

- [109] D. Cardella, P. Celli, and S. Gonella, “Manipulating waves by distilling frequencies: A tunable shunt-enabled rainbow trap,” *Smart Materials and Structures*, 2016.
- [110] A. Palermo, P. Celli, B. Yousefzadeh, C. Daraio, and A. Marzani, “Surface wave non-reciprocity via time-modulated metamaterials,” *Journal of the Mechanics and Physics of Solids*, p. 104181, 2020.
- [111] Q. Wu, H. Chen, H. Nassar, and G. Huang, “Non-reciprocal rayleigh wave propagation in space–time modulated surface,” *Journal of the Mechanics and Physics of Solids*, vol. 146, p. 104196, 2021.
- [112] G. J. Chaplain, J. M. De Ponti, G. Aguzzi, A. Colombi, and R. V. Craster, “Topological rainbow trapping for elastic energy harvesting in graded schrieffer-heeger systems,” *Phys. Rev. Applied*, vol. 14, p. 054035, Nov 2020.
- [113] J. M. De Ponti, A. Colombi, E. Riva, R. Ardito, F. Braghin, A. Corigliano, and R. V. Craster, “Experimental investigation of amplification, via a mechanical delay-line, in a rainbow-based metamaterial for energy harvesting,” *Applied Physics Letters*, vol. 117, no. 14, p. 143902, 2020.
- [114] G. Chaplain, J. M. De Ponti, A. Colombi, R. Fuentes Dominguez, P. Dryburgh, D. Pieris, R. Smith, A. Clare, M. Clark, and R. Craster, “Tailored elastic surface to body wave umklapp conversion,” *Nature Communications*, vol. 11, 06 2020.
- [115] A. Diatta, Y. Achaoui, S. Brûlé, S. Enoch, and S. Guenneau, “Control of rayleigh-like waves in thick plate willis metamaterials,” *AIP Advances*, vol. 6, no. 12, p. 121707, 2016.
- [116] R. Aznavourian, T. M. Puvirajesinghe, S. Brûlé, S. Enoch, and S. Guenneau, “Spanning the scales of mechanical metamaterials using time domain simulations in transformed crystals, graphene flakes and structured soils,” *Journal of Physics: Condensed Matter*, vol. 29, no. 43, p. 433004, sep 2017.
- [117] A. Khlopotin, P. Olsson, and F. Larsson, “Transformational cloaking from seismic surface waves by micropolar metamaterials with finite couple stiffness,” *Wave Motion*, vol. 58, pp. 53 – 67, 2015.
- [118] A. Colombi, S. Guenneau, P. Roux, and R. V. Craster, “Transformation seismology: composite soil lenses for steering surface elastic rayleigh waves,” *Scientific Reports*, vol. 6, pp. 25 320 EP –, 2016.

- [119] S. Brule, B. Ungureanu, Y. Achaoui, A. Diatta, R. Aznavourian, T. Antonakakis, R. Craster, S. Enoch, and S. Guenneau, “Metamaterial-like transformed urbanism,” *Innovative Infrastructure Solutions*, vol. 2, p. 2:20, 2017.
- [120] Y. Achaoui, T. Antonakakis, S. Brûlé, R. V. Craster, S. Enoch, and S. Guenneau, “Clamped seismic metamaterials: ultra-low frequency stop bands,” *New Journal of Physics*, vol. 19, no. 6, p. 063022, 2017.
- [121] B. Ungureanu, S. Brûlé, Y. Achaoui, S. Enoch, and S. Guenneau, “Mechanical waves deflection/damping with seismic metamaterials,” in *2015 9th International Congress on Advanced Electromagnetic Materials in Microwaves and Optics (METAMATERIALS)*, 2015, pp. 310–312.
- [122] Y. Pennec, J. O. Vasseur, B. Djafari-Rouhani, L. Dobrzyński, and P. A. Deymier, “Two-dimensional phononic crystals: Examples and applications,” *Surface Science Reports*, vol. 65, no. 8, pp. 229 – 291, 2010.
- [123] M. Hussein, M. Leamy, and M. Ruzzene, “Dynamics of phononic materials and structures: Historical origins, recent progress, and future outlook,” *Applied Mechanics Reviews*, vol. 66, p. 040802, 07 2014.
- [124] R. Craster and S. Guenneau, *Acoustic Metamaterials: Negative Refraction, Imaging, Lensing and Cloaking*, ser. Springer Series in Materials Science. Springer Netherlands, 2012.
- [125] G. Ma and P. Sheng, “Acoustic metamaterials: From local resonances to broad horizons,” *Science Advances*, vol. 2, no. 2, 2016.
- [126] S. Cummer, J. Christensen, and A. Alù, “Controlling sound with acoustic metamaterials,” *Nature Reviews Materials*, vol. 1, p. 16001, 02 2016.
- [127] S. Krödel and C. Daraio, “Microlattice metamaterials for tailoring ultrasonic transmission with elastoacoustic hybridization,” *Phys. Rev. Applied*, vol. 6, p. 064005, Dec 2016.
- [128] A. Palermo, “Elastic waves in periodic and locally resonant metamaterials: algorithms for fast dispersion computation and applications for seismic wave isolation,” Ph.D. dissertation, Alma Mater Studiorum – Università di Bologna, May 2017. [Online]. Available: <http://amsdottorato.unibo.it/8055/>
- [129] K. Ravilious, “Movers and shakers,” *New Scientist*, vol. 231, no. 3083, pp. 34 – 37, 2016.

- [130] F. Zeighami, “Sub-wavelength resonators as seismic rayleigh waves shield,” Master’s thesis, Alma Mater Studiorum – Universita’ di Bologna, July 2016. [Online]. Available: <http://amslaurea.unibo.it/11216/>
- [131] R. Zaccherini, A. Palermo, A. Marzani, A. Colombi, V. Dertimanis, and E. Chatzi, “Mitigation of rayleigh-like waves in granular media via multi-layer resonant metabarriers,” *Applied Physics Letters*, vol. 117, no. 25, p. 254103, 2020.
- [132] N. Boechler, J. K. Eliason, A. Kumar, A. A. Maznev, K. A. Nelson, and N. Fang, “Interaction of a contact resonance of microspheres with surface acoustic waves,” *Phys. Rev. Lett.*, vol. 111, p. 036103, 2013.
- [133] N. Yu and F. Capasso, “Flat optics with designer metasurfaces,” *Nature Materials*, 2014.
- [134] H.-T. Chen, A. J. Taylor, and N. Yu, “A review of metasurfaces: physics and applications,” *Reports on Progress in Physics*, vol. 79, no. 7, p. 076401, jun 2016.
- [135] Q. Ma, G. D. Bai, H. Jing, C. Yang, L. Li, and T. Cui, “Smart metasurface with self-adaptively reprogrammable functions,” *Light: Science and Applications*, vol. 8, p. 98, 10 2019.
- [136] M. El Badawe, T. Almonneef, and O. Ramahi, “A true metasurface antenna,” *Scientific Reports*, vol. 6, p. 19268, 01 2016.
- [137] D. R. Smith, O. Yurduseven, L. P. Mancera, P. Bowen, and N. B. Kundtz, “Analysis of a waveguide-fed metasurface antenna,” *Phys. Rev. Applied*, vol. 8, p. 054048, Nov 2017.
- [138] Y. Xie, W. Wang, H. Chen, A. Konneker, B.-I. Popa, and S. Cummer, “Wavefront modulation and subwavelength diffractive acoustics with an acoustic metasurface,” *Nature communications*, vol. 5, p. 5553, 06 2014.
- [139] Y. Li, X. Jiang, B. Liang, J.-c. Cheng, and L. Zhang, “Metascreen-based acoustic passive phased array,” *Phys. Rev. Applied*, vol. 4, p. 024003, Aug 2015.
- [140] Y. Li, X. Jiang, R.-q. Li, B. Liang, X.-y. Zou, L.-l. Yin, and J.-c. Cheng, “Experimental realization of full control of reflected waves with subwavelength acoustic metasurfaces,” *Phys. Rev. Applied*, vol. 2, p. 064002, Dec 2014.
- [141] G. Ma, M. Yang, S. Xiao, Z. Yang, and P. Sheng, “Acoustic metasurface with hybrid resonances,” *Nature materials*, vol. 13, 06 2014.

- [142] Y. Li and B. M. Assouar, “Acoustic metasurface-based perfect absorber with deep subwavelength thickness,” *Applied Physics Letters*, vol. 108, no. 6, p. 063502, 2016.
- [143] Y. Li and B. Assouar, “Three-dimensional collimated self-accelerating beam through acoustic metascreen,” *Scientific Reports*, vol. 5, p. 17612, 12 2015.
- [144] Y. Mi and X. Yu, “Sound transmission of acoustic metamaterial beams with periodic inertial amplification mechanisms,” *Journal of Sound and Vibration*, vol. 499, p. 116009, 2021.
- [145] Y. Li, C. Shen, Y. Xie, J. Li, W. Wang, S. A. Cummer, and Y. Jing, “Tunable asymmetric transmission via lossy acoustic metasurfaces,” *Phys. Rev. Lett.*, vol. 119, p. 035501, Jul 2017.
- [146] B. Assouar, B. Liang, Y. Wu, Y. Li, J.-C. Cheng, and Y. Jing, “Acoustic metasurfaces,” *Nature Reviews Materials*, vol. 3, 10 2018.
- [147] Y. Jin, D. Torrent, Y. Pennec, and B. Djafari-Rouhani, “Gradient index devices for the full control of elastic waves in plates,” *Scientific Reports*, vol. 6, 2016.
- [148] X. Su, Z. Lu, and A. N. Norris, “Elastic metasurfaces for splitting sv- and p-waves in elastic solids,” *Journal of Applied Physics*, vol. 123, no. 9, p. 091701, 2018.
- [149] M. Addouche, M. A. Al-Lethawe, A. Elayouch, and A. Khelif, “Subwavelength waveguiding of surface phonons in pillars-based phononic crystal,” *AIP Advances*, vol. 4, no. 12, p. 124303, 2014.
- [150] A. Palermo, M. Vitali, and A. Marzani, “Metabarriers with multi-mass locally resonating units for broad band rayleigh waves attenuation,” *Soil Dynamics and Earthquake Engineering*, vol. 113, pp. 265 – 277, 2018.
- [151] E. A. Garova, A. A. Maradudin, and A. P. Mayer, “Interaction of rayleigh waves with randomly distributed oscillators on the surface,” *Phys. Rev. B*, vol. 59, pp. 13 291–13 296, May 1999.
- [152] P. H. Otsuka, S. Mezil, O. Matsuda, M. Tomoda, A. A. Maznev, T. Gan, N. Fang, N. Boechler, V. E. Gusev, and O. B. Wright, “Time-domain imaging of gigahertz surface waves on an acoustic metamaterial,” *New Journal of Physics*, vol. 20, no. 1, p. 013026, jan 2018.

- [153] N. Boechler, J. K. Eliason, A. Kumar, A. A. Maznev, K. A. Nelson, and N. Fang, “Interaction of a contact resonance of microspheres with surface acoustic waves,” *Phys. Rev. Lett.*, vol. 111, p. 036103, Jul 2013.
- [154] R. Thiers-Moggia and C. Málaga-Chuquitaype, “Seismic protection of rocking structures with inerters,” *Earthquake Engineering & Structural Dynamics*, vol. 48, no. 5, pp. 528–547, 2019.
- [155] F. Moraes, M. Silveira, and P. Gonçalves, “On the dynamics of a vibration isolator with geometrically nonlinear inerter,” *Nonlinear Dynamics*, vol. 93, 08 2018.
- [156] Z. Cheng, A. Palermo, Z. Shi, and A. Marzani, “Enhanced tuned mass damper using an inertial amplification mechanism,” *Journal of Sound and Vibration*, vol. 475, p. 115267, 2020.
- [157] P. P. Kulkarni and J. M. Manimala, “Longitudinal elastic wave propagation characteristics of inertant acoustic metamaterials,” *Journal of Applied Physics*, vol. 119, no. 24, p. 245101, 2016.
- [158] G. Acar and C. Yilmaz, “Experimental and numerical evidence for the existence of wide and deep phononic gaps induced by inertial amplification in two-dimensional solid structures,” *Journal of Sound and Vibration*, vol. 332, no. 24, pp. 6389 – 6404, 2013.
- [159] S. Taniker and C. Yilmaz, “Design, analysis and experimental investigation of three-dimensional structures with inertial amplification induced vibration stop bands,” *International Journal of Solids and Structures*, vol. 72, pp. 88 – 97, 2015.
- [160] F. Zeighami, A. Palermo, and A. Marzani, “Inertial amplified resonators for tunable metasurfaces,” *Meccanica*, vol. 54, no. 13, pp. 2053–2065, Oct 2019.
- [161] COMSOL Multiphysics®), “Comsol ab, stockholm, sweden.” 2020. [Online]. Available: <https://www.comsol.com>
- [162] F. Zeighami, A. Palermo, A. Vratsikidis, Z. Cheng, D. Pitilakis, and A. Marzani, “Medium-scale resonant wave barrier for seismic surface waves,” *Mechanics Based Design of Structures and Machines*, vol. 0, no. 0, pp. 1–16, 2020.
- [163] M. Kadic, T. Bückmann, R. Schittny, and M. Wegener, “Metamaterials beyond electromagnetism,” *Reports on Progress in Physics*, vol. 76, no. 12, p. 126501, 2013.

- [164] A. Colombi, D. J. Colquitt, P. P. Roux, S. Guenneau, and R. V. Craster, “A seismic metamaterial: The resonant metawedge,” *Scientific reports*, vol. 6, p. 27717, 2016.
- [165] B. R. Mace and E. Manconi, “Modelling wave propagation in two-dimensional structures using finite element analysis,” *Journal of Sound and Vibration*, vol. 318, no. 4, pp. 884–902, 2008.
- [166] A. A. Maznev, “Bifurcation of avoided crossing at an exceptional point in the dispersion of sound and light in locally resonant media,” *Journal of Applied Physics*, vol. 123, no. 9, p. 091715, 2018.
- [167] F. Zeighami, A. Palermo, and A. Marzani, “Rayleigh waves in locally resonant metamaterials,” *International Journal of Mechanical Sciences*, vol. 195, p. 106250, 2021.
- [168] Y. Yan, A. Laskar, Z. Cheng, F. Menq, Y. Tang, Y. L. Mo, and Z. Shi, “Seismic isolation of two dimensional periodic foundations,” *Journal of Applied Physics*, vol. 116, no. 4, p. 044908, 2014.
- [169] A. Colombi, R. V. Craster, D. Colquitt, Y. Achaoui, S. Guenneau, P. Roux, and M. Rupin, “Elastic wave control beyond band-gaps: Shaping the flow of waves in plates and half-spaces with subwavelength resonant rods,” *Frontiers in Mechanical Engineering*, vol. 3, p. 10, 2017.
- [170] P. T. Wootton, J. Kaplunov, and D. J. Colquitt, “An asymptotic hyperbolic–elliptic model for flexural-seismic metasurfaces,” *Proceedings of the Royal Society A: Mathematical, Physical and Engineering Sciences*, vol. 475, no. 2227, p. 20190079, 2019.
- [171] A. Palermo, F. Zeighami, A. Vratsikidis, Z. Cheng, D. Ptilakis, and A. Marzani, “Design of a medium-scale test for the assessment of a resonant seismic barrier within the reward project,” *Proceedings of the 15th International Conference “Dynamical Systems - Theory and Applications”*, 2019.
- [172] A. Palermo, S. Krödel, K. H. Matlack, R. Zaccherini, V. K. Dertimanis, E. N. Chatzi, A. Marzani, and C. Daraio, “Hybridization of guided surface acoustic modes in unconsolidated granular media by a resonant metasurface,” *Phys. Rev. Applied*, vol. 9, p. 054026, May 2018.
- [173] D. Ptilakis, M. Dietz, D. M. Wood, D. Clouteau, and A. Modaressi, “Numerical simulation of dynamic soil–structure interaction in shaking table testing,”

- Soil Dynamics and Earthquake Engineering*, vol. 28, no. 6, pp. 453 – 467, 2008.
- [174] O. Novotny, “Seismic surface waves,” <http://geo.mff.cuni.cz/>, 1999, online; accessed 1-Dec-2020.
- [175] K. Pitilakis, D. Raptakis, K. Lontzetidis, T. Tika-Vassilikou, and D. Jongmans, “Geotechnical and geophysical description of euro-seistest, using field, laboratory tests and moderate strong motion recordings,” *Journal of Earthquake Engineering*, vol. 3, no. 3, pp. 381–409, 1999.
- [176] D. Raptakis, F. Chavez-Gracia, K. Makra, and K. Pitilakis, “Site effects at euroseistest—i. determination of the valley structure and confrontation of observations with 1d analysis,” *Soil Dynamics and Earthquake Engineering*, vol. 19, no. 1, pp. 1 – 22, 2000.
- [177] D. Pitilakis, E. Rovithis, A. Anastasiadis, A. Vratsikidis, and M. Manakou, “Field evidence of ssi from full-scale structure testing,” *Soil Dynamics and Earthquake Engineering*, vol. 112, pp. 89 – 106, 2018.
- [178] Y. Achaoui, B. Ungureanu, S. Enoch, S. Brûlé, and S. Guenneau, “Seismic waves damping with arrays of inertial resonators,” *Extreme Mechanics Letters*, vol. 8, pp. 30–37, 2016, nanomechanics: Bridging Spatial and Temporal Scales.